Washington University in St. Louis
Washington University Open Scholarship

McKelvey School of Engineering Theses & Dissertations | McKelvey School of Engineering

Spring 5-15-2017

Characterizing Structure, Properties, and Deformation in Metallic Glasses and Olivine Using Instrumented Nanoindentation

Kelly Kranjc
Washington University in St. Louis

Follow this and additional works at: https://openscholarship.wustl.edu/eng_etds

 Part of the Materials Science and Engineering Commons, and the Mechanics of Materials Commons

Recommended Citation

Kranjc, Kelly, "Characterizing Structure, Properties, and Deformation in Metallic Glasses and Olivine Using Instrumented Nanoindentation" (2017). *McKelvey School of Engineering Theses & Dissertations*. 241.
https://openscholarship.wustl.edu/eng_etds/241

This Dissertation is brought to you for free and open access by the McKelvey School of Engineering at Washington University Open Scholarship. It has been accepted for inclusion in McKelvey School of Engineering Theses & Dissertations by an authorized administrator of Washington University Open Scholarship. For more information, please contact digital@wumail.wustl.edu.

WASHINGTON UNIVERSITY IN ST. LOUIS

Institute of Materials Science and Engineering

Dissertation Examination Committee:
Katharine M. Flores, Chair
Kenneth Kelton
Shankar Sastry
Philip Skemer
Simon Tang

Characterizing Structure, Properties, and Deformation in Metallic Glasses and Olivine Using Instrumented Nanoindentation

by

Kelly Kranjc

A dissertation presented to
The Graduate School
of Washington University in
partial fulfillment of the
requirements for the degree
of Doctor of Philosophy

May 2017
St. Louis, Missouri

© 2017, Kelly Kranjc

Table of Contents

List of Figures

List of Tables

Acknowledgements

I would first and foremost like to thank my advisor, Dr. Katharine Flores. She has been an example to me of excellence in academia, as both the leader of our research group and the director of the Institute of Materials Science and Engineering, and I am very honored that she chose me to join her group. Her guidance, support, and assistance throughout the duration of my PhD, both at Ohio State University and now at Washington University in St. Louis, has always been much appreciated and will leave a lasting impression on my professional and personal future.

Similarly, I would like to thank Dr. Philip Skemer, who has also taken on the role of advisor for my olivine project. Without this collaboration, my knowledge of geology would probably never have extended past what I learned in third grade.

Of course, I could not have gotten through graduate school without the help and support of my group members: Peter Tsai, Zachary Rouse, Nicholas Hutchinson, David Brooks, Juan Wang, and Mu Li. I am particularly grateful to Peter Tsai, who has been a dedicated friend and helpful labmate since we first met in 2010. Outside of the group, I made so many friends at school, such as Julie Drexler, Erin Gibbemeyer, Charlotte Guertler, Fei Fang, and Minji Kim. They were a constant source of enjoyment throughout the many emotional ups and downs of research.

Finally, I would like to acknowledge my family for their emotional support. My mother, Suzan, taught me the value of hard work and dedication and I appreciate her more every day. I would also like to thank my dad, Thomas, for the weekly and much appreciated calls containing comedic relief. My grandparents, Ga, Pucky, Gramps, and Azam have always believed in me. Finally, I also need to acknowledge the furry feline members of my family: Toofie, Virgil, and

Pippin. They may not know or care what a PhD is, but their presence at the end of each and every day helped me through it.

Kelly Kranjc

Washington University in St. Louis

May 2017

Dedicated to my first best friend, Beanie.

ABSTRACT OF THE DISSERTATION

Characterizing Structure, Properties, and Deformation in Metallic Glasses and Olivine Using Instrumented Nanoindentation

by

Kelly Kranjc

Doctor of Philosophy in Materials Science and Engineering

Washington University in St. Louis, 2017

Professor Katharine Flores, Chair

Micro- and nanomechanical testing can provide significant insight about the structure, properties, and behavior of materials. These techniques are nondestructive, require only limited amounts of material, and have been known to detect a brittle-to-ductile transition in mechanical behavior due to a size effect. This work utilizes this type of testing to explore fundamental questions about the structure, properties, and behavior of two disparate material systems: metallic glasses and olivine.

Metallic glasses are metallic alloys devoid of any long-range order. Their unique atomic structure imbues them with properties such as a high elastic strain limit, near-theoretical strengths, and the ability to be thermoplastically formed. Despite their high strengths, metallic glasses suffer from an intrinsic lack of tensile ductility compared to other high-performance materials. Recent studies have shown that the macroscopic deformation behavior of these materials might be controlled by structural heterogeneities, the exact nature of which remains ill-defined. To further this area of research, the heterogeneous microstructure of a Zr-based monolithic bulk metallic glass as well as the glass phase of a Ti-based bulk metallic glass matrix-crystalline composite was investigated using nanoindentation and dynamic modulus mapping.

Significant spatial variations in the mechanical properties measured by both techniques suggest a hierarchical arrangement of mechanical heterogeneities in bulk metallic glasses and their composites. Moreover, a previously unobserved elastic microstructure, comprising an interconnected network of elastic features, was revealed by dynamic modulus mapping. Parameters such as aspect ratio and orientation of the microstructural features were defined here, which highlighted the presence of microstructural domains or colonies in the elastic microstructure. The effects of heat treatment and deformation on these heterogeneities were also investigated.

The rheology of olivine plays an important role in the dynamics of Earth's upper mantle. At conditions of low temperature and high stress, such as in semi-brittle regions of the lithosphere, the deformation mechanism transitions into low temperature plasticity. Low temperature plasticity is difficult to study in typical laboratory conditions, requiring high confining pressures to suppress cracking in favor of dislocation glide. Low temperature plasticity of olivine was investigated using nanoindentation and micropillar compression. Nanoindentation provided a means of achieving plastic deformation in the absence of cracking, but measurements obtained via this method are notoriously difficult to translate into uniaxial properties. Using available models to obtain these properties, the data were fit to an established low temperature plasticity flow law, which predicted Peierls stresses for the olivine in the range of 5.32 – 6.45 GPa. As a complement to the nanoindentation, room temperature plasticity was also achieved using micropillar compression. While some of the pillars exhibited catastrophic shearing after a dwell time during creep testing, other pillars showed evidence of plastic deformation after creep testing that was confirmed to be dislocation slip. The data obtained from the micropillar compression was in good agreement with the flow law fits from the nanoindentation. These

results provide increased confidence in the extrapolation of high-pressure and high-temperature laboratory experiments to low-temperature conditions and illustrate the applicability of micromechanical testing methods to the study of mineral rheology.

Chapter 1: Introduction

1.1. On the Benefits and Importance of Small Scale Testing

Microscale mechanical testing can provide valuable information about the structure and properties of a material that are difficult or even impossible to measure at the macroscale. This type of technique is ideal for multi-phase or structurally hierarchical materials, where the properties of the individual phases or components can be studied independently. Furthermore, mechanisms of deformation or mechanical properties can change at smaller sizes and microscale testing techniques are necessary to study these effects. This dissertation uses microscale testing to investigate structure and properties in two different material systems: metallic glasses and their composites and the mineral olivine.

1.2. Introduction to Metallic Glasses

Metallic glasses are truly unique materials, possessing attributes typical of both metals and conventional glasses. They are composed primarily of metallic elements, but, instead of the crystalline atomic structure typical of metals, these materials possess a disordered atomic structure absent of any long range order. Similar to crystalline metals, metallic glasses exhibit primarily metallic bonding and are opaque. Conversely, similar to ceramic glasses, metallic glasses exhibit a glass transition and are absent any structural defects, such as dislocations or grain boundaries.

First discovered in a Au-Si system in 1960 [1], the early metallic glasses required very high cooling rates, on the order of ~10^7 K/s, to solidify from the melt while bypassing crystallization. This cooling rate requirement also meant that the thickness of these early metallic glasses was limited to 10s of micrometers. Later, the focus of research in this area turned towards

the creation of bulk metallic glass (BMG), or metallic glass with critical dimensions greater than 1 millimeter. Great strides were made through the identification of multicomponent alloys with deep eutectics and slow crystallization kinetics that required much smaller critical cooling rates. Probably the first bulk metallic glass was made by Chen [2], who used suction-casting at cooling rates of only ~10^3 K/s to produce millimeter-scale rods of Pd-Cu-Si BMG. A decade later, Turnbull's group [3] demonstrated that centimeter-scale ingots of a Pd-Ni-P system could be produced at cooling rates of only ~10 K/s. Building off of this, one of the most well-known BMGs was created at the California Institute of Technology by Peker and Johnson in the early 1990s [4]. This alloy, named Vitreloy 1 with a composition of $Zr_{41.2}Ti_{13.8}Cu_{12.5}Ni_{10.0}Be_{22.5}$, was successfully cast into fully amorphous rods up to 14 mm in diameter using cooling rates of less than 10 K/s.

Bulk metallic glasses have several advantageous properties, such as large elastic strain limits (~2%), high yield strengths (~1-2 GPa), as well as the ability to be thermoplastically formed in the manner of common silicate glasses [5–7]. The primary disadvantage of bulk metallic glasses, however, is their characteristic lack of tensile ductility. This is due to the deformation processes inherent in metallic glasses.

1.3. Plastic Deformation in Metallic Glasses

The ability of crystalline materials to plastically deform is primarily dictated by the formation and motion of dislocations in the ordered atomic structure. The amorphous atomic structure of BMGs precludes them from forming dislocations, which in turn causes them to exhibit near-theoretical strengths prior to failure [6–9]. In BMGs, plastic deformation is localized into very narrow shear bands and, when loaded in tension, the material will fail due to the unconstrained propagation of a single shear band. The local plastic strain in these shear bands is

very high, but the deformed volume is very small, and thus the material does not exhibit any macroscopic plastic deformability [7,10,11].

Due to the small sample sizes of the initial metallic glasses, the study of their mechanical behavior did not begin until the 1970s [12]. Spaepen depicted the first deformation mechanism map for metallic glasses based on empirical data on deformation in Pd-based glasses [13]. This map showed two deformation regions: homogeneous deformation, occurring at high temperature and low stress; and inhomogeneous deformation, occurring at low temperature and high stress. While plastic deformation in crystalline alloys primarily occurs via dislocation formation and motion, the atomic structure of metallic glasses precludes them from dislocation activity, which in turn causes them to exhibit near-theoretical strengths prior to failure [6,7,9]. In BMGs, deformation strain is localized into thin shear bands which, when loaded in tension, cause material failure due to the unconstrained propagation of a single shear band. The local plastic strain in a shear band is very high, but the deformed volume is very small, thus there is little to no macroscopic ductility in the material (<0.5%).

From our current understanding, shear bands most often form heterogeneously via shear transformation at a shear transformation zone (STZ) [14]. The STZs, which are small groups of atoms, undergo cooperative rearrangement under an applied external stress [15]. The formation and coalescence of several STZs is what produces the nucleus of a shear band [14]. The exact size of the STZs is still unknown, although it is believed to be on the order of 1 nm and involve anywhere from tens to hundreds of atoms [14].

While the nature of shear bands remains an active area of research within the metallic glass community, certain aspects have been established. The thickness of a shear band is typically reported to be 10 – 20 nm [12,14,16]. The vein patterns observed on metallic glass fracture

surfaces is consistent with shear softening within the shear bands. This shear softening is likely to be caused by local heating due to the rapid propagation of the shear band. However, reports of the extent of heating within the shear band are widely varied, ranging from 0.1 to thousands of degrees Celsius [11,14]. The difficulty in pinpointing this value lies in the difficulty of directly measuring temperature changes in such a small volume of material (a thickness of only 20 nm) over such a short time (a shear band velocity is 2.8 m/s according to one study [17]). One of the most notable studies addressing this issue was conducted by Lewandowski and Greer [11], in which they coated a Zr-based BMG with tin, which has a low melting point of 232°C. After bending the BMG, they were able to observe local melting of the tin coating across the shear bands. They calculated an upper bound estimate of the temperature rise at the center of the shear band of 3100 – 8300 K, although the exact temperature rise in a shear band remains an issue of much debate. The corresponding thermal diffusion width around a shear band was found to be 100 – 240 nm, several times greater than the reported shear band thickness of 20 nm.

1.4. Heterogeneities in Metallic Glasses

More recently, mechanical testing, such as nanoindentation and atomic force microscopy [18–23], and modeling work [24–27] have been used to further probe heterogeneity in metallic glasses. The modeling experiments have shown heterogeneity at the angstrom level. The experimental work has discovered the existence of mechanical heterogeneity on a scale greater than 5 nm, even up to the millimeter scale, as shown in Figure 1.1. The range of length scales where heterogeneity has been detected suggests a hierarchy of structural complexity. The presence of these heterogeneities has implications for deformation in metallic glasses, as these heterogeneities could well be affecting shear band initiation and propagation pathways. More experimental and simulation research is needed across a wide range of metallic glass alloys in

order to study any correlations between structural heterogeneity and bulk behavior, and to better ascertain the feature size, spatial distribution, and statistical distribution of these heterogeneities.

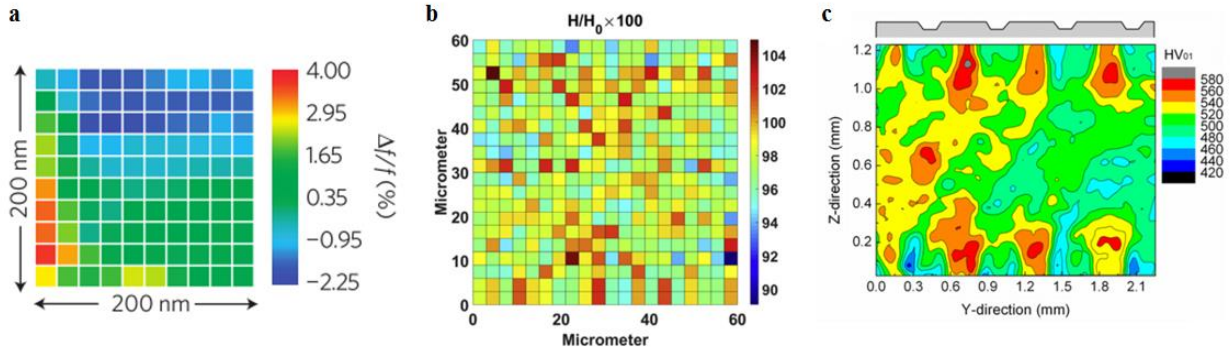

Figure 1.1. Experimental representations of heterogeneity in metallic glasses **(a)** at the nanometer scale via atomic force acoustic microscopy [18], **(b)** at the micrometer scale through nanoindentation [28], and **(c)** at the millimeter scale through microindentation [29].

1.5. Metallic Glass – Crystalline Composites

In order to ameliorate the characteristic lack of tensile ductility in metallic glasses, recent research has focused on integrating a crystalline phase into the metallic glass to create bulk metallic glass composites (BMGCs) [30,31].

BMGCs can be classified based on the way in which they were formed. The first method of creating a BMGC involves combining a distinct crystalline material with a metallic glass into what is termed an ex situ composite. The metallic glass can either be the reinforcement [32] or the matrix [33,34] of the composite. Typically, when trying to improve the ductility of a metallic glass, the glass will be the matrix and a ductile crystalline phase the reinforcement. This is normally achieved by introducing the solid crystalline phase into a metallic glass melt and then cooling the composite, producing a continuous amorphous matrix surrounding the crystalline reinforcement. The crystalline phase can be in the form of wires [34], foams [35], or particles [33]. These composites do increase the compressive strain-to-failure over the monolithic BMG;

however, they are not always able to improve the tensile properties, often due to bonding issues at the interface. The difficulties in this method lie in finding the proper combination of phases and the correct processing method [36]. It is necessary to find a compatible reinforcement/matrix combination that will produce a well-bonded interface and will not react to form undesired secondary phases. Processing is also important to make sure that the reinforcement is fully infiltrated and all surfaces sufficiently wetted to produce a sound interface.

A second type of composite, in situ BMGCs, are formed either when a crystalline structure grows from the melt of a glass-forming alloy or by secondary processing of amorphous material (e.g. partial devitrification) [7]. The first in situ BMGCs were made by melt spinning an aluminum-based alloy at controlled speeds and temperatures to obtain nanocrystals dispersed in an amorphous matrix [37]. These nanocrystalline composites exhibited higher tensile strengths, bending ductility, and hardness compared to a monlithic metallic glass of similar composition.

The nature of the crystalline phase can vary widely between different BMGC systems. For instance, there are alloys with body-centered cubic dendrites [33,38], hexagonal close packed dendrites [39,40] and face-centered cubic dendrites [37,41], alloys with a quasicrystalline phase [7], or alloys where the crystalline phase deforms by a martensitic transformation [42–44]. The dendrite sizes can range from nanometers [45,46] to micrometers [8,47], and can have sharp or rounded features [48]. The crystalline phase morphology (e.g. size, shape, volume fraction) can be altered through compositional changes [39,46,49] or through alloy processing [50,51]. Even slight changes in composition, less than a few atomic percent, can cause large changes in crystalline volume fraction. Generally, however, processing conditions have a more predictable effect on microstructure than composition changes. Suction casting, which results in high cooling rates in the alloy, produces very fine dendrite microstructures [51]. Semi-solid processing, where

the cast alloy is heated and held for a certain amount of time at a temperature above the liquidus of the glass but below the liquidus of the crystalline phase, results in very large dendrites [50,52].

Early composites could only be made in the form of melt spun ribbons, but the development of BMGs also led to the ability to also produce bulk-scale in situ composites. This practice was applied to a Zr-Ti-Nb-Cu-Ni-Be alloy, based on the exceptional glass former Vitreloy 1 [53,54]. Starting with the Zr-Ti-Cu-Ni-Be Vitreloy 1 alloy, it was recognized that Cu, Ni, and Be have little solubility in a Zr-Ti body-centered cubic (BCC) solid solution [53,54]. By adjusting the composition of these elements around the Vitreloy 1 composition, a crystalline dendritic phase was precipitated from the melt. The Nb was added to stabilize and soften the crystalline phase relative to the amorphous matrix, which turned out to be a key factor in giving the composite its ductility. The resulting composite, with a nominal composition of $Zr_{56.2}Ti_{13.8}Nb_{5.0}Cu_{6.9}Ni_{5.6}Be_{12.5}$ and a BCC dendrite structure, was the first to exhibit the high yield strength of a BMG as well as significant necking in tension. The plastic strain in tension for this alloy was measured to be as high as 5% (a significant improvement over the 0% plastic strain in tension for Vitreloy 1). They attributed this improved ductility to the deformation in the crystalline phase (dislocation motion, twinning, and phase transformation) causing load to be transferred to the glass matrix and nucleating shear bands. Further loading would cause propagation of the nucleated shear bands, which would then interact with other shear bands or dendrites.

More recently, the DH-series (Zr-Ti-Nb-Cu-Be) of alloys [38] was developed as an improvement over previous compositions, although it still contains the BCC dendritic crystalline phase. The increased titanium content of these alloys decreased the density, and the absence of nickel increased the fracture toughness and suppressed formation of brittle intermetallics. Figure

1.2 shows the large amount of ductility achieved in the DH-series composites compared to the BMG Vitreloy 1. The alloy DH3 exhibited a yield strength of 1.1 GPa and a total elongation of 13.1%.

Because of the potential for structural applications of BMGCs, recent research has focused on characterizing their deformation behavior and designing new BMGCs with desired properties [5,9,38]. Figure 1.2 shows an example microstructure of the BMGC DH3, accompanied by its stress-strain diagram. From this diagram, the increase in tensile ductility of the BMGC over the monolithic metallic glass is apparent.

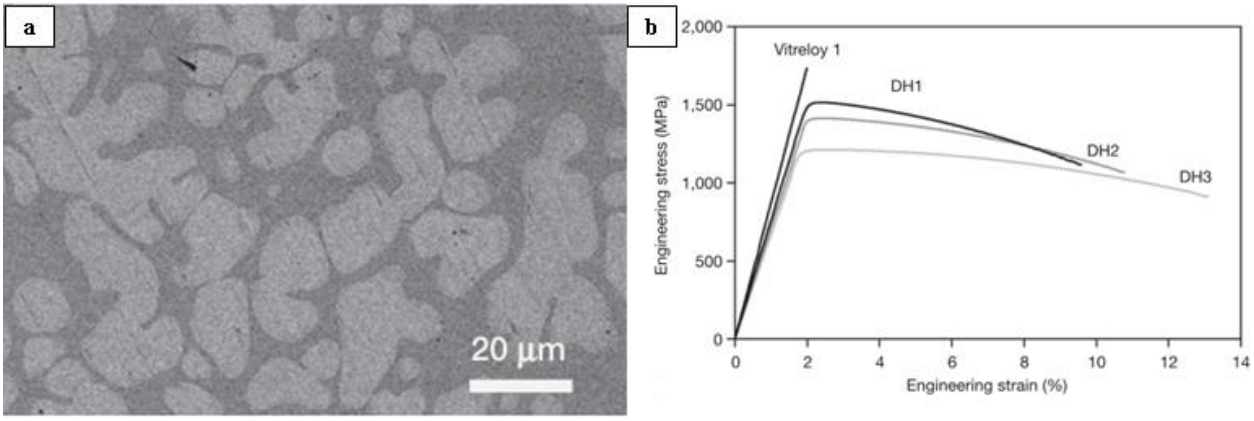

Figure 1.2. (a) Scanning electron micrograph showing the microstructure of the BMGC DH3, where the lighter phase is crystalline and the darker phase is amorphous and (b) the tensile stress-strain diagram of a BMG (Vitreloy 1) and three BMGCs (DH1, DH2, DH3) , showing the increase in ductility in the BMGCs over the BMG [38].

While BMGs fail through the unconstrained propagation of a single shear band, the deformation process for the composites is more complicated. Under an applied stress, deformation in the crystalline phase and subsequent misfit strains between the two phases create stress concentrations at the interface that activate multiple shear bands [53,55,56]. The crystalline phase further acts to arrest those shear bands propagating through the glassy phase [10,38,57]. A larger number of shear bands in the glass phase helps to distribute the plastic strain

so that it is not concentrated into a single shear band, thus leading to the enhanced plasticity of the BMGCs.

A review of the literature shows that the mechanical behavior of BMGCs can be affected by a variety of factors, including composition [38,46,51,58], volume fraction, size, and spacing of the crystalline phase [39,46,50,51], and relative modulus of the two phases [58,59]. While the design of BMGCs remains an open area of research, there are some guidelines for creating tough composites:

1. The glass phase of the composite should have slow kinetics in order to prevent heterogeneous nucleation of unwanted brittle crystals from the dendrites during processing.
2. The microstructure should be spaced to match the critical shear band length in the glass phase.
3. The shear modulus of the crystalline phase should be lower than that of the glass phase. This is so that any cracks that form can be arrested by this softer phase.

The third guideline, which concerns the property mismatch between the two phases, is founded in composite mechanics [60]. However, recent work [44], including our own, has suggested that this is not a necessary condition for obtaining significant ductility. In order to design composites with desired properties (e.g. strength and ductility), it is necessary to determine if and how the relative properties of the two constituent phases affect the overall mechanical behavior of the composite.

The crystalline phase of a BMGC can deform through dislocation motion, twinning, and phase transformation. Currently, it appears that alloys which undergo a phase transformation in

the crystalline phase can achieve the highest recorded ductilities [43]. These alloys also exhibit work-hardening behavior, whereas work-softening is typical in other BMGCs [61]. This type of deformation is thought to produce a complicated stress state in the glass, but it is uncertain how exactly deformation is transferred to the glass phase. Our own research has also indicated that twinning in the crystalline phase leads to higher ductility than when the crystalline phase deforms by dislocation motion. In order to better understand the mechanical reasons as to why different crystalline deformation mechanisms produce different macroscopic stress-strain behavior, it is necessary to study how the crystalline deformation mechanisms affect the resulting deformation mechanisms in the glass phase.

1.6. Introduction to Olivine

Olivine ($(Mg,Fe)_2SiO_4$) is the most abundant mineral in Earth's upper mantle, the region immediately below Earth's crust [62]. The upper mantle is involved in geologic processes such as plate subduction, earthquake generation, and volcanic activity [63]. Thus, the study of olivine deformation is intricately linked with the understanding and prediction of these important geological processes.

The composition of olivine falls between that of pure Forsterite Mg_2SiO_4 and Fayalite Fe_2SiO_4. The crystal structure of olivine is orthorhombic, with lattice constants of the unit cell of a = 4.7560 Å, b = 10.2070 Å, c = 5.9800 [64]. It consists of SiO_4 tetrahedra connected by divalent cations of Mg^{2+} or Fe^{2+}.

Olivine deformation can be accommodated by a variety of mechanisms, including dislocation motion, diffusion, and grain-boundary sliding [65,66]. At high temperatures and low stresses, consistent with conditions deep in the mantle, dislocation creep and grain boundary sliding are expected to be the dominant deformation mechanisms [67,68]. However,

temperatures are lower and stresses are higher in the mantle near the crust [69–71], and experiments show that deformation in this region is controlled by “low temperature” plasticity [72], a mechanism that may reflect a transition to obstacle-limited dislocation glide [73,74]. Rheology in this region can be modeled using a low temperature plasticity flow law, which takes into account material constants such as the flow stress at 0 K [73,74]. However, achieving low temperature plasticity of olivine in a laboratory setting is a very difficult task, which complicates the determination of the constants that define this flow law.

1.7. Dissertation Outline

This chapter covered background information on the two materials of interest in this work: bulk metallic glasses and their composites and the mineral olivine. Chapter 2 will cover the experimental procedures relevant to the micro- and nanoscale characterization performed on each of these materials. Chapters 3 and 4 cover work pertaining to characterization of heterogeneity in metallic glasses and their composites using nanoindentation and dynamic modulus mapping. In Chapter 3, the heterogeneity of a Zr-based monolithic BMG is investigated. The characterization was performed on an as-cast sample, as well as in the vicinity of a shear band. In Chapter 4, a similar investigation into the heterogeneity of an in situ Ti-based bulk metallic glass composite containing crystalline dendrites is presented. The focus of Chapters 5 and 6 switches to the micro- and nanoscale characterization of the mineral olivine. In Chapter 5, a low temperature plasticity flow law describing the strength of the upper mantle is determined through nanoindentation. In Chapter 6, the flow law developed in Chapter 5 is verified though olivine micropillar compression. Chapter 7 concludes this dissertation and provides a summary of the presented work as well as an outlook on future research.

1.8. References

[1] W. Klement, R.H. Willens, P.O.L. Duwez, Non-crystalline Structure in Solidified Gold–Silicon Alloys, Nature. 187 (1960) 869–870. http://www.nature.com/nature/journal/v187/n4740/abs/187869b0.html (accessed September 8, 2014).

[2] H.S. Chen, Thermodynamic Considerations on the Formation and Stability of Metallic Glasses, Acta Metall. 22 (1974) 1505–1511. doi:10.1016/0001-6160(74)90112-6.

[3] H.W. Kui, A.L. Greer, D. Turnbull, Formation of bulk metallic glass by fluxing, Appl. Phys. Lett. 45 (1984) 615–616. doi:10.1063/1.95330.

[4] A. Peker, W.L. Johnson, A Highly Processable Metallic Glass: Zr41.2Ti13.8Cu12.5Ni10.0Be22.5, Appl. Phys. Lett. 63 (1993) 2342–2344. doi:10.1063/1.110520.

[5] D.C. Hofmann, Bulk Metallic Glasses and Their Composites: A Brief History of Diverging Fields, J. Mater. 2013 (2013) 1–8. doi:10.1155/2013/517904.

[6] J. Eckert, J. Das, S. Pauly, C. Duhamel, Processing Routes, Microstructure and Mechanical Properties of Metallic Glasses and their Composites, Adv. Eng. Mater. 9 (2007) 443–453. doi:10.1002/adem.200700043.

[7] J. Eckert, J. Das, S. Pauly, C. Duhamel, Mechanical Properties of Bulk Metallic Glasses and Composites, J. Mater. Res. 22 (2011) 285–301. doi:10.1557/jmr.2007.0050.

[8] G.Y. Sun, G. Chen, G.L. Chen, Design, Synthesis, and Characterization of Bulk Metallic Glass Composite with Enhanced Plasticity, J. Mater. Sci. 46 (2011) 5216–5220. doi:10.1007/s10853-011-5458-z.

[9] M.F. Ashby, A.L. Greer, Metallic Glasses as Structural Materials, Scr. Mater. 54 (2006) 321–326. doi:10.1016/j.scriptamat.2005.09.051.

[10] M.E. Launey, D.C. Hofmann, W.L. Johnson, R.O. Ritchie, Solution to the Problem of the Poor Cyclic Fatigue Resistance of Bulk Metallic Glasses, Proc. Natl. Acad. Sci. U. S. A. 106 (2009) 4986–4991. doi:10.1073/pnas.0900740106.

[11] J.J. Lewandowski, A.L. Greer, Temperature Rise at Shear Bands in Metallic Glasses, Nat. Mater. 5 (2006) 15–18. doi:10.1038/nmat1536.

[12] T. Masumoto, R. Maddin, The mechanical properties of palladium 20 a/o silicon alloy quenched from the liquid state, Acta Metall. 19 (1971) 725–741. doi:10.1016/0001-6160(71)90028-9.

[13] F. Spaepen, A Microscopic Mechanism for Steady State Inhomogeneous Flow in Metallic Glasses, Acta Metall. 25 (1977) 407–415.

[14] A.L. Greer, Y.Q. Cheng, E. Ma, Shear bands in metallic glasses, Mater. Sci. Eng. R Reports. 74 (2013) 71–132. doi:10.1016/j.mser.2013.04.001.

[15] A.S. Argon, Plastic deformation in metallic glasses, Acta Metall. 27 (1979) 47–58. doi:10.1016/0001-6160(79)90055-5.

[16] Y. Zhang, A.L. Greer, Thickness of shear bands in metallic glasses, Appl. Phys. Lett. 89 (2006). doi:10.1063/1.2336598.

[17] W.J. Wright, M.W. Samale, T.C. Hufnagel, M.M. LeBlanc, J.N. Florando, Studies of shear band velocity using spatially and temporally resolved measurements of strain during quasistatic compression of a bulk metallic glass, Acta Mater. 57 (2009) 4639–4648. doi:10.1016/j.actamat.2009.06.013.

[18] H. Wagner, D. Bedorf, S. Küchemann, M. Schwabe, B. Zhang, W. Arnold, K. Samwer, Local Elastic Properties of a Metallic Glass, Nat. Mater. 10 (2011) 439–442. doi:10.1038/nmat3024.

[19] Y.H. Liu, D. Wang, K. Nakajima, W. Zhang, A. Hirata, T. Nishi, A. Inoue, M.W. Chen, Characterization of nanoscale mechanical heterogeneity in a metallic glass by dynamic force microscopy, Phys. Rev. Lett. 106 (2011) 1–4. doi:10.1103/PhysRevLett.106.125504.

[20] Y. Yang, J.F. Zeng, A. Volland, J.J. Blandin, S. Gravier, C.T. Liu, Fractal Growth of the Dense-packing Phase in Annealed Metallic Glass Imaged by High-resolution Atomic Force Microscopy, Acta Mater. 60 (2012) 5260–5272. doi:10.1016/j.actamat.2012.06.025.

[21] H.B. Ke, J.F. Zeng, C.T. Liu, Y. Yang, Structure Heterogeneity in Metallic Glass: Modeling and Experiment, J. Mater. Sci. Technol. 30 (2014) 560–565. doi:10.1016/j.jmst.2013.11.014.

[22] F. Zhu, H.K. Nguyen, S.X. Song, D.P.B. Aji, A. Hirata, H. Wang, K. Nakajima, M.W. Chen, Intrinsic correlation between β-relaxation and spatial heterogeneity in a metallic glass, Nat. Commun. 7 (2016) 11516. doi:10.1038/ncomms11516.

[23] B. Huang, Q.F. He, A.D. Wang, C.L. Zhao, Q. Wang, Y. Yang, C.T. Liu, Tunable elastic heterogeneity caused by deformation-induced magnetization in flexible metallic glass, Scr. Mater. 130 (2017) 7–11. doi:10.1016/j.scriptamat.2016.11.001.

[24] Y. Wang, M. Li, J. Xu, Toughen and harden metallic glass through designing statistical heterogeneity, Scr. Mater. 113 (2016) 10–13. doi:10.1016/j.scriptamat.2015.09.038.

[25] Y. Fan, T. Iwashita, T. Egami, Evolution of elastic heterogeneity during aging in metallic glasses, Phys. Rev. E. 89 (2014) 62313. doi:10.1103/PhysRevE.89.062313.

[26] E. Ma, J. Ding, Tailoring structural inhomogeneities in metallic glasses to enable tensile ductility at room temperature, Mater. Today. (2016). doi:10.1016/j.mattod.2016.04.001.

[27] E. Ma, Tuning order in disorder, Nat. Mater. 14 (2015) 547–552. doi:10.1038/nmat4300.

[28] R. Maass, P. Birckigt, C. Borchers, K. Samwer, C.A. Volkert, Long range stress fields and cavitation along a shear band in a metallic glass: The local origin of fracture, Acta Mater. 98 (2015) 94–102. doi:10.1016/j.actamat.2015.06.062.

[29] S. Scudino, B. Jerliu, S. Pauly, K.B. Surreddi, U. Kühn, J. Eckert, Ductile bulk metallic glasses produced through designed heterogeneities, Scr. Mater. 65 (2011) 815–818. doi:10.1016/j.scriptamat.2011.07.039.

[30] M. Ferry, K.J. Laws, C. White, D.M. Miskovic, K.F. Shamlaye, W. Xu, O. Biletska, Recent developments in ductile bulk metallic glass composites, MRS Commun. 3 (2013) 1–12. doi:10.1557/mrc.2012.32.

[31] Y. Wu, D.Q. Zhou, W.L. Song, H. Wang, Z.Y. Zhang, D. Ma, X.L. Wang, Z.P. Lu, Ductilizing Bulk Metallic Glass Composite by Tailoring Stacking Fault Energy, Phys. Rev. Lett. 109 (2012) 245506. doi:10.1103/PhysRevLett.109.245506.

[32] S.J. Cytron, A metallic glass-metal matrix composite, J. Mater. Sci. Lett. 1 (1982) 211–213. doi:10.1007/BF00724898.

[33] H. Choi-Yim, R.D. Conner, F. Szuecs, W.L. Johnson, Processing, Microstructure and Properties of Ductile Metal Particulate Reinforced Zr57Nb5Al10Cu15.4Ni12.6 Bulk Metallic Glass Composites, Acta Mater. 50 (2002) 2737–2745. http://www.sciencedirect.com/science/article/pii/S0151910702800526 (accessed July 28, 2014).

[34] R.B. Dandliker, R.D. Conner, W.L. Johnson, Melt Infiltration Casting of Bulk Metallic-Glass Matrix Composites, J. Mater. Res. 13 (1998) 2896–2901. doi:10.1557/JMR.1998.0396.

[35] C.Y. Son, G.S. Kim, S.B. Lee, S.K. Lee, H.S. Kim, S. Lee, Dynamic Compressive Properties of Zr-based Amorphous Matrix Composites Reinforced with Tungsten Continuous Fibers or Porous Foams, Metall. Mater. Trans. A. 43 (2012) 1911–1920. doi:10.1007/s11661-011-1066-4.

[36] R.D. Conner, R.B. Dandliker, W.L. Johnson, Mechanical properties of tungsten and steel fiber reinforced Zr41.25Ti13.75Cu12.5Ni10Be22.5 metallic glass matrix composites, Acta Mater. 46 (1998) 6089–6102.

[37] Y.H. Kim, A. Inoue, T. Masumoto, Ultrahigh Tensile Strengths of Al88Y2Ni9M1 (M= Mn or Fe) Amorphous Alloys Containing Finely Dispersed fcc-Al Particles, Mater. Trans. JIM. 31 (1990) 747–749. https://www.jim.or.jp/journal/e/pdf3/31/08/747.pdf (accessed November 11, 2014).

[38] D.C. Hofmann, J.Y. Suh, A. Wiest, G. Duan, M. Lind, M.D. Demetriou, W.L. Johnson, Designing Metallic Glass Matrix Composites with High Toughness and Tensile Ductility, Nature. 451 (2008) 1085–1089. doi:10.1038/nature06598.

[39] M.L. Lee, Y. Li, C.A. Schuh, Effect of a Controlled Volume Fraction of Dendritic Phases on Tensile and Compressive Ductility in La-based Metallic Glass Matrix Composites, Acta Mater. 52 (2004) 4121–4131. doi:10.1016/j.actamat.2004.05.025.

[40] G. He, W. Löser, J. Eckert, L. Schultz, Enhanced Plasticity in a Ti-based Bulk Metallic Glass-forming Alloy by in situ Formation of a Composite Microstructure, J. Mater. Res.

17 (2002) 3015–3018. http://journals.cambridge.org/abstract_S0884291400066917 (accessed November 17, 2014).

[41] M. Calin, J. Eckert, L. Schultz, Improved Mechanical Behavior of Cu–Ti-based Bulk Metallic Glass by in situ Formation of Nanoscale Precipitates, Scr. Mater. 48 (2003) 653–658. http://www.sciencedirect.com/science/article/pii/S1359646202005602 (accessed November 17, 2014).

[42] K.K. Song, D.Y. Wu, S. Pauly, C.X. Peng, L. Wang, J. Eckert, Thermal stability of B2 CuZr phase, microstructural evolution and martensitic transformation in Cu–Zr–Ti alloys, Intermetallics. 67 (2015) 177–184. doi:10.1016/j.intermet.2015.08.015.

[43] F.F. Wu, K.C. Chan, S.S. Jiang, S.H. Chen, G. Wang, Bulk Metallic Glass Composite with Good Tensile Ductility, High Strength and Large Elastic Strain Limit, Sci. Rep. 4 (2014) 5302. doi:10.1038/srep05302.

[44] Y. Wu, Y. Xiao, G. Chen, C.T. Liu, Z. Lu, Bulk Metallic Glass Composites with Transformation-Mediated Work-Hardening and Ductility, Adv. Mater. 22 (2010) 2770–2773. doi:10.1002/adma.201000482.

[45] C. Fan, A. Inoue, Improvement of Mechanical Properties by Precipitation of Nanoscale Compound Particles in Zr-Cu-Pd-Al Amorphous Alloys, Mater. Trans. JIM. 38 (1997) 1040–1046. http://www.jim.or.jp/journal/e/pdf3/38/12/1040.pdf (accessed November 11, 2014).

[46] G. He, W. Löser, J. Eckert, In situ Formed Ti–Cu–Ni–Sn–Ta Nanostructure-dendrite Composite with Large Plasticity, Acta Mater. 51 (2003) 5223–5234. doi:10.1016/S1359-6454(03)00386-0.

[47] C. Fan, R.T. Ott, T.C. Hufnagel, Metallic Glass Matrix Composite with Precipitated Ductile Reinforcement, Appl. Phys. Lett. 81 (2002) 1020. doi:10.1063/1.1498864.

[48] C.N. Kuo, J.C. Huang, X.H. Du, X.J. Liu, T.G. Nieh, Comparison of mechanical response in CuZrAl–V and CuZrAl–Co bulk metallic glass composites, J. Alloys Compd. 586 (2014) S14–S19. doi:10.1016/j.jallcom.2013.01.097.

[49] P. Gargarella, S. Pauly, M. Samadi Khoshkhoo, U. Kühn, J. Eckert, Phase Formation and Mechanical Properties of Ti-Cu-Ni-Zr Bulk Metallic Glass Composites, Acta Mater. 65 (2013) 259–269. doi:10.1016/j.actamat.2013.10.068.

[50] J.L. Cheng, G. Chen, F. Xu, Y.L. Du, Y.S. Li, C.T. Liu, Correlation of the Microstructure and Mechanical Properties of Zr-based in-situ Bulk Metallic Glass Matrix Composites, Intermetallics. 18 (2010) 2425–2430. doi:10.1016/j.intermet.2010.08.040.

[51] R.L. Narayan, P.S. Singh, D.C. Hofmann, N. Hutchinson, K.M. Flores, U. Ramamurty, On the microstructure–tensile property correlations in bulk metallic glass matrix composites with crystalline dendrites, Acta Mater. 60 (2012) 5089–5100. doi:10.1016/j.actamat.2012.06.032.

[52] G.Y. Sun, G. Chen, C.T. Liu, G.L. Chen, Innovative Processing and Property

Improvement of Metallic Glass Based Composites, Scr. Mater. 55 (2006) 375–378. http://www.sciencedirect.com/science/article/pii/S1359646206003228 (accessed November 18, 2014).

[53] C.C. Hays, C.P. Kim, W.L. Johnson, Microstructure Controlled Shear Band Pattern Formation and Enhanced Plasticity of Bulk Metallic Glasses Containing in situ Formed Ductile Phase Dendrite Dispersions, Phys. Rev. Lett. 84 (2000) 2901–2904. http://www.ncbi.nlm.nih.gov/pubmed/11018971.

[54] F. Szuecs, C.P. Kim, W.L. Johnson, Mechanical Properties of Zr56.2Ti13.8Nb5.0Cu6.9Ni5.6Be12.5 Ductile Phase Reinforced Bulk Metallic Glass Composite, Acta Mater. 49 (2001) 1507–1513. http://cat.inist.fr/?aModele=afficheN&cpsidt=976526 (accessed November 14, 2014).

[55] R.T. Ott, F. Sansoz, J.F. Molinari, J. Almer, K.T. Ramesh, T.C. Hufnagel, Micromechanics of Deformation of Metallic-glass–matrix Composites from in situ Synchrotron Strain Measurements and Finite Element Modeling, Acta Mater. 53 (2005) 1883–1893. doi:10.1016/j.actamat.2004.12.037.

[56] G. Chen, J.L. Cheng, C.T. Liu, Large-sized Zr-based Bulk-metallic-glass Composite with Enhanced Tensile Properties, Intermetallics. 28 (2012) 25–33. doi:10.1016/j.intermet.2012.03.054.

[57] E. Pekarskaya, C.P. Kim, W.L. Johnson, In situ Transmission Electron Microscopy Studies of Shear Bands in a Bulk Metallic Glass Based Composite, J. Mater. Res. 16 (2011) 2513–2518. doi:10.1557/JMR.2001.0344.

[58] D.C. Hofmann, J.Y. Suh, A. Wiest, M. Lind, M.D. Demetriou, W.L. Johnson, Development of Tough, Low-density Titanium-based Bulk Metallic Glass Matrix Composites with Tensile Ductility, Proc. Natl. Acad. Sci. U. S. A. 105 (2008) 20136–20140. doi:10.1073/pnas.0809000106.

[59] R.L. Narayan, K. Boopathy, I. Sen, D.C. Hofmann, U. Ramamurty, On the hardness and elastic modulus of bulk metallic glass matrix composites, Scr. Mater. 63 (2010) 768–771. http://www.sciencedirect.com/science/article/pii/S1359646210003957 (accessed July 23, 2013).

[60] M.Y. He, J.W. Hutchinson, Crack Deflection at an Interface between Dissimilar Elastic Materials, Int. J. Solids Struct. 25 (1989) 1053–1067. http://www.sciencedirect.com/science/article/pii/0020768389900218 (accessed December 2, 2014).

[61] D.C. Hofmann, Shape Memory Bulk Metallic Glass Composites, Science (80-.). 329 (2010) 1294–1295.

[62] S.I. Karato, P. Wu, Rheology of the Upper Mantle: A Synthesis, Science (80-.). 260 (1993) 771–778. doi:10.1126/science.260.5109.771.

[63] A.E. Ringwood, Composition and Petrology of the Earth's Mantle, Internatio, McGraw-

Hill, New York, 1975.

[64] J.R. Smyth, R.M. Hazen, The Crystal Structures of Forsterite and Hortonolite at Several Temperatures Up to 900 °C, Am. Mineral. 58 (1973) 588–593.

[65] J.P. Poirier, Creep of Crystals, Cambridge University Press, New York, 1985.

[66] S.I. Karato, Deformation of Earth Materials, Cambridge University Press, New York, 2008.

[67] G. Hirth, D.L. Kohlstedt, Rheology of the Upper Mantle and the Mantle Wedge: A View from the Experimentalists, in: J. Eiler (Ed.), Insid. Subduction Fact., Geophysica, American Geophysical Union, Washington, DC, 2003: pp. 83–105.

[68] L.N. Hansen, M.E. Zimmerman, D.L. Kohlstedt, Grain boundary sliding in San Carlos olivine: Flow law parameters and crystallographic-preferred orientation, J. Geophys. Res. 116 (2011). doi:10.1029/2011JB008220.

[69] D.L. Kohlstedt, B. Evans, S.J. Mackwell, Strength of the Lithosphere: Constraints Imposed by Laboratory Experiments, J. Geophys. Res. 100 (1995) 17587–17602. doi:10.1016/S0016-0032(16)90156-X.

[70] P. Skemer, S.I. Karato, Sheared Lherzolite Xenoliths Revisited, J. Geophys. Res. 113 (2008). doi:10.1029/2007JB005286.

[71] W.M. Behr, G. Hirth, Rheological Properties of the Mantle Lid beneath the Mojave Region in Southern California, Earth Planet. Sci. Lett. 393 (2014) 60–72. doi:10.1016/j.epsl.2014.02.039.

[72] M.C. Tsenn, N.L. Carter, Upper Limits of Power Law Creep of Rocks, Tectonophysics. 136 (1987) 1–26. doi:10.1016/0040-1951(87)90332-5.

[73] U.F.F. Kocks, A.S.S. Argon, M.F.F. Ashby, Thermodynamics and Kinetics of Slip, Pergamon Press, Oxford, 1975. doi:10.1016/0079-6425(75)90005-5.

[74] H.J. Frost, M.F. Ashby, Deformation Mechanism Maps, Pergamon Press, New York, 1982.

Chapter 2: Experimental Procedures

2.1. Introduction

This chapter presents a detailed description of the sample preparation, fabrication, and testing procedures used for both the metallic glass and the olivine studies.

2.2. Sample Preparation

In order to obtain clear images, fabricate specimens, and perform tests, the bulk sample must be sufficiently smooth. Both the metallic glass samples and the olivine samples were cut using a low speed water jet saw and then ground down using a series of SiC papers (400, 600, 800, 1200 grit) wetted with water. The metallic glass samples were ground with the assistance of an Allied MultiPrep™ system for the sake of convenience while the olivine samples were ground by hand to prevent the sample from fracturing. After grinding with the 1200 grit SiC paper, the metallic glass specimens were polished to a mirror finish using an Allied Red Final C polishing cloth wetted with a 0.02 μm colloidal silica suspension. The olivine samples were further polished using Allied Final A polishing clothes and a diminishing series of 3, 1, 0.5, and 0.1 μm diamond pastes.

2.3. Nanoindentation

Nanoindentation is a highly useful tool for ascertaining the mechanical properties of thin films and small volumes of material [1,2]. Similar to microindentation, nanoindentation is performed by pressing an indenter of known geometry into the flat, smooth surface of a material. However, unlike conventional microindentation, the load and displacement of the indenter are continuously measured in order to obtain a load-displacement relationship as shown in Figure 2.1. This feature allows for the measurement of hardness as well as modulus of the sample. The

ability of nanoindentation to obtain mechanical property information consistently and essentially nondestructively with very little material makes it highly suitable for testing a wide range of materials.

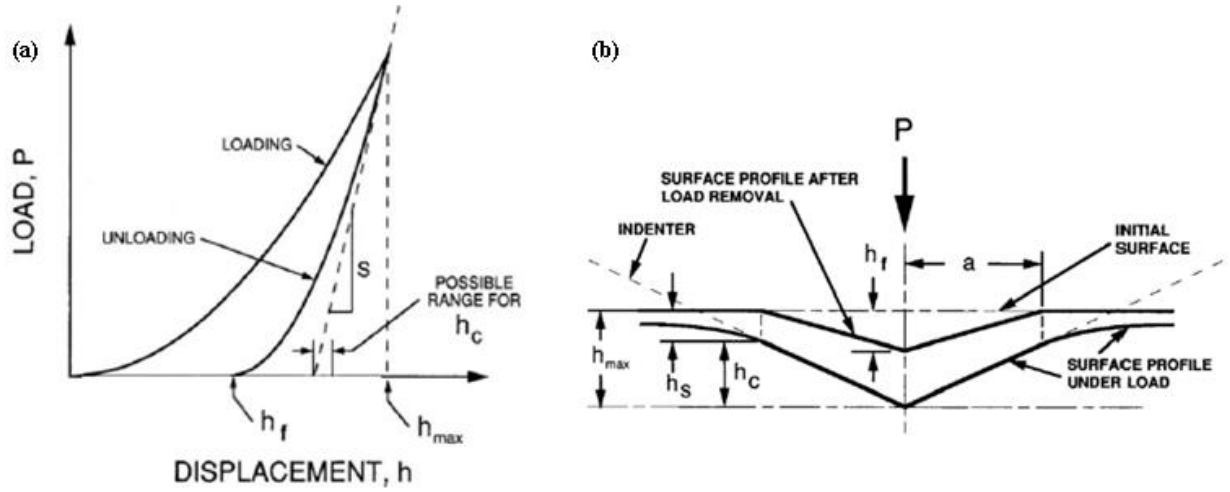

Figure 2.1. (a) Example load-displacement diagram obtained from a nanoindentation test and **(b)** the corresponding cross-section schematic of a sharp indenter penetrating a material [1].

Nanoindentation testing readily measures two material properties: indentation modulus and hardness. The reduced indentation modulus (E_r), given in Equation 2.1, is a function of the contact area of the indent (A) and the slope of the unloading curve near the maximum load (P_{max}). The unloading curve is used in this calculation because it is assumed that there is no reverse plastic deformation during removal of the probe (an assumption which has been shown to be reliable through finite element modeling [3]).

$$E_r = \frac{S\sqrt{\pi}}{2\sqrt{A}} \tag{2.1}$$

The slope of the unloading curve is determined by a method first proposed by Oliver and Pharr [4]. The unloading curve is fitted to a power law function of the form shown in Equation 2.2. The constants α and m are determined by a least squares fitting, and h_f is the indent depth after

unloading (see Figure 2.1). S is solved by analytically differentiating Equation (**2.2)** and evaluating it at peak load ($S = \frac{dP}{dh}\Big|_{P_{max}}$).

$$P = \alpha\left(h - h_f\right)^m \tag{2.2}$$

The hardness, given in Equation 2.3, is a function of only the maximum load and the contact area of the indent.

$$H = \frac{P_{max}}{A} \tag{2.3}$$

The primary difference between nanoindentation and microindentation, apart from the size of the indents, is that the contact area used in nanoindentation is measured indirectly. Specifically, several indents of varying depth are made in a standard sample, which has a known indentation modulus and hardness. Typically the standard is fused quartz, which has an indentation modulus and hardness of 69.6 GPa and 9.25 GPa, respectively. Equation 2.1 can then be rearranged to solve for *A*, and, with multiple indents at varying depths, the coefficient in the polynomial relationship between the contact area and contact depth (h_c) can be determined:

$$A = C_0 h_c^2 + C_1 h_c + C_2 h_c^{\frac{1}{2}} + C_3 h_c^{\frac{1}{4}} + C_4 h_c^{\frac{1}{8}} + C_5 h_c^{\frac{1}{16}} \tag{2.4}$$

The contact depth, as shown in Figure 2.1, is the distance from the tip of the indentation probe to the point at which the probe and sample are no longer in contact when the sample is fully loaded. The contact depth for any indent can be calculated through Equation 2.5, where ε is a geometric factor dependent on the indenter shape (0.75 for Berkovich indenters) and h_{max} is the maximum depth of the indent (see Figure 2.1).

$$h_c = h_{\max} - \varepsilon \frac{P_{\max}}{S} \tag{2.5}$$

In this work, nanoindentation was performed using a Hysitron TI 950 TriboIndenter®. The instrument features very sensitive force and displacement noise floors of less than 30 nN and 0.2 nm, respectively. The probe actuation is controlled through a transducer unit, and either a nanoDMA or 2D transducer was used in all studies presented here. The nanoDMA transducer has a maximum load capability of 12.725 mN and allows for force modulation during testing. The 2D transducer has a maximum load capability of 11.540 mN and is less susceptible to drift issues than the nanoDMA transducer. The system has a magnetic sample stage, so samples are affixed to magnetic stainless steel discs using a cyanoacrylate adhesive.

This system allows for conventional nanoindentation, but can be used to acquire topographical images as well. These topographical images are produced through scanning probe microscopy (SPM), in which the probe is rastered over the sample at a prescribed load, which is chosen to be small enough not to cause wear or permanent deformation to the sample. SPM imaging is highly beneficial in selecting appropriate or desired areas of the sample for further testing, as some features can be detected through SPM imaging which cannot be distinguished through SEM or optical microscopy.

The instrument used in this study was furthermore equipped with a high temperature stage, capable of attaining temperatures ranging from -15 to 200°C. The stage is heated and cooled using either a Peltier device (for cooling or heating below 100°C) or a resistive heater (for heating above 100°C). The high temperature stage is separate from the magnetic stage used for room temperature testing. When using this stage, samples are attached to the stainless steel discs using Epo-Tek H20E epoxy, which is capable of withstanding temperatures of 200°C for 1000 hours without degrading. The discs are held onto this stage through metal clips.

2.4. Dynamic Modulus Mapping

Dynamic modulus mapping was first performed by Asif et al. in 2001 when they coupled nanoindentation with SPM imaging [5]. Similar to SPM imaging, the probe is rastered across the sample surface, however an oscillatory force is simultaneously applied. The resulting displacement amplitude and phase shift are continuously monitored throughout the testing through the use of a lock-in amplifier. A Berkovich probe is used for this application because, at small displacements, the probe is essentially spherical and thus Hertzian contact mechanics can be used in the analysis. The calculations for the storage stiffness, loss stiffness, and complex stiffness are given in Equations 2.6, 2.7, and 2.8, respectively:

$$k_{storage} = \frac{F_D \cos(\varphi)}{d_D} + m_T \times \omega^2 \quad k_T \tag{2.6}$$

$$k_{loss} = \omega \times C_S \tag{2.7}$$

$$k_{complex} = \frac{1}{\frac{1}{\sqrt{k_{storage}^2 \pm k_{loss}^2}} \quad MC} \tag{2.8}$$

where F_D is the dynamic actuation force, φ is the phase shift between the dynamic force and dynamic displacement (d_D), m_T is the transducer mass, k_T is the transducer stiffness, ω is the frequency, C_s is the sample damping, and MC is the machine compliance. These stiffnesses can be converted into moduli using Equation 2.9, where the subscript x refers to either loss, storage, or complex properties and r is the radius of curvature of the probe, assuming spherical contact.

$$E_x = \sqrt{\frac{k_x^3}{6F_D r}} \tag{2.9}$$

The complex modulus for dynamic testing is the same as the reduced modulus for static testing. Equation 2.9 (with complex properties applied) is the dynamic analogue of Equation 2.1. This technique has been used to obtain high resolution (on the order of tens of nanometers) stiffness and modulus maps for a variety of materials, including fiber-epoxy composites [5], a wood-adhesive bond [6], and organic-rich shales [7].

Dynamic modulus mapping was performed using the Hysitron TI 950 TriboIndenter® platform equipped with the nanoDMA® III, allowing for nanoscale dynamic mechanical analysis. The setpoint force and force amplitude are chosen so that the displacement into the sample is around 1 nm, resulting in good plot contrast while only elastically deforming the sample. Each map collected consists of 256x256 pixels, although the area of the map can be specified.

2.5. Micropillar Fabrication

One drawback of nanoindentation is that complex stress and strain fields are created during sample testing, making a comparison or translation to uniaxial properties extremely difficult. Micropillar testing has the advantage that the mechanical response is much easier to quantify due to the specimen geometry creating a more uniform stress distribution. Micropillar fabrication in this work was achieved using focused ion beam (FIB) milling. The FIB instrument is an ideal platform for microspecimen fabrication, because it offers both high resolution imaging and sub-micron precision milling capabilities. In most systems, the beam is produced from a Ga^+ ion source. For imaging, the ion beam is rastered across the sample, producing secondary electrons from the interaction between the ions and the sample. The secondary electrons are then detected and analyzed similar to SEM to produce a high resolution image. For milling, the ion

beam is directed through a prescribed pattern for long enough times to mill away the sample material.

FIB micromachining first started with the fabrication of pillars from single crystals of nickel-based metals [8]. These initial pillars were created through both annular and lathe milling. Annular milling involves machining away material around a feature of interest, leaving the bottom of the pillar connected to the bulk. In the lathe method, an initial pillar is made using one annular milling step. Then, the sample is tilted so that the ion beam is nearly perpendicular to the pillar and the sides are further milled through a series of small cuts and rotations. Lathe-milled pillars generally have less taper and a more defined height than annularly-milled pillars, but often incur more ion damage [9]. The pillars can be compressed using a flat-punch nanoindenter probe and uniaxial stress and strain can be measured. Similarly, other groups used the FIB to make cantilever beams from features of interest [10], which can be loaded to obtain bending or fracture toughness measurements.

While FIB micromachining is very useful for creating micromechanical testing specimens, there are several drawbacks to using this technique. Ion beam damage of the specimen is a concern because it can result in surface amorphization, formation of defects, or phase changes [11]. In order to lessen these effects, the ion beam current is reduced with each milling step so that the surface damage is lessened by each progressive pass. Ion damage is increased when the beam is aimed directly at the sample, meaning that the lathe milling process for pillars creates more surface damage due to the necessity of imaging the sample after each rotation step. This in turn can lead to an altered stress-strain response and deformation morphology in the lathe-milled pillars [9]. The ion beam can also cause sample heating around

the milling site, which is a concern for samples with low thermal conductivity [11] or particularly for polymeric or biological samples [12,13].

In this study, a Zeiss Crossbeam 540 FIB-SEM instrument was used to fabricate all of the olivine pillars. This particular instrument is ideally suited to create micropillars in olivine for a variety of reasons. First, this is a dual beam instrument, which allows for imaging using the electron beam instead of the ion beam, preventing unnecessary ion exposure. Second, this instrument can be programmed to automate the pillar fabrication routine. This allows for the sequential production of a large number of identical pillars with minimal supervision. Although it was not used in this study, this instrument is also capable of simultaneously running both the ion beam and the electron beam, which mitigates charging on the sample surface. This feature could be very useful for micropillar fabrication in similar nonconductive samples.

Because olivine is not conductive, it was necessary to coat the sample with an 8 nm thick layer of iridium to prevent charging. The pillars were then fabricated using the ion beam pattern settings listed in Table 2.1. Each annular pattern was milled starting on the outside edge and moving inwards, with the exception of the final milling step. Setting the milling direction starting from the inside tended to give the pillars a smoother finish.

Table 2.1. Focused ion beam milling parameters. For each step, an annular pattern is milled into the material, centered at the desired pillar location. The inner and outer diameter of the annulus, the beam current, and the ion dose are specified for each step. Steps 1 – 3 are the same no matter the final pillar dimensions. Step 4 is dependent on the desired final pillar dimensions (either 1.25 μm or 350 nm diameter).

Milling Step	Inner Diameter (μm)	Outer Diameter (μm)	Current (nA)	Ion Dose (nC/μm^2)
1	10.70	30.00	15	16
2	4.26	11.06	7	12
3	2.12	4.38	1.5	8
4 (1.25 μm)	1.40	2.16	0.05	5
4 (350 nm)	0.44	2.16	0.05	3.6

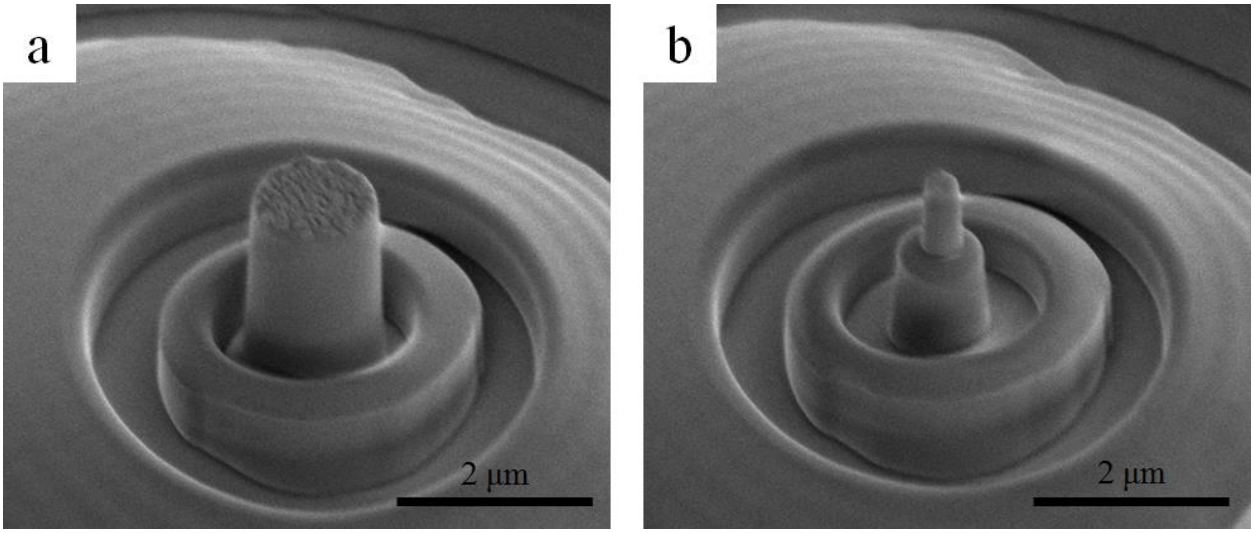

Figure 2.2. SEM images of the (a) 1.25 μm and (b) 350 nm olivine micropillars fabricated using annular FIB milling.

Results from the 350 nm pillars are not presented in this work because the misalignment between the instrument and the smaller pillars was too great, resulting in the pillar shearing off at its base during mechanical testing. However, the milling parameters are still presented here for the benefit of future use of these nanopillars.

2.6. Micropillar Compression Testing

Micropillar compression testing from FIB-milled specimens was first performed in 2004 by Uchic et al. [8]. Since that time, it has become standard practice in the materials science community to study the micro- and nanomechanics of materials. They are often used to study size-scale effects [14–16] and brittle-to-ductile transitions [17,18]. Care must be taken in interpreting the stress-strain relationship, however, because artificially low moduli can be measured due to pillar sink-in and taper [19] while artificially high yield strengths can also be observed [20,21].

For this work, micropillar compression testing was performed using the Hysitron TI 950 TriboIndenter® equipped with a diamond flat punch probe.

2.7. References

[1] A.C. Fischer-Cripps, Nanoindentation, Third Ed, Springer Science+Business Media, LLC, New York, 2011.

[2] W.C. Oliver, G.M. Pharr, Nanoindentation in materials research: Past, present, and future, MRS Bull. 35 (2010) 897–907. doi:10.1557/mrs2010.717.

[3] G.M. Pharr, A. Bolshakov, Understanding Nanoindentation Unloading Curves, J. Mater. Res. 17 (2002) 2660–2671. doi:10.1557/JMR.2002.0386.

[4] W.C. Oliver, G.M. Pharr, An Improved Technique for Determining Hardness and Elastic Modulus Using Load and Displacement Sensing Indentation Experiments, J. Mater. Res. 7 (1992) 1564–1583.

[5] S.A. Syed Asif, K.J. Wahl, R.J. Colton, O.L. Warren, Quantitative Imaging of Nanoscale Mechanical Properties Using Hybrid Nanoindentation and Force Modulation, J. Appl. Phys. 90 (2001) 1192–1200. doi:10.1063/1.1380218.

[6] J. Konnerth, A. Valla, W. Gindl, Nanoindentation Mapping of a Wood-Adhesive Bond, Appl. Phys. A. 88 (2007) 371–375. doi:10.1007/s00339-007-3976-y.

[7] T.M. Wilkinson, S. Zargari, M. Prasad, C.E. Packard, Optimizing Nano-dynamic Mechanical Analysis for High-resolution, Elastic Modulus Mapping in Organic-rich Shales, J. Mater. Sci. (2014). doi:10.1007/s10853-014-8682-5.

[8] M.D. Uchic, D.M. Dimiduk, J.N. Florando, W.D. Nix, Sample Dimensions Influence Strength and Crystal Plasticity, Science (80-.). 305 (2004) 986–989. doi:10.1126/science.1098993.

[9] J. Hütsch, E.T. Lilleodden, The influence of focused-ion beam preparation technique on microcompression investigations: Lathe vs. annular milling, Scr. Mater. 77 (2014) 49–51. doi:10.1016/j.scriptamat.2014.01.016.

[10] D. Di Maio, S.G. Roberts, Measuring Fracture Toughness of Coatings Using Focused-ion-beam-machined Microbeams, J. Mater. Res. 20 (2005) 299–302. doi:10.1557/JMR.2005.0048.

[11] C.A. Volkert, A.M. Minor, Focused Ion Beam Micromachining, MRS Bull. 32 (2007) 389–399.

[12] D. Drobne, M. Milani, V. Leser, F. Tatti, Surface Damage Induced by FIB Milling and Imaging of Biological Samples is Controllable, Microsc. Res. Tech. 70 (2007) 895–903. doi:10.1002/jemt.

[13] R. Schmied, B. Chernev, G. Trimmel, H. Plank, New Possibilities for Soft Matter Applications: Eliminating Technically Induced Thermal Stress during FIB Processing, RSC Adv. 2 (2012) 6932–6938. doi:10.1039/c2ra21025h.

[14] M.D. Uchic, D.M. Dimiduk, A methodology to investigate size scale effects in crystalline

plasticity using uniaxial compression testing, Mater. Sci. Eng. A. 400–401 (2005) 268–278. doi:10.1016/j.msea.2005.03.082.

[15] C.P. Frick, B.G. Clark, S. Orso, A.S. Schneider, E. Arzt, Size Effect on Strength and Strain Hardening of Small-scale [1 1 1] Nickel Compression Pillars, Mater. Sci. Eng. A. 489 (2008) 319–329. doi:10.1016/j.msea.2007.12.038.

[16] J.R. Greer, W.C. Oliver, W.D. Nix, Size dependence of mechanical properties of gold at the micron scale in the absence of strain gradients, Acta Mater. 53 (2005) 1821–1830. doi:10.1016/j.actamat.2004.12.031.

[17] F. Östlund, K. Rzepiejewska-Malyska, K. Leifer, L.M. Hale, Y. Tang, R. Ballarini, W.W. Gerberich, J. Michler, Brittle-to-ductile transition in uniaxial compression of silicon pillars at room temperature, Adv. Funct. Mater. 19 (2009) 2439–2444. doi:10.1002/adfm.200900418.

[18] F. Östlund, P.R. Howie, R. Ghisleni, S. Korte, K. Leifer, W.J. Clegg, J. Michler, Ductile–brittle transition in micropillar compression of GaAs at room temperature, Philos. Mag. 91 (2011) 1190–1199. doi:10.1080/14786435.2010.509286.

[19] A. Bharathula, S.W. Lee, W.J. Wright, K.M. Flores, Compression testing of metallic glass at small length scales: Effects on deformation mode and stability, Acta Mater. 58 (2010) 5789–5796. doi:10.1016/j.actamat.2010.06.054.

[20] A.A. Konstantinidis, K. Michos, E.C. Aifantis, On the correct interpretation of compression experiments of micropillars produced by a focused ion beam, J. Mech. Behav. Mater. 25 (2016) 83–87. doi:10.1515/jmbm-2016-0009.

[21] B.E. Schuster, Q. Wei, T.C. Hufnagel, K.T. Ramesh, Size-independent strength and deformation mode in compression of a Pd-based metallic glass, Acta Mater. 56 (2008) 5091–5100. doi:10.1016/j.actamat.2008.06.028.

Chapter 3: Heterogeneity in As-Cast and Deformed Monolithic Metallic Glass

Portions of this chapter are adapted from the following manuscript, currently in review with Acta Materialia: P. Tsai, K. Kranjc, K.M. Flores, Hierarchical Heterogeneity and an Elastic Microstructure Observed in a Metallic Glass Alloy, Acta Materialia, submitted. All data presented in this chapter was collected by K. Kranjc, with the exception of the silicon modulus map. Data analysis was shared by both K. Kranjc and P. Tsai. Portions of the co-authored manuscript written by P. Tsai are included here for clarity.

3.1. Introduction

Understanding structure-property relationships has long been at the heart of alloy development and design. For crystalline alloys, depending on the complexity of the overall microstructure, variations in structural features could span length scales across many orders of magnitude. The structure of metallic glasses is more difficult to characterize; in contrast to crystalline alloys, metallic glasses are devoid of long range translational atomic symmetry, although short and medium range ordering persists [1]. For this reason, metallic glasses appear deceptively homogeneous and isotropic when investigated with conventional characterization techniques, without the typical microstructural features that account for complexity and uniqueness in crystalline alloys. Despite the apparent microstructural similarity of metallic glasses, however, their deformation behavior can vary drastically with both alloy composition and processing conditions [2], implying the existence of a complex underlying structure that is not yet fully understood.

On the atomic length scale, the structure of an amorphous alloy is by definition heterogeneous, possessing a statistical spread of different atomic cluster configurations, randomly orientated and distributed throughout its volume. Structural heterogeneities extending beyond the size of atomic clusters are less obvious, especially considering the high atomic

packing efficiency of bulk amorphous alloys and their general resemblance to the disordered liquid [3]. Recent experimental and molecular dynamics studies have reported nanoscale heterogeneous structure in metallic glasses [4–8]. The existence of such heterogeneities has profound implications on the macroscopic mechanical behavior [9]. Finite element modeling has shown that increased toughness and ductility can also be achieved through designing nanoscale heterogeneity via free volume dispersion, which promotes more profuse shear banding [10]. Experimentally, atomic force microscopy has been used to show the existence of nanoscale fluctuations in elastic modulus and energy dissipation in several metallic glass alloys [4–7]. However, the characteristic size, spacing, and distribution of these heterogeneities has not been determined, leaving much unknown about their nature and the effect that they might have on the resulting properties of the metallic glass.

3.2. Experimental Procedure

3.2.1. Sample Preparation and Testing

In this study, nanoindentation and dynamic modulus mapping (DMM) were used to characterize changes in spatial fluctuations in mechanical properties of a monolithic metallic from either annealing or shear banding. The BMG $Zr_{58.5}Cu_{15.6}Ni_{12.8}Al_{10.3}Nb_{2.8,}$ commonly referred to as Vitreloy 106a, with centimeter-scale casting thickness was used because of its ease of processing and it has been extensively studied within the BMG community [11]. All of the samples were prepared by arc melting pure elements in an argon environment and casting into a copper mold. The amorphous nature of each sample was verified through transmission electron microscopy analysis.

In the nanoindentation experiments, a 10x10 array of indents spaced 8 μm apart was performed on an as-cast sample. The sample was cut from a 3 mm thick plate and polished to a

mirror finish using colloidal silica. The indents on the as-cast sample were performed to a maximum load of 8 mN at a loading and unloading rate of 1.6 mN/s. The sample was then annealed at 370°C for 1 hour (the glass transition temperature, T_g is 390°C), repolished to remove the oxide layer, and the indentation was repeated. The sample was then annealed 1 hour further (for a total annealing time of 2 hours), repolished, and then indented again. Due to unexpected differences in the data acquired from different specimens, three separate indentation arrays were then performed in order to determine any difference caused by maximum indentation load: one each at maximum loads of 8, 4, and 1.2 mN. The array size (10x10) and spacing (8 μm) remained the same, as well as the loading and unloading rate of 1.6 mN/s.

For the DMM experiments, a rectangular bar specimen cut from a 3 mm thick plate was polished on one side to a mirror finish using colloidal silica. To examine the existence of mechanical heterogeneities at a smaller length scale than the nanoindentation experiments, the DMM was performed over a 5x5 μm square area. Then, in order to induce shear banding the bar was deformed by rolling at room temperature several times until a 5% reduction of thickness was achieved. The total thickness reduction per pass was limited to less than 1%. In order to identify the location of a shear band after polishing, a focused ion beam instrument was used to mill the perimeter of a 100x100 μm square area encompassing two intersecting shear bands. The sample face containing the milled square was then ground and polished to a mirror finish suitable for DMM, removing shear steps and any ion beam damage from the surface while leaving the milled pattern visible. The DMM was then repeated, obtaining a montage of 5x5 μm maps within the milled area. All of the DMM was performed as described in Section 2.4.

3.3. Results

Comparing the as-cast and annealed samples in Figure 3.1, annealing caused an increase in both the average indentation modulus E_r and hardness H. The average indentation modulus increased from 100 to 106 GPa after annealing while the hardness increased from 6.16 to 6.37 GPa. Significant spatial variation was observed in both the indentation modulus and hardness, which can be seen for the as-cast sample in Figure 3.1(a-b). In this representation, both properties are expressed as deviations from their respective average, $100\% \times (X - X_{avg})/X_{avg}$, where X represents either E_r or H. Histograms of the data are well described by Gaussian distributions, as shown in Figure 3.1(c-d). The distributions for both E_r and H broaden slightly as a result of annealing. To verify that the scatter in the measurements was indicative of the material properties and not due to instrumentation limitations, the nanoindentation was performed to a maximum load of 1.5 mN on a single crystal silicon wafer grown in the <100> direction, which can be considered a structurally homogeneous standard. A complimentary nanoindentation array was also performed to the same load on the same monolithic glass alloy cast into a 3 mm rod. The histograms of the silicon and metallic glass nanoindentation data are shown in Figure 3.1(e-f). Compared to the BMG samples, the silicon exhibited a much narrower distribution of E_r and H values.

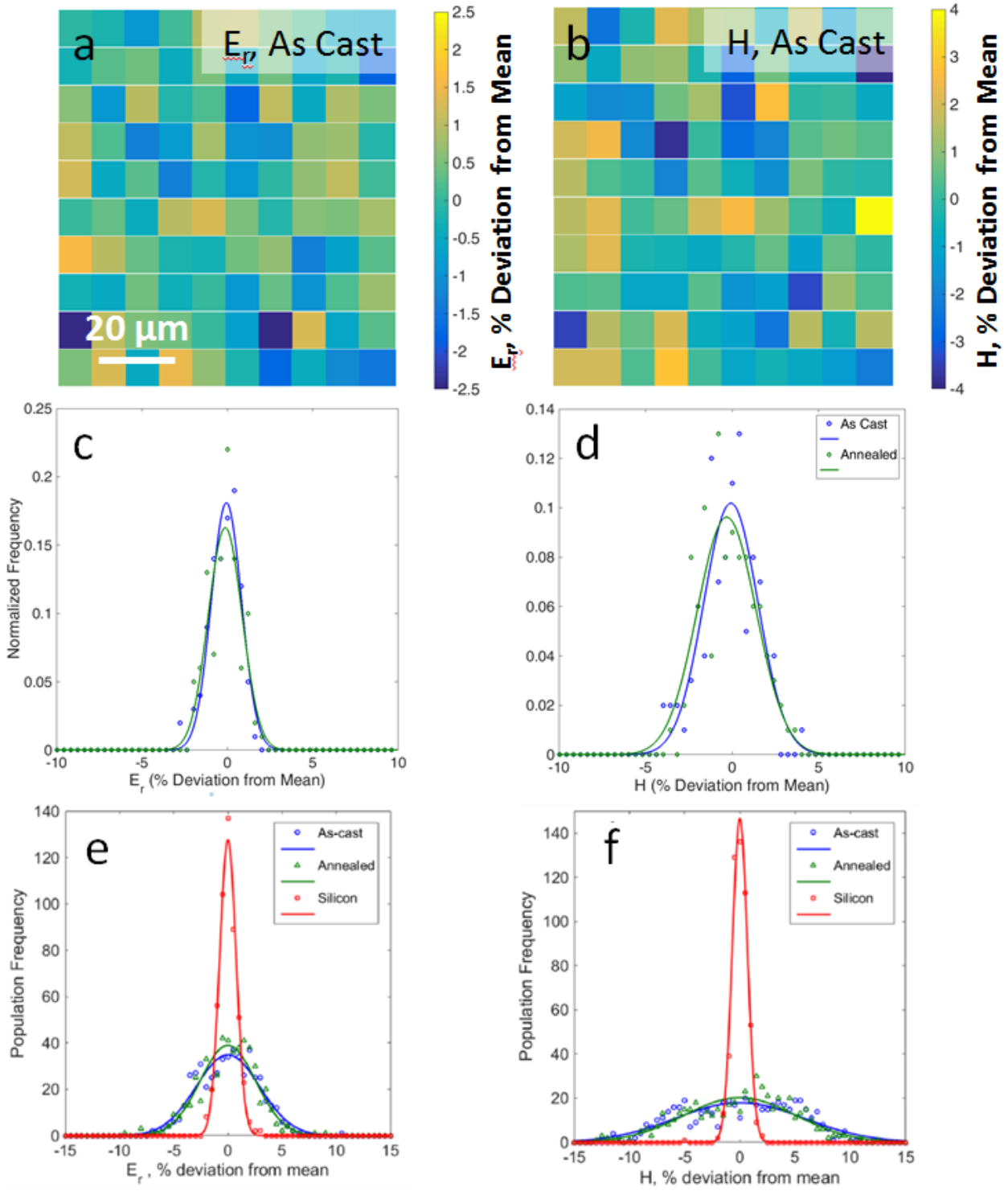

Figure 3.1. (a-b) Color map representations of nanoindentation data showing micrometer scale heterogeneity in an as-cast monolithic bulk metallic glass plate indented at 8 mN. The maps of **(a)** indentation modulus (E_r) and **(b)** hardness (H) each consist of 100 indents collected in a rectangular array measuring 72 x 72 µm. White squares correspond to unsuccessful indents. **(c-d)** The corresponding histograms of **(c)** E_r and **(d)** H compare the as-cast and annealed BMG and

show a slightly narrower distribution for the annealed BMG nanoindentation data. **(e-f)** Histograms of **(e)** E_r and **(f)** H for the same alloy cast into a 3 mm rod and indented at 1.5 mN. For comparison, the histogram for single crystal <100> silicon indented to 1.5 mN is also shown.

Figure 3.2 shows the indentation modulus and hardness relationship for the as-cast and annealed 3 mm plate specimen. The as-cast data, acquired at a load of 8 mN, shows a trend of increasing hardness with increasing modulus that is well described by a linear fit. The average modulus, 100 GPa, and average hardness, 6.16 GPa, were slightly lower than for the 3 mm rod, which could be due to different indent loads and loading rates, different sample geometries causing different cooling histories, or typical inconsistencies between castings. After 1 hour of annealing at $0.95T_g$, the modulus-hardness correlation shifted to higher modulus and hardness values. The average indentation modulus increased to 106 GPa while the average hardness increased to 6.37 GPa. The general trend of increasing hardness with increasing modulus remained consistent and all of the data sets followed the same linear scaling law of $H \approx (0.06 – 0.08)E_r$. After 2 hours of annealing, the indentation modulus and hardness values remained essentially the same, indicating that the sample had fully relaxed at that annealing condition. The standard deviation in the modulus and hardness data remained essentially the same between the as-cast (SD_E = 0.85 GPa, SD_H = 0.10 GPa), 1 hour annealed (SD_E = 0.97 GPa, SD_H = 0.10 GPa), and 2 hour annealed (SD_E = 0.93 GPa, SD_H = 0.10 GPa) tests when the indentation load was kept constant at 8 mN. However, when the indentation load was decreased for the 2 hour annealed sample, the scatter in the data increased correspondingly so that the greatest amount of variation was observed for the 1.2 mN tests (SD_E = 1.95 GPa, SD_H = 0.20 GPa). The standard deviation from the 1.5 mN indents in the annealed 3 mm rod shown in Figure 3.1 (SD_E = 1.23 GPa, SD_H = 0.14 GPa) falls between the 1.2 mN and 8 mN data from the plate.

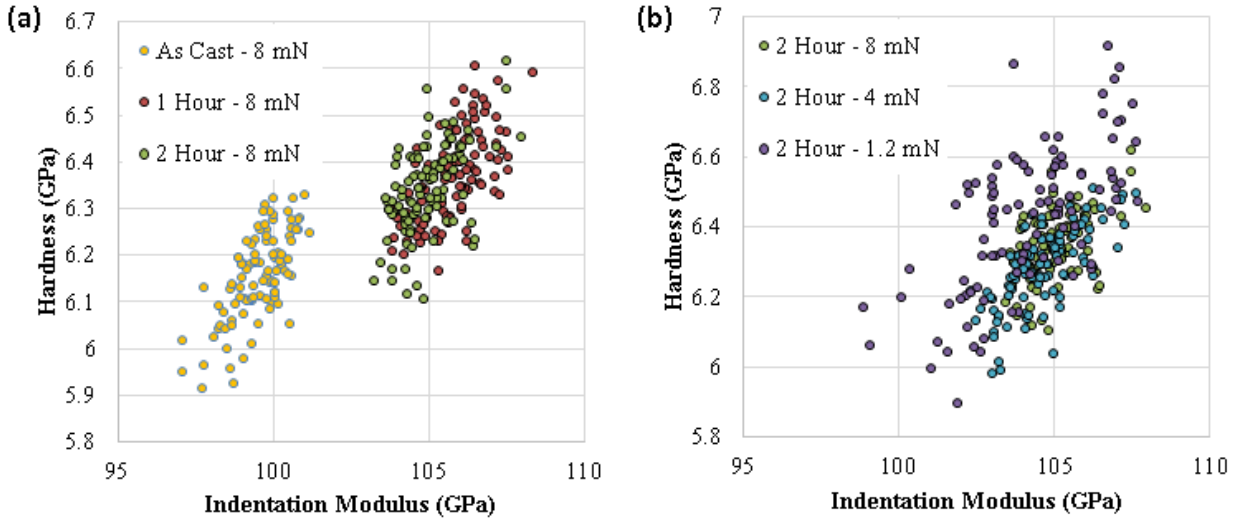

Figure 3.2. (a) Plot of the indentation modulus-hardness relationship for the as-cast and annealed monolithic BMG indented to a load of 8 mN. **(b)** The BMG annealed for 2 hours was indented to three maximum loads: 8, 4, and 1.2 mN. An increase in the scatter of the data is observed as the indentation load decreases. Each data set consists of 100 indents.

To further probe mechanical variations in the BMG, dynamic modulus mapping was also performed. Figure 3.4(a) shows some example 5x5 μm modulus maps obtained from the as-cast, undeformed BMG sample. As with the nanoindentation, for ease of comparing between different maps, the modulus values are again represented as a deviation from the average value of each map as opposed to an absolute value. The distributions in modulus obtained from the mapping procedure shown in Figure 3.4(b) are again well fit by a Gaussian distribution. Spatial fluctuations in the local elastic modulus are clearly evident in each map, forming an "elastic microstructure" with an interconnected stiffer-than-average network encompassing pockets of more compliant material. Maps 1 and 2 were acquired within 100 μm of each other on the LxW side of the LxWxT rectangular sample, as were Maps 3 and 4 on the perpendicular LxT side. However, there are noticeable differences between the four modulus maps, such as how diffuse or distinct the interconnected stiff network is or the general morphology of the stiff network, as

well as variations in their corresponding modulus distributions even when collected less than 100 μm apart.

The dynamic modulus maps were analyzed by determining the distribution in moduli values normalized to the average modulus of the maps. Furthermore, the maps were analyzed using the spatial autocorrelation function $F_{corr}(x,y)$ to determine the characteristic feature aspect ratio and orientation. The autocorrelation function is defined as:

$$F_{corr}(x,y) = \iint F(x',y')F(x'+x,\ y'+y)dx'dy' \tag{3.1}$$

where the spatially varying function $F(x',y')$ represents the modulus map. In practice, this function essentially overlays a modulus map overtop of itself and measures the amount of correlation as one identical map is shifted in the x and y direction. Thus, $F_{corr}(0,0)$ would have the highest correlation as two identical maps that have not been shifted would be perfectly correlated. Because the modulus maps collected here are discretized into 256x256 pixels, the autocorrelation function takes on the form:

$$F_{corr}(x,y) = \sum_{y'}\sum_{x'} F(x',y')F(x'+x,\ y'+y) \tag{3.2}$$

The characteristic feature dimensions can be obtained by measuring the size and orientation of the point defined by $F_{corr}(0,0)$ to the surrounding local minimum. The autocorrelation function can be normalized to $F_{corr}(0,0)$ for better comparison between plots.

The local properties of the modulus map were evaluated by sectioning the original maps into smaller, overlapping maps and performing the analysis on each of the reduced maps. To begin, the original map is tiled into a 3x3 array so that the analysis at the edges of the map is not limited by the map boundary. Then, reduced maps measuring 64x64 pixels and spaced 8 pixels apart are extracted from the central map of the 3x3 array. This results in a 32x32 array of

reduced maps representing the original map. Each reduced map is then analyzed as depicted in Figure 3.3. An autocorrelation function analysis is performed on each reduced map and an ellipse is fit to the normalized autocorrelation plot where the value exceeds 0.2. The aspect ratio and angle of orientation of the ellipse is then measured. If the aspect ratio is 1, then the ellipse (circle) has an orientation of 0°. The properties of the reduced map are then recombined into a 32x32 pixel aspect ratio or orientation map so that local variations in the original modulus map can be detected.

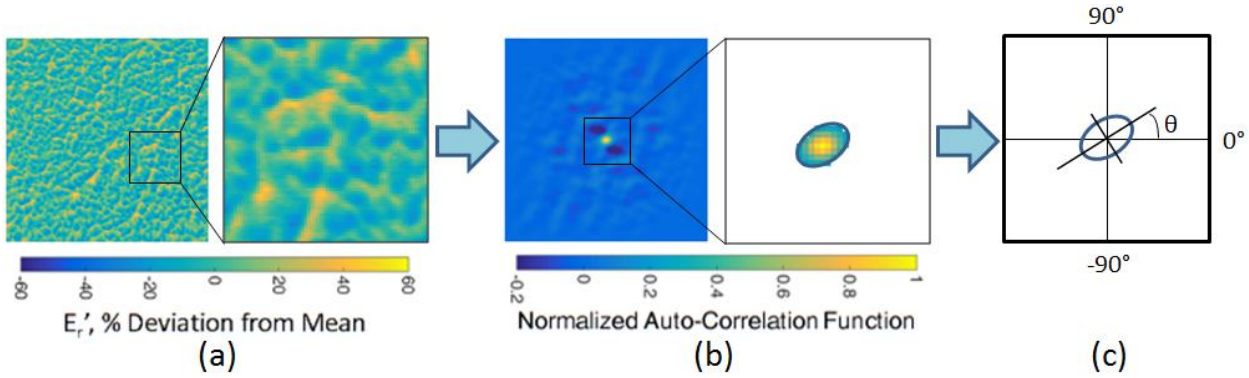

Figure 3.3. (a) A 64x64 pixel region of the 256x256 pixel modulus map is selected. **(b)** The autocorrelation function is performed on the reduced map and an ellipse is fit to the center region where the normalized autocorrelation value is greater than 0.2. **(c)** The aspect ratio and angle of orientation of the long axis of the ellipse are measured.

Analysis using the autocorrelation function and presented in Figure 3.4(c) shows overall directionality in the four maps from the as-cast specimen at a positive angle. The features in Maps 2 and 4 are the most isotropic overall, while those in Maps 1 and 3 are more elongated. Further analysis using subplots of the maps shows distinct domains within the maps of varying aspect ratio (Figure 3.4(d)) and orientation (Figure 3.4(e)). Map 2 is again shown to have nearly isotropic features while there are regions of more elongated features in Maps 1, 3, and 4. The features in Maps 1 and 3 are all oriented at a positive angle while the features are more randomly oriented between positive and negative values in Maps 2 and 4, as shown more clearly in the histogram of the orientation maps in Figure 3.4(f).

(a)

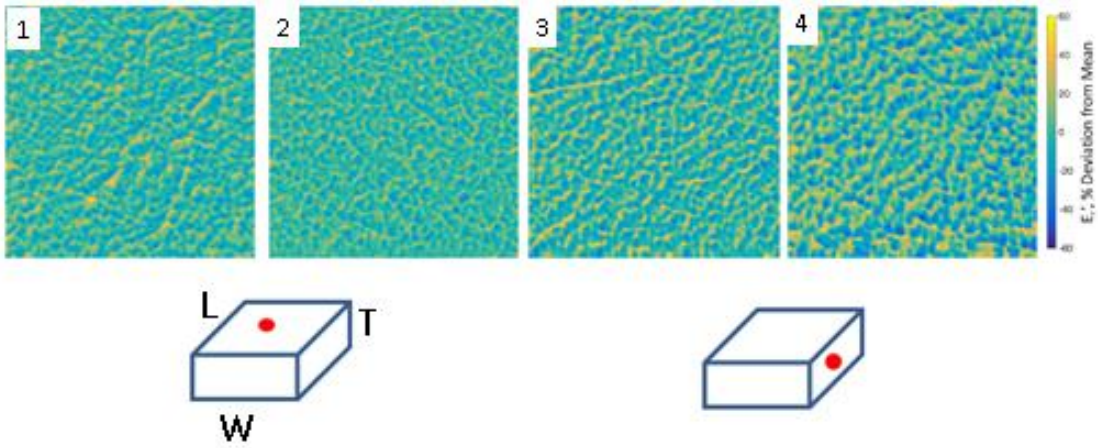
1
2
3
4
L
T
W

(b)

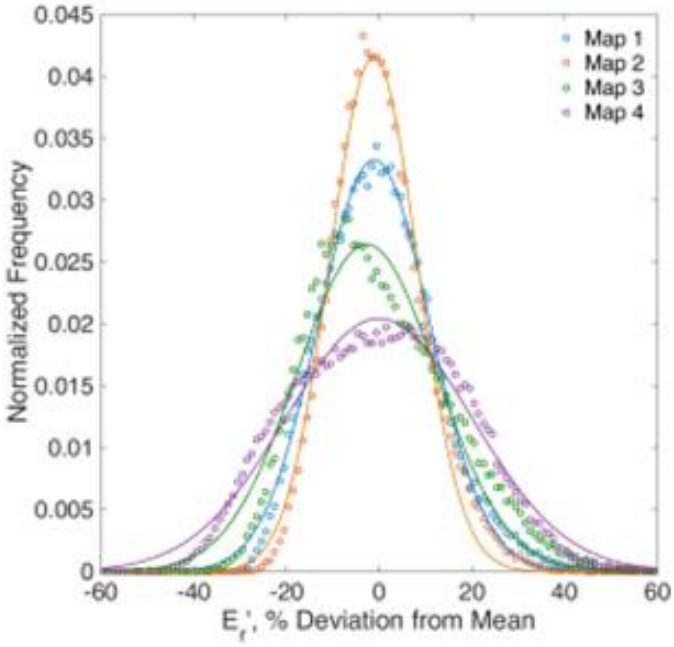
Map 1
Map 2
Map 3
Map 4
Normalized Frequency
0.045
0.04
0.035
0.03
0.025
0.02
0.015
0.01
0.005
0
-60
-40
-20
0
20
40
60
E_r', % Deviation from Mean

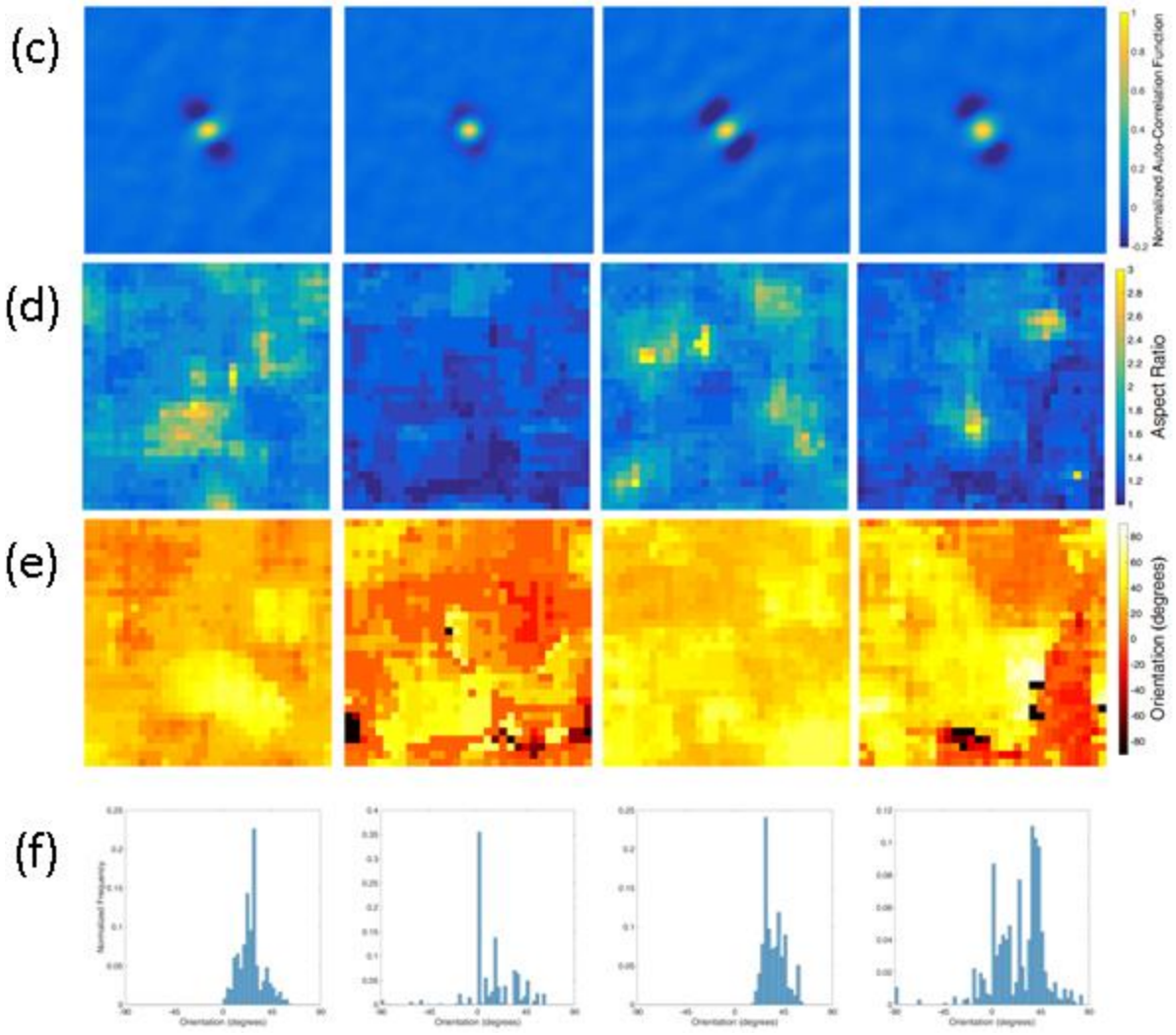

Figure 3.4. (a) Modulus maps of the as-cast BMG rectangular bar. Each map measures 5x5 μm. Maps 1 and 2 were obtained from the LxW face of the plate while Maps 3 and 4 were obtained from the LxT face, as indicated by the cartoons. The corresponding **(b)** modulus distributions, **(c)** normalized autocorrelation function, **(d)** aspect ratio map, **(e)** orientation map, and **(f)** orientation histogram from each map.

Although a Gaussian or Gaussian-like distribution of elastic moduli has been reported before for computational and experimental studies on nanometer-scale heterogeneities in metallic glasses [6,12–14], random errors in measurements can also contribute to the distribution. To evaluate the extent of any random errors in measurement, a modulus map was also obtained from the same silicon wafer used for the nanoindentation experiments. The resulting modulus map and histogram are shown in Figure 3.5. As with the nanoindentation, the modulus map obtained from

the silicon was noticeably more uniform than the maps collected from the BMG shown in Figure 3.4. The histogram of the silicon exhibited a full width at half maximum (FWHM) of 6.2%, compared to a range of 22.6% to 46.0% for the maps of the as-cast BMG shown in Figure 3.4.

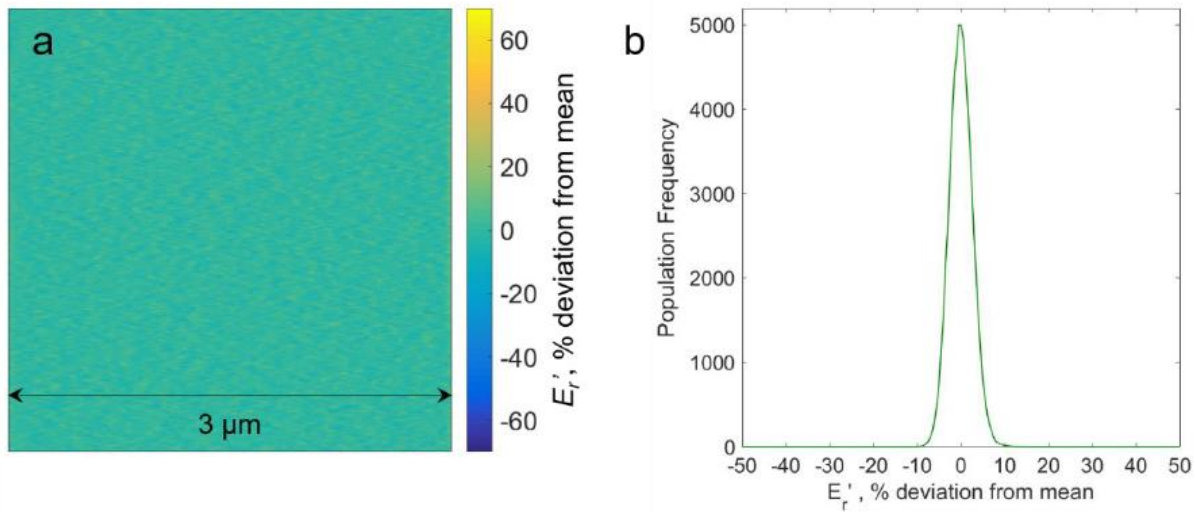

Figure 3.5. Absence of spatial heterogeneities in a structurally homogeneous material. **(a)** 3 µm x 3 µm storage modulus map collected from the surface of a single-crystal silicon wafer grown in the <100> direction and **(b)** corresponding histogram.

After the cold rolling the metallic glass plate, the relationship between the observed elastic fluctuations and a shear band was also investigated. The path of the shear bands was not perfectly straight at the microscale, as can be seen from the scanning probe microscopy image of a shear band intersection in Figure 3.6. This image was acquired after the sample was initially polished and then cold rolled, but before the sample was polished a second time to remove the shear steps. In the undisturbed regions of the SPM image, height fluctuations are observed which are likely a result of the heterogeneities in the glass causing preferential polishing. There is no correlation between the height maps and modulus maps, and previous work in this research group has shown that the topography fluctuations have a different characteristic size than the modulus fluctuations. The height fluctuations seen in Figure 3.6 are exaggerated due to the

scaling of the z-axis, and the average roughness of the topography over 1 μm^2 of the topography map is approximately 2 nm. The path of the shear band seems to be affected by the height fluctuations as the deflections in the shear band path are approximately the same size as the height fluctuations.

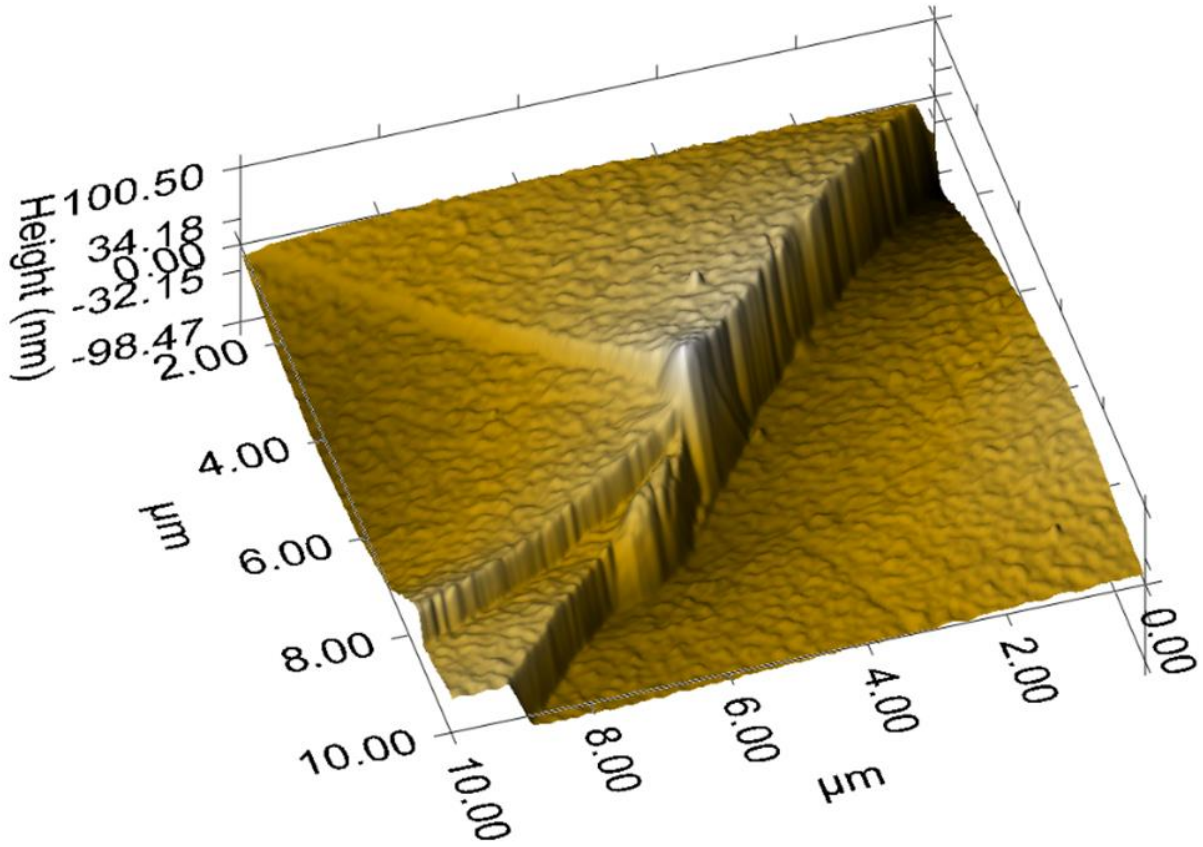

Figure 3.6. Scanning probe microscopy image of the intersection of several shear bands. Note that the scaling of the z-axis is not consistent with the other axes and was increased for emphasis.

In order to determine how the elastic microstructure changes in the vicinity of a shear band, a montage of maps was collected from a region of the sample that was known to contain two intersecting shear bands although the shear steps had been removed by polishing. The montage covered a discontinuous 53x29 µm region and is shown in Figure 3.7(a), where the inset is an SEM image and shows the location of the montage relative to the original placement of the

shear band. Because the sample was polished after the SEM image was acquired, the shear band is probably shifted relative to its original location. As with the previously discussed modulus maps, each map measures 5x5 μm and is normalized to the mean of each respective map. Visually, there is a variation in the elastic microstructure over the entire montage, with different microstructural pockets evident even within the same map. To better see these variations, two maps from the montage are shown again in Figure 3.8 at a greater size. For instance, in the map from on the left in Figure 3.8, the elastic microstructure on the left side of this map appears more diffuse while on the right it looks more defined with the features in both regions oriented in different directions. The map on the right clearly shows elongation of the finer stiffer features in the general direction of the shear band.

The variations in microstructure are further emphasized in the aspect ratio maps in Figure 3.7(b) and the orientation maps in Figure 3.7(c). The angle of the shear band was measured as positive 63° in the SEM image. Regions of higher aspect ratio are more concentrated in the region of the montage extending in the direction of the shear band. However, even in the aspect ratio maps farther away from where the shear band is believed to be, there is still a large degree of variability within and between maps. These observations are the same for the orientation maps. A region of features oriented at a higher positive angle is present in the section of the montage extending parallel to the shear band (in the region between the two maps marked with a ‡ symbol in Figure 3.7(c)). A high degree of variation in orientation is also present, with some maps containing very little variation in orientation and other maps containing pockets of higher and lower orientation. Although the elastic microstructure appears to be continuous across the boundaries between the individual modulus maps, the aspect ratio and orientation values are not always coherent at the boundary between maps due to the edge effects inherent in analysis.

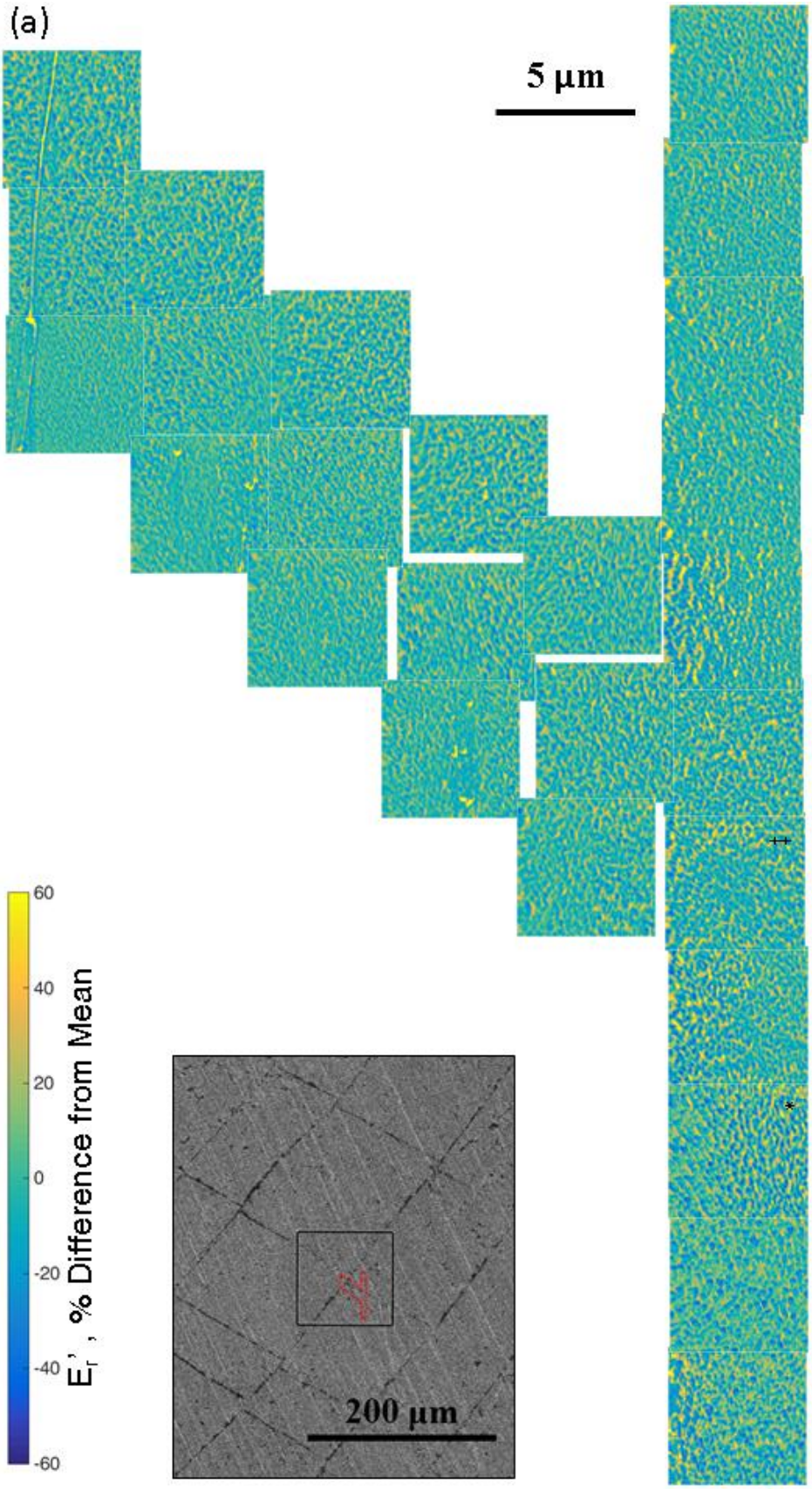
(a)
5 µm
60
40
20
0
-20
-40
-60
E_r', % Difference from Mean
200 µm

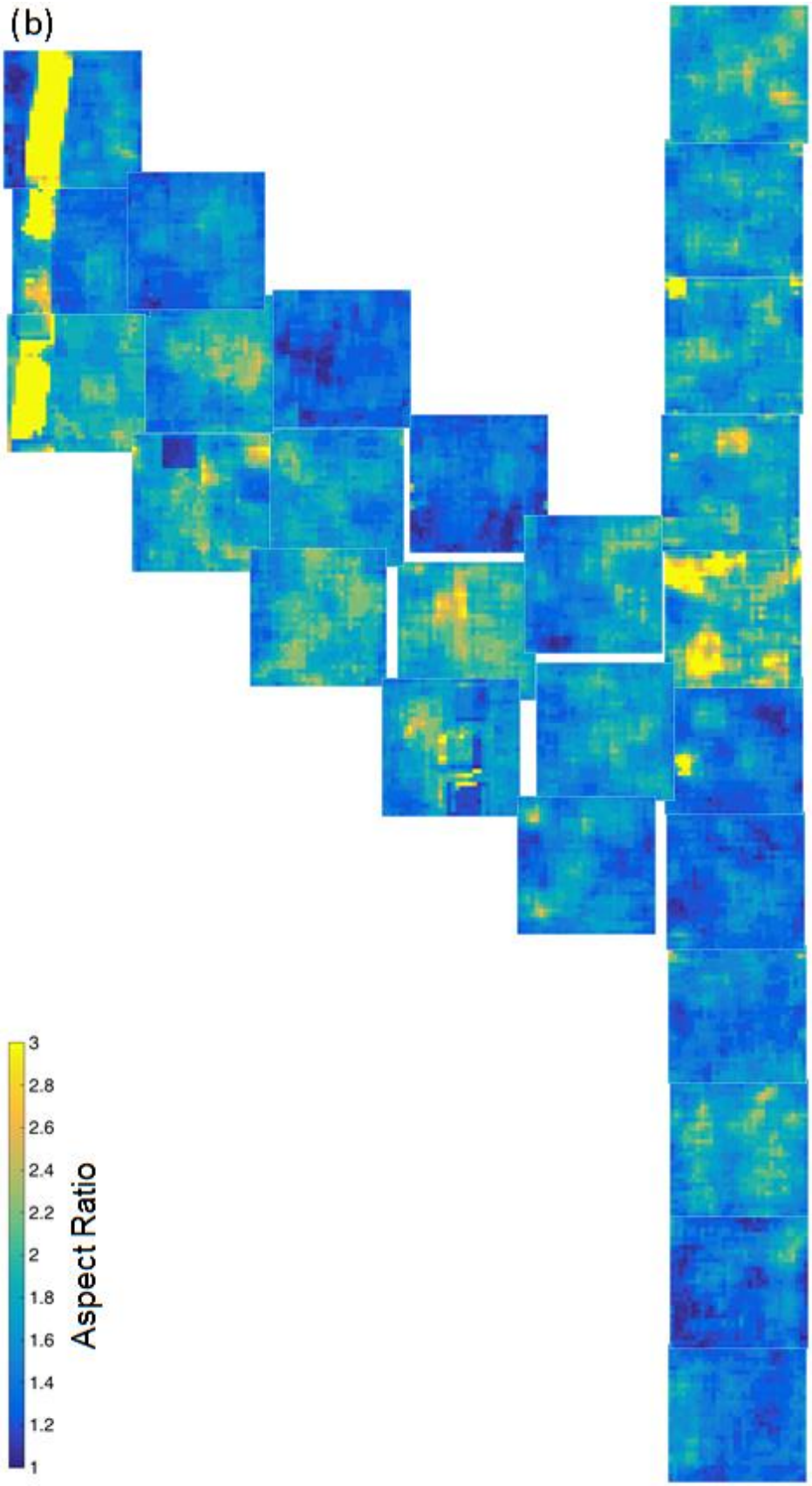
(b)
3
2.8
2.6
2.4
2.2
2
1.8
1.6
1.4
1.2
1
Aspect Ratio

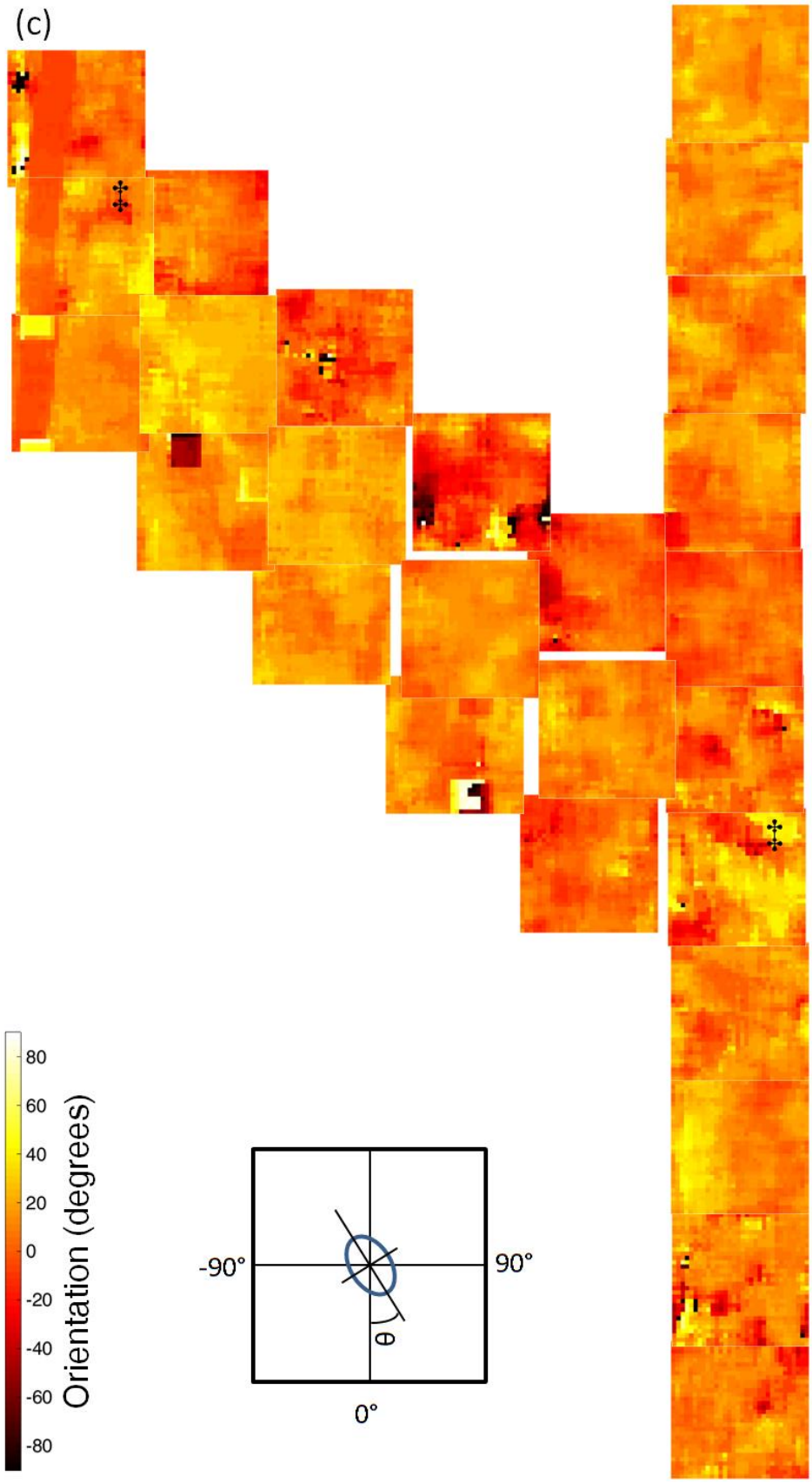
(c)
80
60
40
20
0
-20
-40
-60
-80
Orientation (degrees)
-90°
90°
0°
θ

Figure 3.7. (a) Modulus maps of the monolithic metallic glass obtained over a shear band. Each map measures 5x5 μm. The two maps marked with * and ‡ symbols are shown in Figure 3.8. The inset is an SEM image with the mapped region outlined. **(b)** Corresponding aspect ratio maps. **(c)** Corresponding orientation maps. The vertically linear mark traversing the three left-most maps is a scratch on the sample surface (created post-polishing) and not indicative of the elastic microstructure of the BMG.

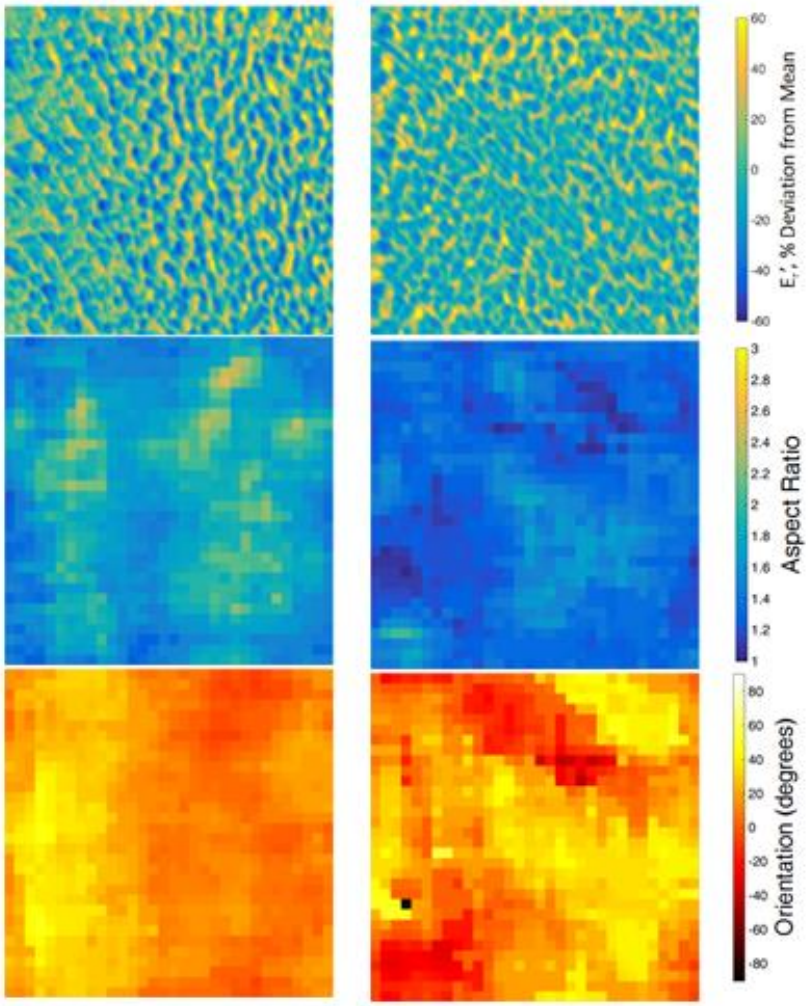

Figure 3.8. Two selected maps from the montage highlighting different domains within the maps of varying aspect ratio and orientation.

3.4. Discussion

The nanoindentation hardness and modulus measurements on the monolithic BMG exhibited a wide distribution, as was shown particularly in Figure 3.1(e-f) when compared to a silicon standard. By taking the distribution in properties for the ideally homogeneous single

crystal silicon to be indicative of random errors inherent in the measurement, the greater variation in properties in the BMG can be assumed to be directly caused by heterogeneities in the material itself.

The linear scaling observed between E_r and H shown in Figure 3.2 has been similarly observed in a previous study that found a linear relationship between Vickers hardness and shear modulus for a number of compositionally distinct BMGs [15]. They found that the relationship $H_v = 0.151G$ satisfied data from 37 compositionally distinct alloys, while in this study the data was well fit by $H \approx (0.06 - 0.08)E_r$. In contrast to the BMG data collected here, there was no correlation between H and E_r for the single crystal silicon, which is indicative of its structural and chemical homogeneity. The consistency in the linear fit for all of the data acquired here, as well as the phenomenological agreement with the previous study of compositionally different BMGs [15], strongly suggests that the spatial variations in indentation modulus and hardness are largely due to spatial compositional fluctuations. Essentially, each indent is sampling a compositionally distinct region of the BMG, resulting in a continuous spread of values along the trendline reminiscent of the variation observed in the previous study [15] due to composition. This notion is further reinforced by the increase in scatter in the data when the indentation load, and thus the interaction volume of the indent, decreases. Assuming that the maximum depth of the indent is proportional to the interaction volume, the corresponding maximum depths for the 8, 4, and 1.2 mN indents were 239.7, 163.6, and 80.3 nm. When the maximum depth or interaction volume is larger, more chemically distinct regions are sampled in the indentation measurement and the resulting measurement is an average of the heterogeneities within that volume. When the maximum depth or interaction volume decreases, however, fewer chemically

distinct areas are sampled and the measurement is more representative of the local properties in that area.

Annealing the BMG caused an increase in both hardness and modulus (Figure 3.2) as well as a slight broadening of the distribution of those properties (Figure 3.1). A slight narrowing in the distribution would be expected, as was shown in Figure 3.1(e-f) because β-relaxation during annealing creates an increase in the overall atomic packing efficiency [7,16,17]. When a metallic glass is fabricated through rapid quenching, a dense population of topologically unstable atomic clusters forms a rigid elastic backbone encompassing pockets of liquid-like regions [18]. During annealing, β-relaxation causes the unstable regions to rearrange into more stable and efficiently packed configurations. This increases the rigidity of the elastic backbone and makes the initiation of plastic flow more difficult. This creates a more uniform structure, although spatial compositional fluctuations persist. The slight broadening that was seen for the plate sample in Figure 3.1(c-d) is most likely due to the increased size of the indents in this sample probing larger scale heterogeneities and is indicative of heterogeneities present at multiple length scales.

The spatial property fluctuations observed through nanoindentation were on the order of several microns. This length scale is very large compared to potential variations due to features such as atomic clusters and shear transformation zones, and the variation at this length scale appears to be random. In order to investigate smaller scale variations in elastic properties, DMM can be used to map features with sizes of less than 100 nanometers. In the analysis presented here, the maps are normalized to the mean of each respective map because the average storage modulus varies between maps, consistent with the nanoindentation. Heterogeneity in the elastic properties was observed in the maps of the as-cast sample shown in Figure 3.4 and in the

deformed sample shown in Figure 3.7. These heterogeneities formed an interconnected stiff network encompassing pockets of more compliant material. Interestingly the distribution in modulus is much larger at this length scale than for the nanoindentation results (compare Figure 3.1(c) to Figure 3.4(b)). This again reinforces the notion that the properties measured via nanoindentation at the larger length scale are from sampling a variety of hard and soft features that become averaged together. At this length scale, the elastic fluctuations are not randomly distributed, but instead form a distinct microstructure with measurable variations in feature aspect ratio and orientation both within and between maps, as shown in Figure 3.4 and Figure 3.7. While the entire sample has been confirmed to be single-phase amorphous, these domains of microstructural variability are reminiscent of two-phase amorphous structures that form from chemical segregation, which has been reported for a number of metallic glasses [19]. This is in agreement with the earlier finding that the variations in nanoindentation properties are due to chemical variations. In one study on $Cu_{46}Zr_{47-x}Y_xAl_7$ metallic glass, they found that a two phase amorphous composite was created when the Y content exceeded 15% [20]. This two-phase amorphous composite exhibited extreme brittleness; however, when the Y content was between 2% and 5%, the metallic glass exhibited enhanced plasticity due to chemical heterogeneities from the positive enthalpy of mixing between the Y and Zr. The effect of chemical heterogeneity on mechanical behavior is still poorly understood. However, now that we are beginning to understand the elastic microstructure at this length scale which is likely a result of chemical heterogeneity, we can begin to exploit it to design tougher glasses, similar to polycrystalline metals where optimizing grain size to achieve desired properties is common practice.

The primary difference between the elastic microstructure presented here and heterogeneities observed in previous studies [5,6,14] is the length scale of the observed

fluctuations. The resolution of the dynamic modulus technique as performed here is approximately 70 nm, so discernable features in these maps are greater than this limit. Other studies using various atomic force microscopy methods reported much smaller feature sizes from structural heterogeneities, on the order of 2 to 50 nanometers [4–6,12]. Molecular dynamics models have estimated the diameter of a shear transformation zone to be 1.5 nm [21]. Similarly, molecular dynamic studies have also reported soft spots in metallic glasses on the order of a few nanometers [8]. The length scales reported from the atomic force microscopy studies are more consistent with those of these structural features. The elastic microstructure observed here may be due to a networked structure of the nanometer-scale heterogeneities observed elsewhere. Furthermore, the elastic heterogeneities observed within the modulus map are also present within larger scale fluctuations in the modulus and hardness over several microns, as was shown in the nanoindentation data presented here. Heterogeneities on the order of millimeters have also been reported, leading to improved ductility and toughness [22]. This demonstration of variability in size of the characteristic microstructural features, from this work and others just mentioned, suggest the existence of a hierarchy in heterogeneity in metallic glasses that can span from single nanometers to millimeters.

The potential for the elastic microstructure to affect and be affected by a shear band was also investigated here. Previous nanoindentation studies have shown long range variation of properties on the order of tens of micrometers away from a shear band [23,24], thus it would be expected that a shear band could also cause local changes in the elastic microstructure. The scanning probe microscopy image of a shear band shown in Figure 3.6 shows the pathway of the shear band deflecting around the measured height fluctuations, which are likely due to preferential polishing caused by the elastic heterogeneities. Ideally, larger heterogeneities would

cause more deflection in the path of a shear band, hindering its propagation and potentially inducing increased ductility. Because it is well established that shear band propagation causes a rise in temperature [25], it would be expected that this temperature gradient cause changes to the orientation and aspect ratio of the surrounding microstructural features. If the shear band causes local melting and requenching, a refined microstructure would be expected. If the shear band causes local heating without melting, a coarsened microstructure could be produced. The aspect ratio maps in Figure 3.7(b) do show areas of higher aspect ratio in the collection of maps extending in the direction of the shear band. Areas of higher positive orientation exist in these maps as well, although the higher orientations in the maps are only at angles of 45° while the shear band was measured to have an angle of 63°. There are several potential reasons as to why more definitive traces of the shear band are not found in the elastic microstructure of the map montage. First, the reduced area maps that were used in the analysis could potentially still be too large to identify single features on the order of a shear band, which has been reported to have a thickness of 20 nm and a corresponding thermal diffusion width of 100 to 240 nm [25]. Second, the shear band might have been too weak to cause significant microstructural changes. In the SEM image of the shear band in the inset of Figure 3.7(a), the particular shear band that is being mapped is not as well defined as other shear bands in the vicinity, potentially carrying less strain than the other shear bands and unable to create disturbances in the surrounding microstructure. Mapping across a stronger shear band could reveal more significant microstructural changes.

3.5. Conclusions

In summary, using the two techniques of nanoindentation and dynamic modulus mapping, heterogeneities in a Zr-based metallic glass were observed at two length scales. At the micrometer level, heterogeneities are randomly spatially arranged, but the hardness and modulus

exhibit a linear relationship. This linear scaling is indicative of the variations in properties being caused by compositional fluctuations in the metallic glass. Isothermal annealing treatment at a temperature below the glass transition increased the average values of indentation hardness and modulus but reduced the overall degree of heterogeneity in the alloy. Superimposed on these variations, at the sub-micron scale, an "elastic microstructure" was observed, leading to the notion of a hierarchy of heterogeneities in metallic glasses. Variations in aspect ratio and orientation of the features were also observed in the modulus maps, indicating different domains are present in the microstructure as well. Modulus mapping in the vicinity of a shear band showed some alignment in microstructural domains of higher aspect ratio and orientation angle in the general direction of the shear band. This work demonstrates the existence of heterogeneities in a Zr-based metallic glass at multiple length scales, including the presence of an elastic microstructure, and provides a new experimental approach for studying the microstructure of BMGs with a view towards improving the ductility and structural reliability of these materials.

3.6. References

[1] Y.Q. Cheng, E. Ma, Atomic-level structure and structure-property relationship in metallic glasses, Prog. Mater. Sci. 56 (2011) 379–473. doi:10.1016/j.pmatsci.2010.12.002.

[2] J.J. Lewandowski, W.. Wang, A.L. Greer, Intrinsic plasticity or brittleness of metallic glasses, Philos. Mag. Lett. 85 (2005) 77–87. doi:10.1080/09500830500080474.

[3] K.J. Laws, D.B. Miracle, M. Ferry, A predictive structural model for bulk metallic glasses., Nat. Commun. 6 (2015) 8123. doi:10.1038/ncomms9123.

[4] Y. Yang, J.F. Zeng, A. Volland, J.J. Blandin, S. Gravier, C.T. Liu, Fractal Growth of the Dense-packing Phase in Annealed Metallic Glass Imaged by High-resolution Atomic Force Microscopy, Acta Mater. 60 (2012) 5260–5272. doi:10.1016/j.actamat.2012.06.025.

[5] Y.H. Liu, D. Wang, K. Nakajima, W. Zhang, A. Hirata, T. Nishi, A. Inoue, M.W. Chen, Characterization of nanoscale mechanical heterogeneity in a metallic glass by dynamic force microscopy, Phys. Rev. Lett. 106 (2011) 1–4. doi:10.1103/PhysRevLett.106.125504.

[6] H. Wagner, D. Bedorf, S. Küchemann, M. Schwabe, B. Zhang, W. Arnold, K. Samwer, Local Elastic Properties of a Metallic Glass, Nat. Mater. 10 (2011) 439–442.

doi:10.1038/nmat3024.

[7] F. Zhu, H.K. Nguyen, S.X. Song, D.P.B. Aji, A. Hirata, H. Wang, K. Nakajima, M.W. Chen, Intrinsic correlation between β-relaxation and spatial heterogeneity in a metallic glass, Nat. Commun. 7 (2016) 11516. doi:10.1038/ncomms11516.

[8] E. Ma, Tuning order in disorder, Nat. Mater. 14 (2015) 547–552. doi:10.1038/nmat4300.

[9] E. Ma, J. Ding, Tailoring structural inhomogeneities in metallic glasses to enable tensile ductility at room temperature, Mater. Today. (2016). doi:10.1016/j.mattod.2016.04.001.

[10] Y. Wang, M. Li, J. Xu, Toughen and harden metallic glass through designing statistical heterogeneity, Scr. Mater. 113 (2016) 10–13. doi:10.1016/j.scriptamat.2015.09.038.

[11] C.C. Hays, J. Schroers, W.L. Johnson, T.J. Rathz, R.W. Hyers, J.R. Rogers, M.B. Robinson, Vitrification and determination of the crystallization time scales of the bulk-metallic-glass-forming liquid Zr58.5Nb2.8Cu15.6Ni12.8Al 10.3, Appl. Phys. Lett. 79 (2001) 1605–1607. doi:10.1063/1.1398605.

[12] H.B. Ke, J.F. Zeng, C.T. Liu, Y. Yang, Structure Heterogeneity in Metallic Glass: Modeling and Experiment, J. Mater. Sci. Technol. 30 (2014) 560–565. doi:10.1016/j.jmst.2013.11.014.

[13] H. Mizuno, S. Mossa, J.L. Barrat, Measuring spatial distribution of the local elastic modulus in glasses, Phys. Rev. E - Stat. Nonlinear, Soft Matter Phys. 87 (2013) 42306. doi:10.1103/PhysRevE.87.042306.

[14] Y. Fan, T. Iwashita, T. Egami, Evolution of elastic heterogeneity during aging in metallic glasses, Phys. Rev. E. 89 (2014) 62313. doi:10.1103/PhysRevE.89.062313.

[15] X.Q. Chen, H. Niu, D. Li, Y. Li, Modeling hardness of polycrystalline materials and bulk metallic glasses, Intermetallics. 19 (2011) 1275–1281. doi:10.1016/j.intermet.2011.03.026.

[16] P. Murali, U. Ramamurty, Embrittlement of a bulk metallic glass due to sub-Tg annealing, Acta Mater. 53 (2005) 1467–1478. doi:10.1016/j.actamat.2004.11.040.

[17] J. Qiao, J. Pelletier, R. Casalini, U. De Lyon, M. Umr, F.- Villeurbanne, Relaxation of Bulk Metallic Glasses Studied by Mechanical Spectroscopy, J. Phys. Chem. B. 117 (2013) 13658–13666.

[18] W.H. Wang, Y. Yang, T.G. Nieh, C.T. Liu, On the source of plastic flow in metallic glasses: Concepts and models, Intermetallics. 67 (2015) 81–86. doi:10.1016/j.intermet.2015.08.004.

[19] J. Eckert, J. Das, S. Pauly, C. Duhamel, Mechanical Properties of Bulk Metallic Glasses and Composites, J. Mater. Res. 22 (2011) 285–301. doi:10.1557/jmr.2007.0050.

[20] E.S. Park, D.H. Kim, Phase separation and enhancement of plasticity in Cu-Zr-Al-Y bulk metallic glasses, Acta Mater. 54 (2006) 2597–2604. doi:10.1016/j.actamat.2005.12.020.

[21] M. Zink, K. Samwer, W.L. Johnson, S.G. Mayr, Plastic deformation of metallic glasses: Size of shear transformation zones from molecular dynamics simulations, Phys. Rev. B. 73 (2006) 2–4. doi:10.1103/PhysRevB.73.172203.

[22] S. Scudino, B. Jerliu, S. Pauly, K.B. Surreddi, U. Kühn, J. Eckert, Ductile bulk metallic glasses produced through designed heterogeneities, Scr. Mater. 65 (2011) 815–818. doi:10.1016/j.scriptamat.2011.07.039.

[23] R. Maaß, K. Samwer, W. Arnold, C. a. Volkert, A single shear band in a metallic glass: Local core and wide soft zone, Appl. Phys. Lett. 105 (2014) 171902. doi:10.1063/1.4900791.

[24] R. Maass, P. Birckigt, C. Borchers, K. Samwer, C.A. Volkert, Long range stress fields and cavitation along a shear band in a metallic glass: The local origin of fracture, Acta Mater. 98 (2015) 94–102. doi:10.1016/j.actamat.2015.06.062.

[25] J.J. Lewandowski, A.L. Greer, Temperature Rise at Shear Bands in Metallic Glasses, Nat. Mater. 5 (2006) 15–18. doi:10.1038/nmat1536.

Chapter 4: Heterogeneity in As-Cast and Deformed Bulk Metallic Glass Composites

Portions of this chapter are adapted from the following publication: J.A. Kolodziejska, H. Kozachkov, K. Kranjc, A. Hunter, E. Marquis, W.L. Johnson, K.M. Flores, D.C. Hofmann, Towards an understanding of tensile deformation in Ti-based bulk metallic glass matrix composites with BCC dendrites, Sci. Rep. 6 (2016) 22563 [108]. Sample casting and tensile testing were performed by J.A. Kolodziejska and H. Kozachkov. TEM analysis was performed by A. Hunter. SEM, nanoindentation, and modulus mapping was performed by K. Kranjc.

4.1. Introduction

Bulk metallic glass composites (BMGCs) have attracted considerable attention in recent years due to their improved ductility and toughness over monolithic glasses while maintaining a high strength, thus increasing their viability as structural materials [1]. Various classes of BMGCs have been investigated, such as ex situ composites [2,3] and in situ composites with crystalline dendrites [4–6]. Of these, in situ Ti and Zr-based dendritic BMGCs have demonstrated an exemplary and unique blend of properties and processibility. Moreover, the dendritic volume fraction and composition can be controlled through tuning the overall composite composition [7] while the dendrite morphology can be tailored using semisolid processing [8] and Bridgman solidification [9]. BMGCs with benchmark ductility and fracture toughness have been achieved using this approach [6].

As described in Section 1.5, one of the general rules of designing a tough and ductile BMGC is that the dendrite phase have a lower modulus than that of the glass phase so that they can hinder the propagation of shear bands and cracks in the glass matrix [1,10–15]. In Ti and Zr-based in situ composites, a more compliant dendritic phase can be achieved through the use of a β–stabilizing element (e.g. vanadium, niobium, or tantalum), which stabilizes the dendrites in the high temperature BCC (β) phase. However, since the total concentration of β–stabilizer affects

the properties of both the crystalline dendrite and the glass matrix, it is difficult to quantify the dependence of the bulk composite properties on the β–stabilizer concentration.

This study explored the effects of the β–stabilizing element vanadium on the resultant mechanical properties of the alloy series. To this end, a novel series of Ti-Zr-Cu-Be-V BMGC alloys with β–titanium BCC dendrites was designed for this investigation. The alloy series encompassed a broad range of β–stabilizer concentration (0 – 12%) while maintaining a near-constant dendrite volume fraction, a combination that has previously proven difficult to attain [16]. This alloy series was predicated on the alloy originally called DV1, but here referred to as V12, whose composition is given in Table 4.1. This alloy was previously extensively explored and found to have excellent glass-forming ability as well as a high yield strength and total tensile elongation of 1.362 GPa and 12.5%, respectively [16]. Three of the component elements, Ti, Zr, and V, readily form a solid solution while Cu and Be have limited solubility in the dendritic β–phase. Therefore, the dendritic volume fraction of these alloys is primarily dependent on the ratio of these two groups of elements [4,7]. Removing all of the β–stabilizing vanadium from the V12 alloy and slightly adjusting the composition produced the V0 alloy, a quaternary BMGC with sufficient glass-forming ability and similar dendritic volume fraction to V12. Increasing the vanadium content in 2 at% increments from V0 while holding the Ti-Zr-V/Cu-Be ratio constant produced the V series of alloys, V0 – V10, whose compositions are shown in Table 4.1. The V12 alloy is offset from the compositional formula by only 1 at% titanium and zirconium. Alloys with vanadium concentrations higher than 12 at% were not investigated due to their limited glass-forming ability.

4.2. Experimental Procedure

The BMGC samples used in this study were prepared via arc melting by a collaborator at the NASA Jet Propulsion Laboratory. Table 4.1 shows the nominal compositions of all of the alloys prepared by this collaborator. The samples were cast into 4 x 4 mm rods and then machined into tensile bars with square gauge sections 2 mm in width and 8 mm in length. The samples were loaded in tension using an Instron 5969 universal testing machine at a constant displacement rate of 0.2 mm/min until failure. Strain in the gauge section was monitored with a clip-on extensometer. The mechanical data from those samples is shown in Figure 4.2. The samples were acquired after the tensile testing in order to perform nanoindentation and dynamic modulus mapping. A low-speed diamond wet saw was used to section off the grip region and the necked region of the tested tensile bars. These pieces were then ground using a series of silicon carbide papers from 400 to 1200 grit. The samples were then given a final polish using 0.05 μm colloidal silica to achieve a mirror finish.

In order to acquire mechanical properties of the individual phases of the BMGCs, nanoindentation was performed using the Hysitron TI950 Triboindenter system described in Section 2.3. A diamond Berkovich probe was used to indent each phase at least one indent diameter away from the interface. Each phase was tested to a maximum depth of 100 nm with loading and unloading displacement rates of 20 nm/s. Each load-displacement curve was analyzed according to the methods described in Section 2.3. The nanoindentation was performed on both the center of the grip region, which was assumed to be in an as-cast, undeformed state, and on the gauge section within 100 μm of the fracture surface.

Table 4.1. Nominal compositions of the V series alloys.

Alloy Name	Ti (at%)	Zr (at%)	Cu (at%)	V (at%)	Be (at%)
VX	53 – 0.5X	27 – 0.5X	5	X = 0, 2, 4, 6, 8, 10	15
DV1/V12	48	20	5	12	15

Dynamic modulus mapping was also performed on both the grip (undeformed) and necked (deformed) sections of the tested tensile bars. Each map was 5x5 μm and was obtained as described in Section 2.4.

4.3. Results

SEM analysis on the center of the cross-section of the grip region (Figure 4.1) shows that the dendrite morphology is consistent for all of the alloys. The dendritic volume fraction is similar, though not identical, for all of the alloy compositions, as predicted from maintaining the Ti-Zr-V/Cu-Be ratio constant. As indicated in Figure 4.1, the dendrite volume fraction decreased with vanadium content between V0 and V8, from 63% to 55% by area. After the minimum at V8, the volume fraction increased to 57% and 58% by area for V10 and V12, respectively. XRD analysis exhibited distinct BCC peaks for all of the alloys, confirming that each contained β dendrites. One alloy in the series, V0, also exhibited an additional clear, non-BCC peak.

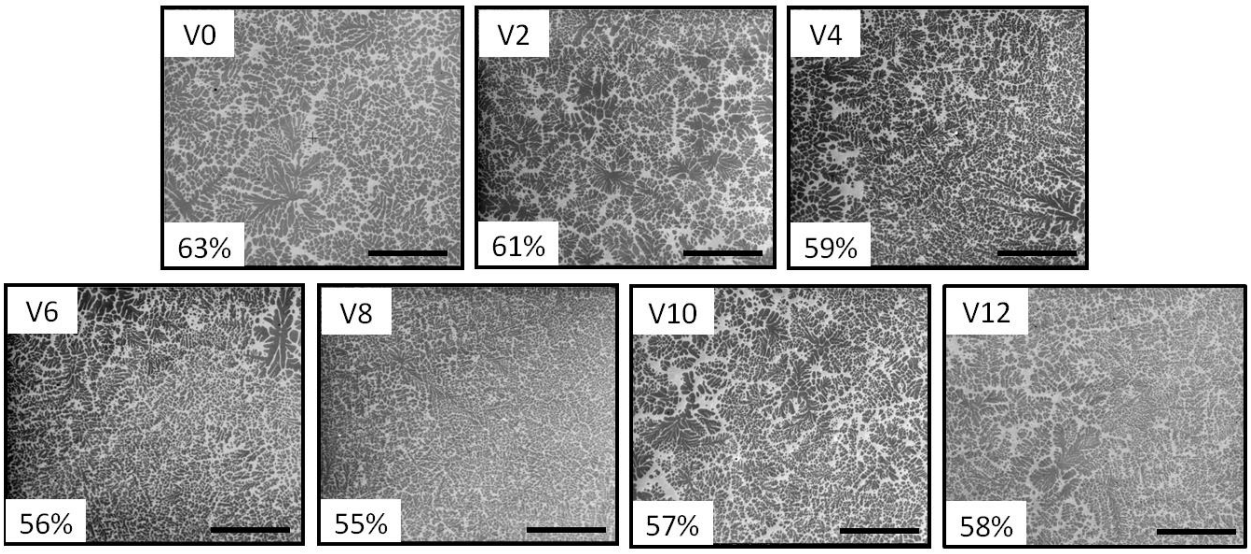

Figure 4.1. SEM images demonstrating the consistency in microstructure among the V series alloys despite their compositional differences. The measured dendritic volume percentage is shown at the bottom left corner of each image. Scale bar = 50 μm. [17]

Engineering stress-strain curves are presented in Figure 4.2, and show that the V series alloys display a wide variety of macroscale mechanical behavior. V0 exhibited the highest ultimate tensile strength (σ_{max}), but also the lowest plastic strain. V2 through V10 all exhibited lower ultimate tensile strength and more extensive tensile ductility than V0. Moreover, V2 through V10 exhibited varying post-yield behaviors, including strain hardening (V2) and strain softening (V4 through V12) to different degrees. Excluding V0, the ultimate tensile strength, the plastic strain, and the degree of strain softening (as roughly parameterized by the slope of the stress-strain curve after σ_{max}), reached a minimum at V8.

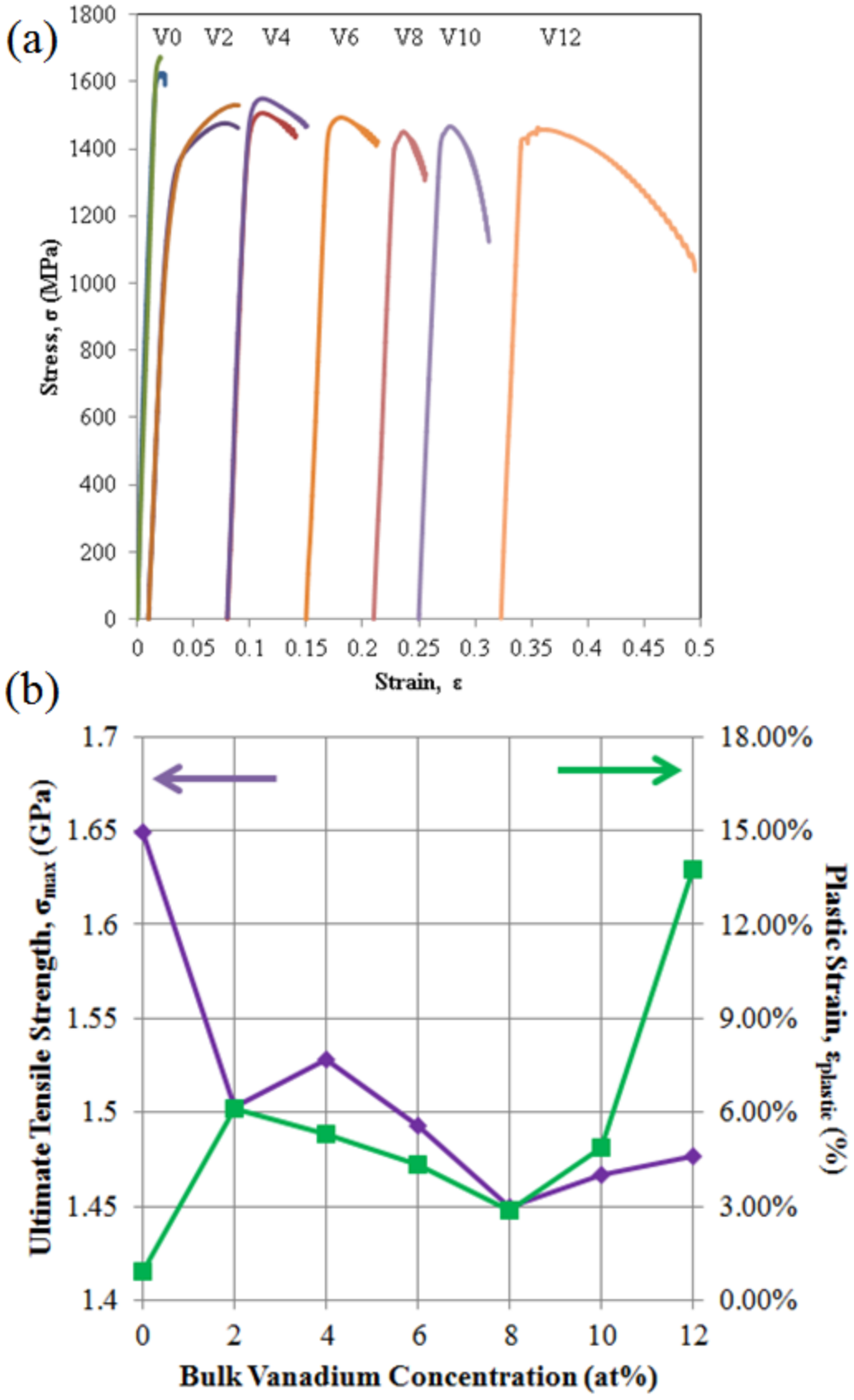
(a)
V0
V2
V4
V6
V8
V10
V12
Stress, σ (MPa)
Strain, ε
(b)
Ultimate Tensile Strength, σmax (GPa)
Plastic Strain, εplastic (%)
Bulk Vanadium Concentration (at%)

Figure 4.2. (a) Engineering stress-strain behavior of the V series alloys showing the range of mechanical behavior observed due to incremental 2% additions of vanadium. **(b)** Plot of ultimate tensile strength (purple) and plastic strain (green) measured from the stress-strain curves. (Tensile testing was performed by collaborators at CalTech.) [17]

The post-deformation TEM micrographs in Figure 4.3 show extensive twinning and dislocations present in the V12 dendrites. For V6, dislocations were observed in the dendrite with little evidence of twinning. This lack of twinning in the dendrite corresponds to pronounced strain softening and necking instability in the composite. Twinning and dislocations were found in the V2 dendrites. The V0 micrograph showed the presence of dislocations in the dendrites.

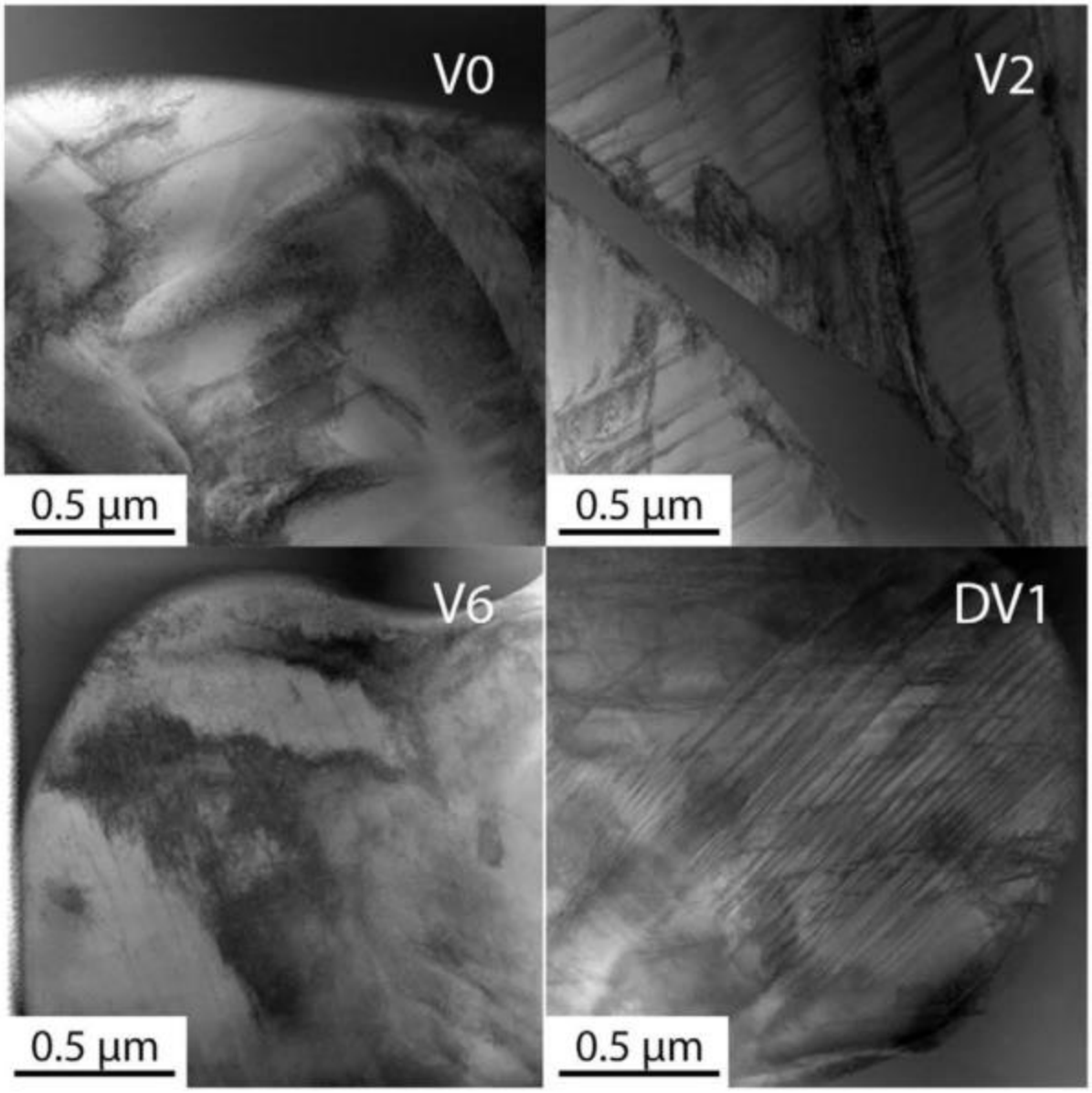

Figure 4.3. Post-deformation TEM micrographs show the range of deformation mechanisms exhibited in the dendrites of the V0, V2, V6, and V12 alloys [17]. Dislocations and extensive twinning are observed in the DV1/V12 and V2 alloys. V6 shows little evidence of twinning, with dislocations as the primary deformation mechanism. Dislocations were also present in the V0 dendrites. (TEM was performed by A. Hunter at U. of Michigan.)

In order to determine any correlation between the composite behavior and the individual phase properties, nanoindentation was used to obtain modulus and hardness values of the dendritic and amorphous matrix phases for each of the V series composites. The nanoindentation

results are shown in Figure 4.4. Looking at the results from the undeformed composite obtained from the grip of the tensile bar, the V0 composite exhibits a higher modulus in the dendrite than the glass, and the hardness of the matrix is higher than that of the dendrite by approximately 1 GPa. For V2 through V12, the modulus of the matrix is higher than that of the dendrite and the ratio of the matrix to dendrite hardness is increased from V0. The nanoindentation was performed again near the neck or fracture surface of V0 – V10. While the indentation properties here were still not reflective of the bulk composite strength and ductility, the difference between the modulus of the dendrite and of the matrix tended to decreased near the fracture surface.

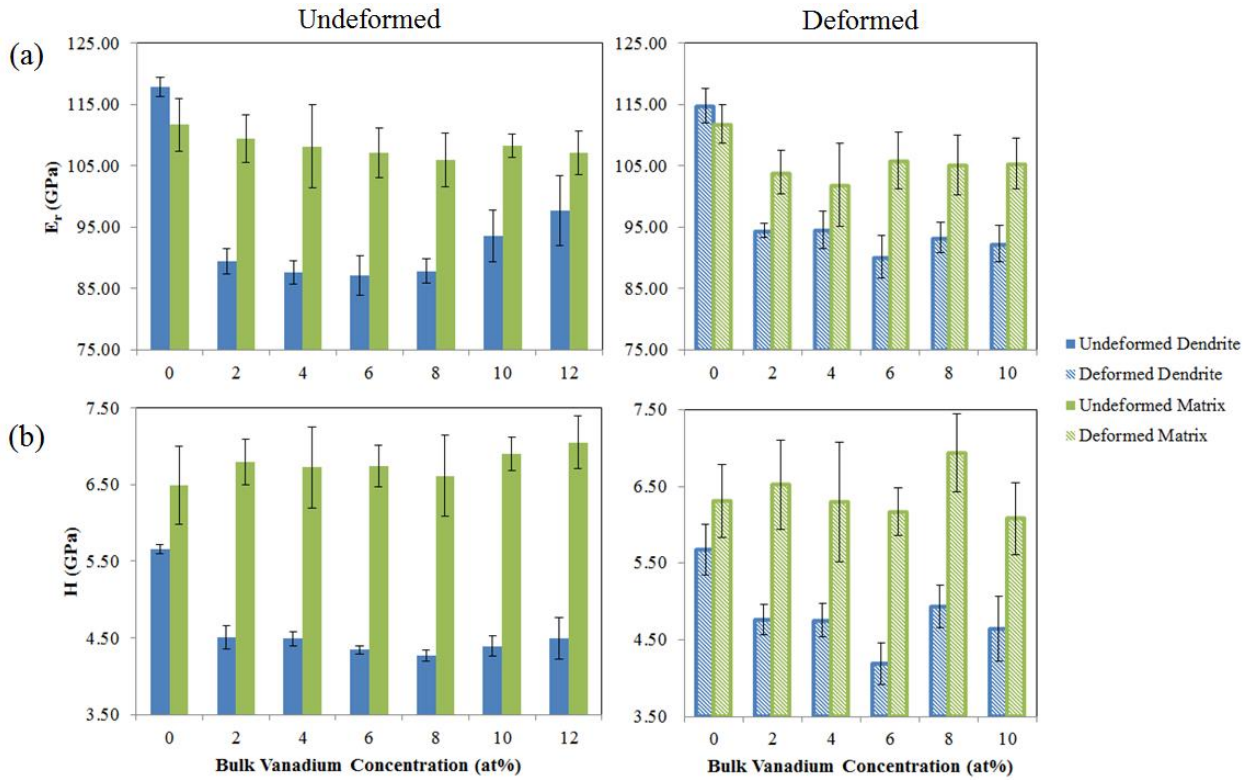

Figure 4.4. Plots of **(a)** reduced modulus and **(b)** hardness for both the crystalline dendritic and amorphous matrix phases of the V series alloys.

Modulus maps of V2, V4, and V6 acquired at the undeformed grip section of the tensile bars are shown in Figure 4.5(a). These composites specifically are shown because of their

transition of bulk mechanical properties: V2 is the only composite that exhibited strain hardening, which transitioned into strain softening behavior in V4 and V6 with a decline in plastic strain and strength between V4 and V6. The heterogeneities in the V2 map are much more pronounced than in either the V4 or V6 maps, which appear much more homogeneous. The modulus distributions for the matrix phase vary between the three composites, as shown in Figure 4.5(b). There is a slight tail or second peak on the low side of these distributions, which is most likely due to dendrite influence at the interface. Each dataset was fit with a Gaussian distribution, which captured the main peak and was not overly influenced by the aforementioned slight tail or second peak. The full width at half maximum (FWHM) of the Gaussian fit for V2, V4, and V6 was measured to be 19.3%, 14.6%, and 12.3%, respectively. By comparison, the distributions of the dendrite phase are much more consistent, with FWHMs of 8.8%, 10.6%, and 10.7% for V2, V4, and V6, respectively. As a reminder from Chapter 3, the FWHM of the structurally homogeneous silicon standard was 6.2%.

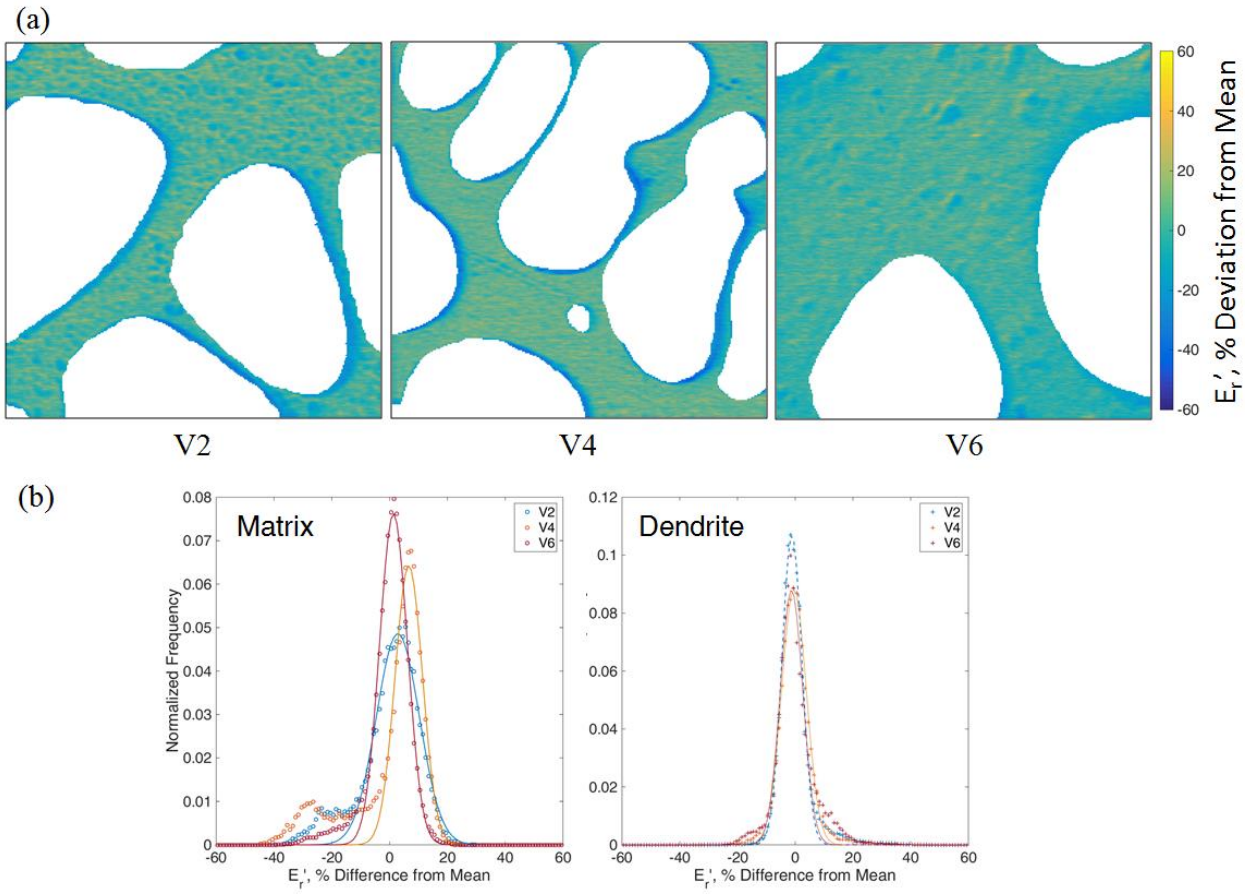

Figure 4.5. (a) Modulus maps of three of the V series composites, V2, V4, and V6, acquired from the undeformed grip section. The dendrite phase has been removed from the maps so that only the glass matrix is shown. Each map measures 5 x 5 μm. **(b)** Histograms of the glass matrix and dendrite modulus values, each normalized to their own respective mean.

The modulus maps of the same alloys V2, V4, and V6 acquired near the fracture surface are shown in Figure 4.6. The heterogeneities appear more distinct in all three of the maps from the fracture region as opposed to those from the undeformed region. The histograms of the maps from the fracture region show once again that the V2 alloy has the largest modulus distribution, where the FWHM is 27.7%. The FWHM for the V4 and V6 alloys is 15.3% and 17.1% respectively. The increase in modulus distribution can be more clearly seen in histograms comparing the distributions for the deformed and undeformed regions separately, as shown in Figure 4.7.

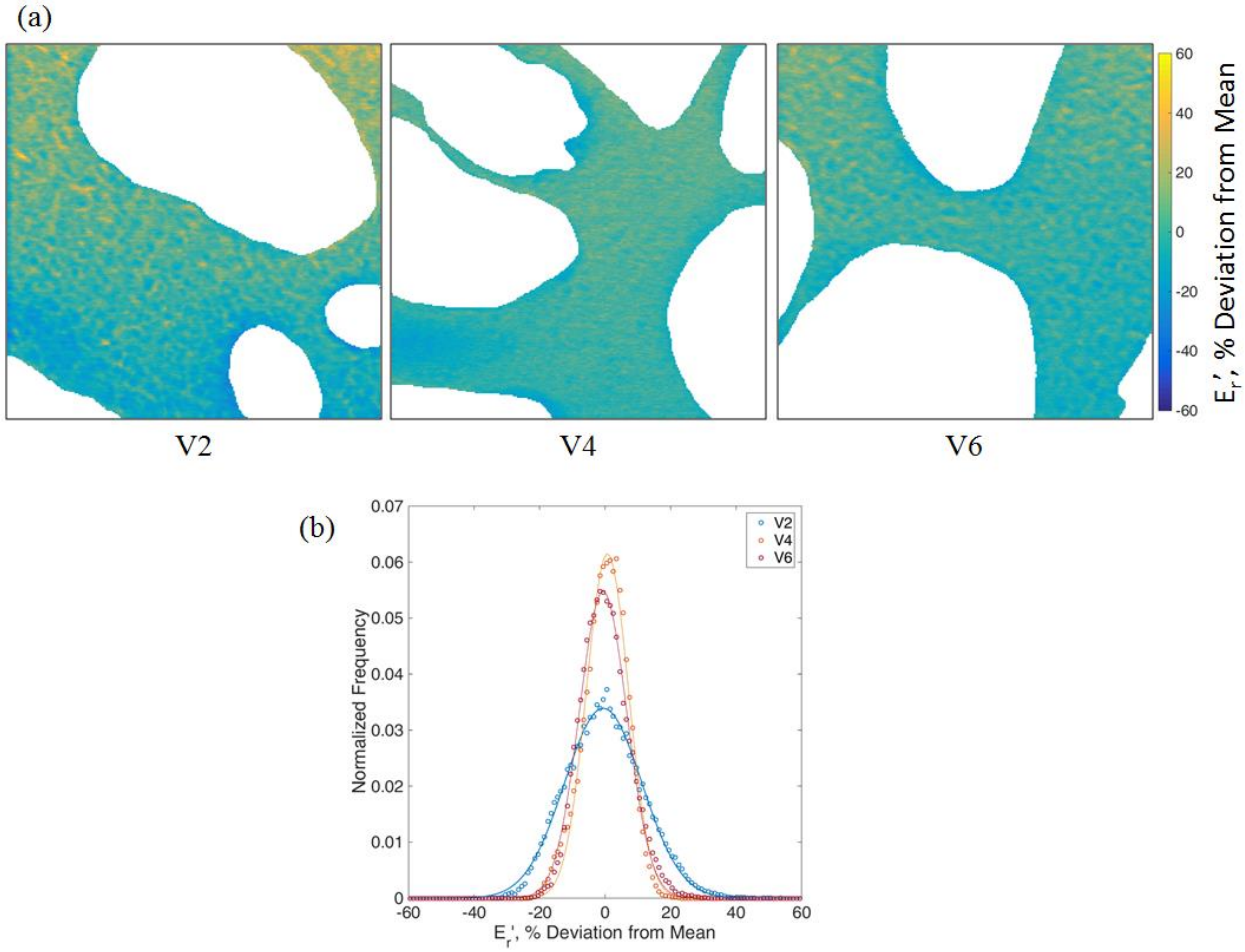

Figure 4.6. (a) Modulus maps of glass matrix phase of three of the V series composites, V2, V4, and V6, acquired from the deformed region near the fracture surface. Each map measures 5 x 5 μm. **(b)** Corresponding histogram of the modulus from each of the three maps.

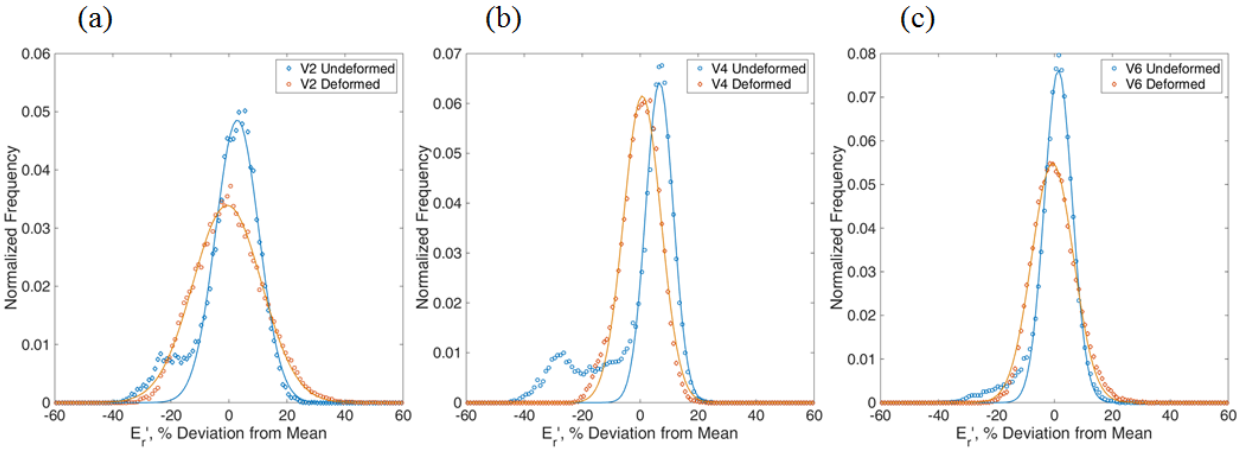

Figure 4.7. Histogram comparisons between the undeformed (blue) and deformed (orange) maps for **(a)** V2, **(b)** V4, and **(c)** V6.

4.4. Discussion

This alloy series exhibited a wide range of tensile mechanical behavior, despite incremental composition changes of only 2% vanadium. This work shows a significant correlation between composition and mechanical properties of Ti-based BMGCs, with the potential for tuning the composition to customize performance.

Having a higher dendrite than matrix modulus, as is the case in V0, has been shown to be a predictor of poor ductility [15]. This is based on the analysis of He and Hutchinson [18] in which the Dundur parameter ($\alpha = (E_{r,dendrite} - E_{r,matrix})/(E_{r,dendrite} + E_{r,matrix})$, when calculated with indentation moduli) is used to predict how a crack will propagate through a composite. For negative values of α, He and Hutchinson demonstrate that a crack (or similarly a shear band) propagating in the matrix would be attracted to the dendrite, while it would deflect away from the interface when α is positive [16,18]. Figure 4.8 shows a plot of plastic strain for a number of different alloys, including the alloys investigated here, with varying Dundur parameters. While the Dundur parameter is not an absolute predictor of ductility, there is a general trend of increasing plastic strain with decreasing Dundur parameter, particularly when $\alpha < -0.05$. With a more negative Dundur parameter, there is more of a driving force for a shear band or crack in the glass matrix to reenter a dendrite, which may promote the formation of longer flaws in the matrix and result in a less ductile composite. However, there are composites with negative α that exhibit zero ductility as well as one composite in the plot with a positive α and a small amount ductility. The two phase transformation composites shown in the plot have high ductilities, but their Dundur parameters are close to zero. This plot shows that merely having a softer dendrite is not a sufficient condition for ductility, although the magnitude of the negative α is an indicator of the ductility.

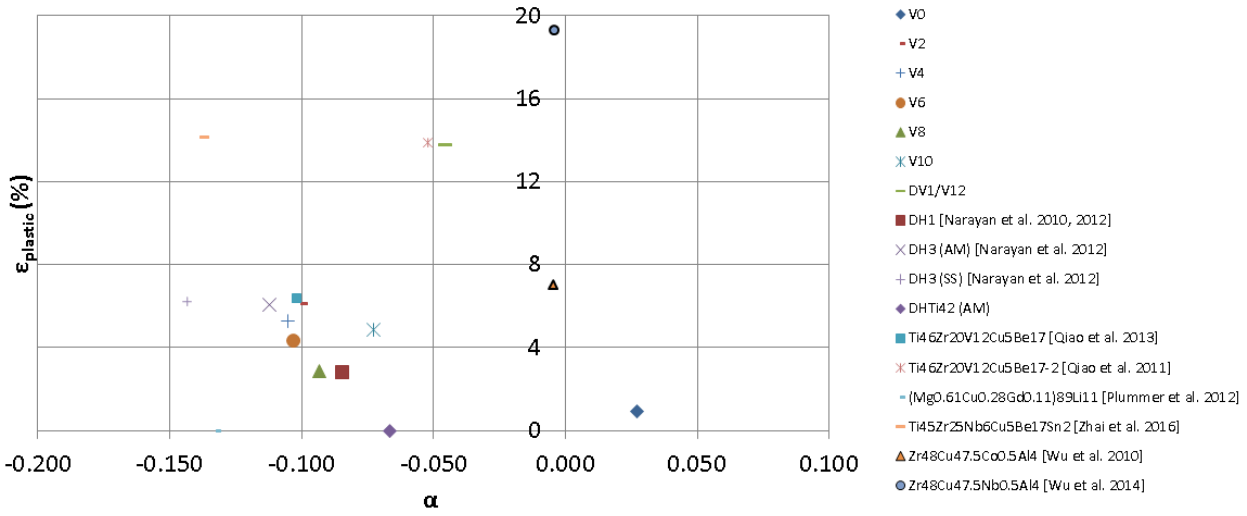

Figure 4.8. Plot of plastic strain for a variety of BMGCs with different Dundur parameters (α) [8,12,19–24]. The two data points outlined in black are phase transformation composites while the remaining data points are in situ composites.

The tensile test results showed that V0 exhibited negligible tensile ductility, which was expected based on the positive Dundur parameter. The difference in tensile behavior is most drastic between the V0 and V2 composite, where the plastic strain increases from 1% to 6% and is accompanied by strain hardening behavior. The relative differences in mechanical properties between the two phases in V0 versus V2 explain the changes in the bulk properties observed between these two alloys. While the indentation modulus of the matrix remained fairly consistent at ~110 GPa, the dendrite modulus decreased substantially from 118 GPa to 90 GPa. This satisfies the condition that the dendrite must be less stiff than the matrix in order to obtain ductility in the composite. However, the relative nanoindentation properties do not account for the variety of behaviors observed in the tension results of V2-V12. Neither the overall range of work hardening/softening behaviors nor the tensile ductility or strength trends shown in Figure 4.2 are reflected in the modulus or hardness trends, with the exception that all trends are reversed at the V6–V8 composition range, where the dendrite modulus, dendrite hardness, σ_{max}, $\varepsilon_{plastic}$, and degree of strain hardening all appear to exhibit a local minimum. In short, the tensile

behavior of the BMGC would not be able to be predicted from the change in Dundur parameter obtained through nanoindentation alone for V2 through V12.

The variation in properties can primarily be explained by the variation in deformation mechanisms observed in the dendrites. V2, which demonstrates strain hardening, shows dislocations and twinning in the dendrites. V12, which showed extensive ductility and strain softening, also exhibits twinning and dislocations in the TEM analysis of the dendrites. Conversely, V6 exhibited limited ductility and a large degree of strain softening, and only dislocation defects were observed in the TEM analysis.

The modulus maps of the three selected composites show that the heterogeneities in the matrix are most distinct and have the broadest spread in values in the V2 alloy. This increased level of heterogeneity over the other two mapped composites could contribute to the high strength and ductility of the V2 composite. As discussed in the previous chapter, heterogeneities might be playing a role in the nucleation and propagation pathways of shear bands. Conceivably, the enhanced heterogeneity in the V2 alloy is causing more prolific shear band initiation and more tortuous propagation pathways, combining with the dendrite deformation mechanisms to fortify an altogether more robust composite.

Interestingly, the modulus variability increased in each of the composites near the fracture surface of the composite tensile bar. This is the opposite of the effect of annealing, described in Chapter 3, which caused a narrowing in the modulus distribution most likely due to relaxation causing an increase in the atomic packing efficiency. Potentially some slight rejuvenation of the glass in response to being in such proximity to the fracture surface is resulting in increased free volume and thereby contributing to the increase in the distribution [25]. The glass phase of the V2 composite has the largest variation in modulus as well as a larger

increase in the variation with deformation compared to V4 and V6. The large modulus variation in the glass of the as cast V2 could be due to compositional differences in the glass between the three composites. The glass composition of V2 was measured to be $Ti_{33.6}Zr_{27.2}Cu_{8.7}V_{1.5}Be_{28.7}$ while that of V6 was $Ti_{32.1}Zr_{27.4}Cu_{8.8}V_{1.4}Be_{30.0}$ [17]. The larger increase in modulus variation with deformation in V2 could be an effect of the dendrite deformation mechanism. While the dendrite deformation mechanism in V4 is unconfirmed, V2 dendrites undergo twinning while V6 dendrites do not. Twinning in dendrites causes a volume change, resulting in increased stress on the surrounding matrix [26]. Twinning in the V2 dendrites could be causing a higher stress and more rejuvenation in the surrounding glass matrix, leading to a larger variation in modulus in the deformed state.

Bulk metallic glasses are themselves hierarchical heterogeneities, with one level of heterogeneity being between the compliant crystalline dendrites and the stiff metallic glass matrix and the second level being the distribution of hard and soft spots in the metallic glass matrix. Under an applied stress, deformation initiates in the more compliant crystalline phase and subsequent misfit strains between the two phases create stress concentrations at the interface that activate multiple shear bands [4,27,28]. While the effects of modulus mismatch on the mechanical behavior of a composite are generally understood, the effects of heterogeneity, even on monolithic glasses, are still being determined. Thus, heterogeneity in the glass phase should be further investigated to determine its contributions towards the overall mechanical behavior of the composite. Potentially tuning the heterogeneities in the glass matrix, as well as optimizing the morphology and properties of the composite through compositional changes, could together be the pathway towards designing BMGCs with desirable properties.

4.5. Conclusions

In this work, an alloy series was created by collaborators by systematically decreasing the β-stabilizing vanadium content. Changes of only 2% in the vanadium concentration resulted in drastic changes in the tensile behavior of the composite, as well as the deformation mechanisms in the dendrites. Nanoindentation was used to ascertain the properties of the glass and crystalline phases, and showed that some of the tensile behavior could be attributed to differences in the elastic properties of the two phases, although it could not explain the bulk scale behavior of the complete series. Modulus mapping was also performed on three of the alloys in the series that exhibited differing behavior and properties. The V2 alloy, which was the only one that displayed significant strain hardening as well as high strength and ductility, was also the composite that had the widest modulus distribution. As with the monolithic metallic glasses, the glass heterogeneity is an important factor in the deformation of the glass. Consideration of both the interphase heterogeneity between the glass and the crystal as well as the intraphase heterogeneity within the glass could together lead to the design of better BMGCs.

4.6. References

[1] F. Szuecs, C.P. Kim, W.L. Johnson, Mechanical Properties of Zr56.2Ti13.8Nb5.0Cu6.9Ni5.6Be12.5 Ductile Phase Reinforced Bulk Metallic Glass Composite, Acta Mater. 49 (2001) 1507–1513. http://cat.inist.fr/?aModele=afficheN&cpsidt=976526 (accessed November 14, 2014).

[2] H. Choi-Yim, R.D. Conner, F. Szuecs, W.L. Johnson, Processing, Microstructure and Properties of Ductile Metal Particulate Reinforced Zr57Nb5Al10Cu15.4Ni12.6 Bulk Metallic Glass Composites, Acta Mater. 50 (2002) 2737–2745. http://www.sciencedirect.com/science/article/pii/S0151910702800526 (accessed July 28, 2014).

[3] R.B. Dandliker, R.D. Conner, W.L. Johnson, Melt Infiltration Casting of Bulk Metallic-Glass Matrix Composites, J. Mater. Res. 13 (1998) 2896–2901. doi:10.1557/JMR.1998.0396.

[4] C.C. Hays, C.P. Kim, W.L. Johnson, Microstructure Controlled Shear Band Pattern

Formation and Enhanced Plasticity of Bulk Metallic Glasses Containing in situ Formed Ductile Phase Dendrite Dispersions, Phys. Rev. Lett. 84 (2000) 2901–2904. http://www.ncbi.nlm.nih.gov/pubmed/11018971.

[5] M.L. Lee, Y. Li, C.A. Schuh, Effect of a Controlled Volume Fraction of Dendritic Phases on Tensile and Compressive Ductility in La-based Metallic Glass Matrix Composites, Acta Mater. 52 (2004) 4121–4131. doi:10.1016/j.actamat.2004.05.025.

[6] D.C. Hofmann, J.Y. Suh, A. Wiest, G. Duan, M. Lind, M.D. Demetriou, W.L. Johnson, Designing Metallic Glass Matrix Composites with High Toughness and Tensile Ductility, Nature. 451 (2008) 1085–1089. doi:10.1038/nature06598.

[7] S.Y. Lee, C.P. Kim, J.D. Almer, U. Lienert, E. Ustundag, W.L. Johnson, Pseudo-binary Phase Diagram for Zr-based in situ β Phase Composites, J. Mater. Res. 22 (2007) 538–543. doi:10.1557/jmr.2007.0066.

[8] R.L. Narayan, P.S. Singh, D.C. Hofmann, N. Hutchinson, K.M. Flores, U. Ramamurty, On the microstructure–tensile property correlations in bulk metallic glass matrix composites with crystalline dendrites, Acta Mater. 60 (2012) 5089–5100. doi:10.1016/j.actamat.2012.06.032.

[9] J.W. Qiao, S. Wang, Y. Zhang, P.K. Liaw, G.L. Chen, Large plasticity and tensile necking of Zr-based bulk-metallic-glass-matrix composites synthesized by the Bridgman solidification, Appl. Phys. Lett. 94 (2009). doi:10.1063/1.3118587.

[10] M.E. Launey, D.C. Hofmann, J.Y. Suh, H. Kozachkov, W.L. Johnson, R.O. Ritchie, Fracture toughness and crack-resistance curve behavior in metallic glass-matrix composites, Appl. Phys. Lett. 94 (2009) 241910. doi:10.1063/1.3156026.

[11] J. Eckert, J. Das, S. Pauly, C. Duhamel, Mechanical Properties of Bulk Metallic Glasses and Composites, J. Mater. Res. 22 (2011) 285–301. doi:10.1557/jmr.2007.0050.

[12] J.W. Qiao, T. Zhang, F.Q. Yang, P.K. Liaw, S. Pauly, B.S. Xu, A Tensile Deformation Model for In-situ Dendrite/Metallic Glass Matrix Composites, Sci. Rep. 3 (2013) 2816. doi:10.1038/srep02816.

[13] K.M. Flores, D. Suh, R. Howell, P. Asoka-Kumar, P.A. Sterne, R.H. Dauskardt, Flow and fracture of bulk metallic glass alloys and their composites, Mater. Trans. 42 (2001) 619–622. doi:DOI 10.2320/matertrans.42.619.

[14] J.M. Park, J. Jayaraj, D.H. Kim, N. Mattern, G. Wang, J. Eckert, Tailoring of in situ Ti-based bulk glassy matrix composites with high mechanical performance, Intermetallics. 18 (2010) 1908–1911. doi:10.1016/j.intermet.2010.02.029.

[15] D.C. Hofmann, W.L. Johnson, Improving Ductility in Nanostructured Materials and Metallic Glasses: “Three Laws,” Mater. Sci. Forum. 633–634 (2010) 657–663. doi:10.4028/www.scientific.net/MSF.633-634.657.

[16] D.C. Hofmann, J.Y. Suh, A. Wiest, M. Lind, M.D. Demetriou, W.L. Johnson, Development of Tough, Low-density Titanium-based Bulk Metallic Glass Matrix

Composites with Tensile Ductility, Proc. Natl. Acad. Sci. U. S. A. 105 (2008) 20136–20140. doi:10.1073/pnas.0809000106.

[17] J.A. Kolodziejska, H. Kozachkov, K. Kranjc, A. Hunter, E. Marquis, W.L. Johnson, K.M. Flores, D.C. Hofmann, Towards an understanding of tensile deformation in Ti-based bulk metallic glass matrix composites with BCC dendrites, Sci. Rep. 6 (2016) 22563. doi:10.1038/srep22563.

[18] M.Y. He, J.W. Hutchinson, Crack Deflection at an Interface between Dissimilar Elastic Materials, Int. J. Solids Struct. 25 (1989) 1053–1067. http://www.sciencedirect.com/science/article/pii/0020768389900218 (accessed December 2, 2014).

[19] R.L. Narayan, K. Boopathy, I. Sen, D.C. Hofmann, U. Ramamurty, On the hardness and elastic modulus of bulk metallic glass matrix composites, Scr. Mater. 63 (2010) 768–771. http://www.sciencedirect.com/science/article/pii/S1359646210003957 (accessed July 23, 2013).

[20] J.W. Qiao, A.C. Sun, E.W. Huang, Y. Zhang, P.K. Liaw, C.P. Chuang, Tensile deformation micromechanisms for bulk metallic glass matrix composites: From work-hardening to softening, Acta Mater. 59 (2011) 4126–4137. doi:10.1016/j.actamat.2011.03.036.

[21] J.D. Plummer, I.A. Figueroa, I. Todd, Phase Stability, Microstructure and Mechanical Properties of Li Containing Mg-based Bulk Metallic Glass Composites, Mater. Sci. Eng. A. 546 (2012) 103–110. doi:10.1016/j.msea.2012.03.034.

[22] H. Zhai, H. Wang, F. Liu, A strategy for designing bulk metallic glass composites with excellent work-hardening and large tensile ductility, J. Alloys Compd. 685 (2016) 322–330. doi:10.1016/j.amjmed.2015.10.002.This.

[23] Y. Wu, Y. Xiao, G. Chen, C.T. Liu, Z. Lu, Bulk Metallic Glass Composites with Transformation-Mediated Work-Hardening and Ductility, Adv. Mater. 22 (2010) 2770–2773. doi:10.1002/adma.201000482.

[24] F.F. Wu, K.C. Chan, S.S. Jiang, S.H. Chen, G. Wang, Bulk Metallic Glass Composite with Good Tensile Ductility, High Strength and Large Elastic Strain Limit, Sci. Rep. 4 (2014) 5302. doi:10.1038/srep05302.

[25] D.J. Magagnosc, G. Kumar, J. Schroers, P. Felfer, J.M. Cairney, D.S. Gianola, Effect of ion irradiation on tensile ductility, strength and fictive temperature in metallic glass nanowires, Acta Mater. 74 (2014) 165–182. doi:10.1016/j.actamat.2014.04.002.

[26] S. Pauly, S. Gorantla, G. Wang, U. Kühn, J. Eckert, Transformation-mediated Ductility in CuZr-based Bulk Metallic Glasses, Nat. Mater. 9 (2010) 473–477. doi:10.1038/nmat2767.

[27] R.T. Ott, F. Sansoz, J.F. Molinari, J. Almer, K.T. Ramesh, T.C. Hufnagel, Micromechanics of Deformation of Metallic-glass–matrix Composites from in situ Synchrotron Strain Measurements and Finite Element Modeling, Acta Mater. 53 (2005)

1883–1893. doi:10.1016/j.actamat.2004.12.037.

[28] G. Chen, J.L. Cheng, C.T. Liu, Large-sized Zr-based Bulk-metallic-glass Composite with Enhanced Tensile Properties, Intermetallics. 28 (2012) 25–33. doi:10.1016/j.intermet.2012.03.054.

Chapter 5: Low Temperature Plastic Rheology of Olivine Determined by Nanoindentation

This chapter is largely adapted from the following publication: K. Kranjc, Z. Rouse, K.M. Flores, P. Skemer, Low temperature plastic rheology of olivine determined by nanoindentation, Geophys. Res. Lett. 43 (2016) 176–184. All data was collected by K. Kranjc. Data analysis was performed by both K. Kranjc and Z. Rouse. The Introduction and Background were written by P. Skemer.

5.1. Introduction

Convection in planetary mantles is accommodated mainly by the sub-solidus flow of minerals such as olivine, the most abundant mineral in the upper mantle [1]. Deformation may occur by one of several microscopic mechanisms, involving motion of dislocations, diffusive mass transfer, grain-boundary sliding, or some combination thereof (e.g. refs. [2–4]). At high temperatures and low convective stresses characteristic of the sub-lithospheric upper mantle olivine is expected to deform by dislocation creep or by dislocation accommodated grain boundary sliding [5,6]. Both mechanisms produce texture, which is detected through the observation of wide-spread seismic anisotropy in the upper mantle (e.g. ref. [7]). However, experiments show that at lower temperatures or higher stresses there is an additional contribution to deformation by power-law breakdown or "low temperature" plasticity [8], which may reflect a transition to obstacle-limited dislocation glide [2,9].

It is generally assumed that the effects of low temperature plasticity are minimal in deeper parts of the Earth when temperatures are high and convective stresses are low [10–12]. However, stresses may be larger within the ductile or semi-brittle regions in the lithosphere [13–15] or at the tips of cracks [16,17]. Moreover, large shear stresses are common in laboratory experiments and the effects of low temperature plasticity must be considered when extrapolating experimental data to geologic strain-rates [18,19]. Hence, precise measurements of rheology at

low temperatures are critical for interpreting geologic observations and reconciling these observations with experimental data.

In this study we present new data obtained using instrumented nanoindentation that further constrains the low-temperature rheology of olivine, while demonstrating the efficacy of this technique for the general study of mineral rheology. Although indentation methods have been used extensively in fields such as materials science, (e.g. ref. [20]), their application to geological sciences has been limited [21–27]. Nanoindentation provides a number of advantages over traditional high pressure and temperature rock deformation experiments. First, nanoindentation is a relatively precise technique, with sub-nanometer displacement resolution and force resolution as low as 100 nN [28]. Second, brittle deformation is readily suppressed due to the self-confined nature of the indentation method [29]. Hence, plasticity is easily achieved for hard materials at room temperature conditions without secondary confinement from a gaseous or solid medium. Finally, experiments are rapid and minimally destructive, so many tests can be performed in a short period of time.

5.2. Background

At low temperature conditions, obstacle-limited dislocation glide is expected to be the dominant deformation mechanism in many minerals [2,8]. While there are several formulations for constitutive relations in the exponential regime, we follow here the derivation from Frost and Ashby [2]. Orowan [30] provided the well-known equation for strain accumulation by dislocation motion:

$$\dot{\varepsilon} = \rho b \bar{v} \tag{5.1}$$

which states that strain-rate ($\dot{\varepsilon}$) is the product of dislocation density (ρ, itself a non-linear function of stress), the Burgers vector of the slip system b, and the average velocity of the dislocation, $\bar{v}$. A general formulation for the velocity of dislocations is:

$$\bar{v} \propto \exp\left(-\frac{H^*}{RT}\right) \tag{5.2}$$

where H^* is the activation enthalpy, R is the gas constant, and T is absolute temperature [2]. In the case of low temperature plasticity, H^* is stress dependent:

$$H^* = H_o^*\left(1 - \left(\frac{\sigma}{\sigma_c}\right)^p\right)^q \tag{5.3}$$

where H_0^* is the zero-stress activation enthalpy, σ is the differential stress, and σ_c is the critical stress where dislocations move freely through obstacles at T = 0 K (the "athermal flow strength" of Frost and Ashby [2]). Dimensionless constants p and q depend on the details of the energy barriers to dislocation motion and are constrained to fall within ranges $0 \leq p \leq 1$ and $1 \leq q \leq 2$ [9]. For the specific case where plasticity is rate-limited by the lattice friction, $\sigma_c = \sigma_p$, where σ_p is the Peierls stress (cf. ref. [4]).

Combining Equations (5.1-5.3), and noting that ρ is proportional to σ^2, yields a constitutive expression describing low temperature plasticity (cf. Equation 2.12, ref. [2]):

$$\dot{\varepsilon}_{LTP} = A\sigma^2 \exp\left\{-\left(\frac{H_o^*}{RT}\right)\left(1 - \left(\frac{\sigma}{\sigma_p}\right)^p\right)^q\right\} \tag{5.4}$$

where $\dot{\varepsilon}_{LTP}$ is the strain-rate of the material deforming by this mechanism, and A is a material-dependent parameter. As σ/σ_p approaches unity materials begin to yield plastically at a rate that is nearly independent of temperature.

Previous studies have attempted to constrain the low-temperature behavior of olivine through microindentation [21] and high pressure and temperature deformation experiments using either Griggs or the D-DIA apparatus [18,19,31]. Data are fit to an equation such as 5.4 assuming particular models for dislocation obstacles. Previous studies determined Peierls stresses for dry olivine that range from 5.9 GPa [19] to 15.4 GPa [31]; Katayama and Karato [18] conducted a study under water-saturated conditions in which they determined Peierls stresses of 1.6-2.9 GPa. Although rheological experiments at high temperature are relatively straightforward, experiments approaching room temperature are challenging due to the strength of olivine and its propensity to deform by brittle mechanisms when the applied differential stress is greater than the confining pressure [13,21]. Furthermore, precise stress measurements under high confining pressures are technically difficult, requiring either in situ measurements of changes to lattice spacing with a synchrotron light source (e.g. refs. [19,31]), which have significant uncertainty [32], or measurements based on calibrated relationships with dislocation density (e.g. ref. [18]).

5.3. Experimental Procedure

5.3.1. Materials

Two olivine samples were investigated in this study. The first sample was derived from a single crystal of San Carlos olivine, which was separated from a mantle xenolith. Optical microscopy confirmed the sample to be free of fluid inclusions, fractures, and subgrain boundaries. A second polycrystalline sample was synthesized from ground powders of the Balsam Gap Dunite, which was vacuum sintered at 1390°C for 4 hours at a pressure of 10 Pa (see ref. [33] for details of sample preparation). The polycrystalline olivine sample had a grain size of approximately 250 μm and no preferred crystallographic orientation. The single crystal of olivine was unoriented. Both samples are inferred to contain very low concentrations of water:

San Carlos olivine is considered to be nearly anhydrous [34], while the high-temperature preparation procedure for the polycrystalline sample should have effectively removed any pre-existing water. The samples were polished to a 0.1 μm finish using diamond paste and mounted on stainless steel discs. The single crystal olivine was attached to the disc using H20E EPO-TEK silver conductive epoxy suitable for testing at elevated temperatures. The polycrystalline sample was mounted to a separate disc using cyanoacrylate adhesive, which is appropriate for room temperature testing.

5.3.2. Nanoindentation

Nanoindentation measurements were obtained using the methods and equipment described in Section 2.3. The sample was clamped to the heating/cooling stage, the desired temperature was set, and the sample was left to equilibrate for at least 40 minutes before testing. The area function, which relates indent depth to projected area, of a diamond Berkovich probe was calibrated using a fused quartz standard. The single crystal olivine sample was tested in this manner at temperatures of 0, 75, 125, and 175°C, as well as at a room temperature of 23°C without activating the temperature control stage. At least 33 indents were made at each temperature setting; a total of 175 indents were made during this part of the study. Dry nitrogen gas was flowed over the sample for the 0°C tests to prevent condensation on the sample surface. For each indent, the sample was loaded at a rate of 1000 μN/s to a maximum load of 5000 μN with a 2 second hold at maximum load.

Additional constant strain rate indentation tests were performed at room temperature at an indentation strain rate of 0.05 s^{-1}. Nanoindentation strain rate ($\dot{\varepsilon}_i$) is calculated as the displacement rate ($\dot{h}$) of the nanoindentation probe divided by the instantaneous displacement (h) [35–38]. During these constant strain rate tests, the load is increased exponentially over a

calculated time interval to achieve the desired strain rate. A set of 16 indents performed in this manner were conducted to a maximum load of 5000 μN with a 2 second hold at maximum load and a linear unloading rate of 1000 μN/s. The nanoindentation strain rates for both the quasistatic temperature tests and the constant strain rate tests were converted to uniaxial strain rates ($\dot{\varepsilon}_u$) through $\dot{\varepsilon}_u = \dot{\varepsilon}_i/3$, which is based on relationships found in other material systems [35–39].

In order to study the effect of crystallographic orientation, tests were performed on 24 individual grains from the untextured polycrystalline olivine sample at room temperature. Approximately 9 indents were performed on each of the 24 individual grains at a rate of 28 nm/s to a maximum displacement of 140 nm. All indents were placed in the center of the grains to avoid any potential influence from grain boundaries.

5.3.3. Data Analysis

The resulting load-displacement curves from the nanoindentation testing were first analyzed using classical relations to obtain the reduced modulus from indentation (E_r) and the hardness (H),

$$E_r = \frac{S\sqrt{\pi}}{2\sqrt{A_c}} \tag{5.5}$$

$$H = \frac{P_{max}}{A_c} \tag{5.6}$$

where S is the slope of the load-displacement curve upon unloading, A_c is the projected contact area of the indentation, and P_{max} is the maximum indentation load. The reduced modulus was also converted into a compressive Young's modulus for an isotropic material via:

$$\frac{1}{E_r} = \frac{1-\nu^2}{E} + \frac{1-\nu_i^2}{E_i} \tag{5.7}$$

where ν and E are the Poisson ratio and modulus of the sample and ν_i and E_i are those of the indenter probe (ν_i = 0.07, E_i = 1140 GPa for the diamond indenter used here). The Poisson ratio of olivine was taken to be 0.247 for all temperatures [40].

Each curve was further analyzed according to the method of Mata and Alcala [41,42] in order to extract uniaxial mechanical properties. This method is based on finite element modeling for non-linear plastic deformation following the power law stress-strain relation:

$$\varepsilon = \left(\frac{\sigma_y}{E}\right)\left(\frac{\sigma}{\sigma_y}\right)^{1/n} \tag{5.8}$$

where σ_y is the yield strength at which plastic deformation commences, E is the Young's modulus, and n is the power law strain hardening exponent. The von Mises yield criterion was used for their simulations. To apply Mata and Alcala's method, first a quadratic function is fit through the loading portion of the load-displacement curve in order to determine the curvature (K). The curvature is used to calculate the pile-up factor (α), a dimensionless quantity describing the amount of material pile-up or sink-in around the boundary of the probe during indentation according to the relationship:

$$\alpha = \frac{K}{fH} \tag{5.9}$$

where f is a geometric factor equal to 24.56 for a Berkovich probe. Pile-up and sink-in increase or decrease the contact area, respectively, from what is expected from the indent depth. A value of $\alpha^{0.5} > 1$ indicates the development of pile-up while $\alpha^{0.5} < 1$ implies sink-in. E and H (from Equations 5.6 and 5.7) are then used to determine σ_r, the uniaxial stress at a total characteristic

strain of 0.1, from numerical fits to finite element data (Equation 5 in ref. [42]). Further numerical fits relate the values of σ_r, E, and $\alpha^{0.5}$ to the power law strain hardening coefficient n (Equation 7 in ref. [42]). Finally, E, σ_r, and n are used to calculate the yield strength of the indented material by rearranging Equation 5.8 and applying the condition that $\varepsilon = 0.1$ when $\sigma = \sigma_r$:

$$\sigma_y = [\sigma_r(0.1E)^{-n}]^{1/1-n} \tag{5.10}$$

Complete details of this method are described in [41,42].

Once the yield strength was obtained, the data were analyzed according to the flow law in Equation 5.4. Several combinations of p and q were chosen to correspond with those values used in other low temperature plasticity studies [18,19,21,31]. Due to the limited data set in this study, not all of the parameters in the flow law could be constrained through a nonlinear least-squares inversion. Therefore, a zero-stress activation enthalpy of 320 kJ/mol, as determined by Mei et al. [19], was used for the fitting process. The choice of activation enthalpy has only a minor effect on the calculated Peierls stress. This was also demonstrated by Katayama and Karato [18], who found less than 10% difference in the calculated Peierls stress between activation enthalpies of 518 and 300 kJ/mol.

5.4. Results

The experimental conditions and results from all of the temperature tests, the constant strain rate tests, and the average values from the polycrystalline olivine are given in Table 5.1 with standard error from repeated measurements reported. For all of the testing conditions, the calculated $\alpha^{0.5}$ was approximately 0.88, indicating a slight sinking-in of material around the indent perimeter. This can be seen in the scanning probe microscopy (SPM) image of an example

indent in Figure 5.1. The average strain hardening exponent n was calculated to be 0.22 on average for the single crystal olivine and 0.09 for the polycrystalline sample. The ratio E/σ_r, which describes the elastic and plastic contributions to the stress field under the indenter, was approximately 30 for all conditions. Figure 1, as well as all other SPM images acquired during testing, shows no evidence for crack formation at the sample surface. This indicates that all permanent deformation was accommodated by non-brittle phenomena. Figure 5.2 shows the load-displacement curves for the temperature tests as well as the indentation strain rate evolution over time for a quasi-static temperature test and a constant strain rate test. The strain rate was calculated from the final 20 nm of loading for each test. A uniaxial strain rate of approximately 0.04 s^{-1} was measured for each of the temperature tests. Because this strain rate cannot be considered steady state due to the nature of the quasistatic test, constant strain rate tests were performed to ensure that the properties obtained from the quasistatic tests are valid. The constant strain rate tests exhibit less variation in measured strain rate and are in good agreement with the quasistatic tests for all of the calculated properties.

Table 5.1. Summary of experimental conditions and results. Standard error from repeated measurements is reported.

Crystal Type	Temperature (°C)	Reduced Modulus (GPa)	Hardness (GPa)	Indentation Strain Rate, $\dot{\varepsilon}_i$ ($x10^{-1}$ s^{-1})	Uniaxial Strain Rate, $\dot{\varepsilon}_u$ ($x10^{-2}$ s^{-1})	Yield Strength (GPa)
Single	0	164.10 ± 7.40	14.12 ± 0.58	1.21	4.04	4.60 ± 0.27
Single	23	181.29 ± 6.47	14.32 ± 0.42	1.11	3.70	4.59 ± 0.24
Single	75	178.55 ± 5.22	14.91 ± 0.45	1.21	4.04	4.38 ± 0.22
Single	125	160.64 ± 9.37	13.12 ± 0.55	1.20	4.01	4.28 ± 0.28
Single	175	160.77 ± 9.01	13.12 ± 0.48	1.20	3.99	4.19 ± 0.32
Single*	23	184.27 ± 12.25	14.29 ± 0.74	0.538	1.79	4.51 ± 0.35
Poly	23	168.60 ± 11.53	14.42 ± 0.76	2.21	7.37	5.65 ± 0.39

*Constant strain rate

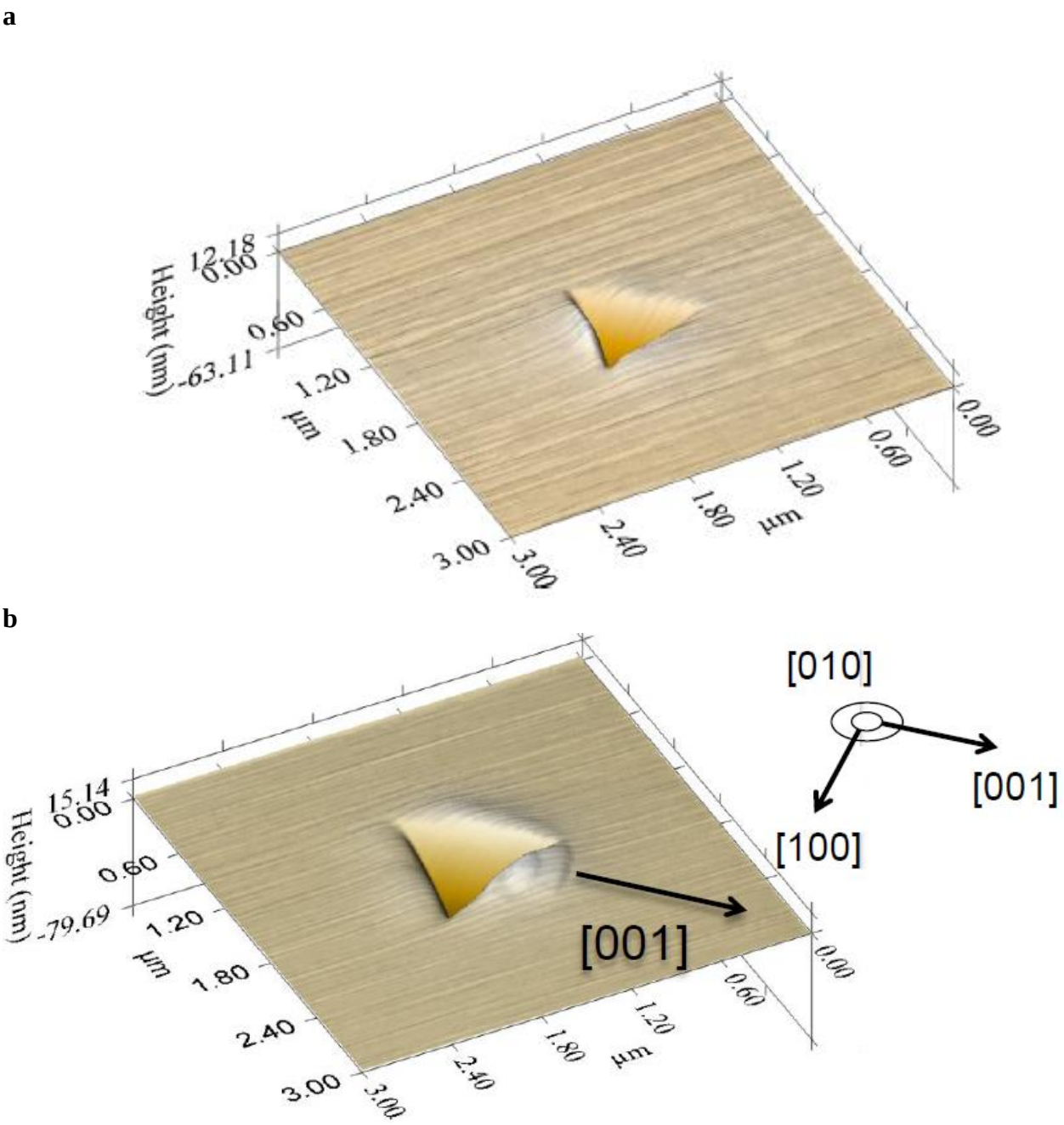

Figure 5.1. Scanning probe microscopy images of (a) a 5000 μN indent made at 75°C and (b) an 8833 μN indent made at 23°C. The orientation provided in (b) is not applicable to (a). The topographical image is obtained by rastering the nanoindentation probe across the surface while maintaining a constant load between the probe and the surface. The z axis describes the surface distortions relative to the height of the original surface, which is set to 0 nm. The lack of any visible cracking on the surface indicates that all permanent deformation was accommodated plastically. Pile-up occurs in the [001] crystallographic direction.

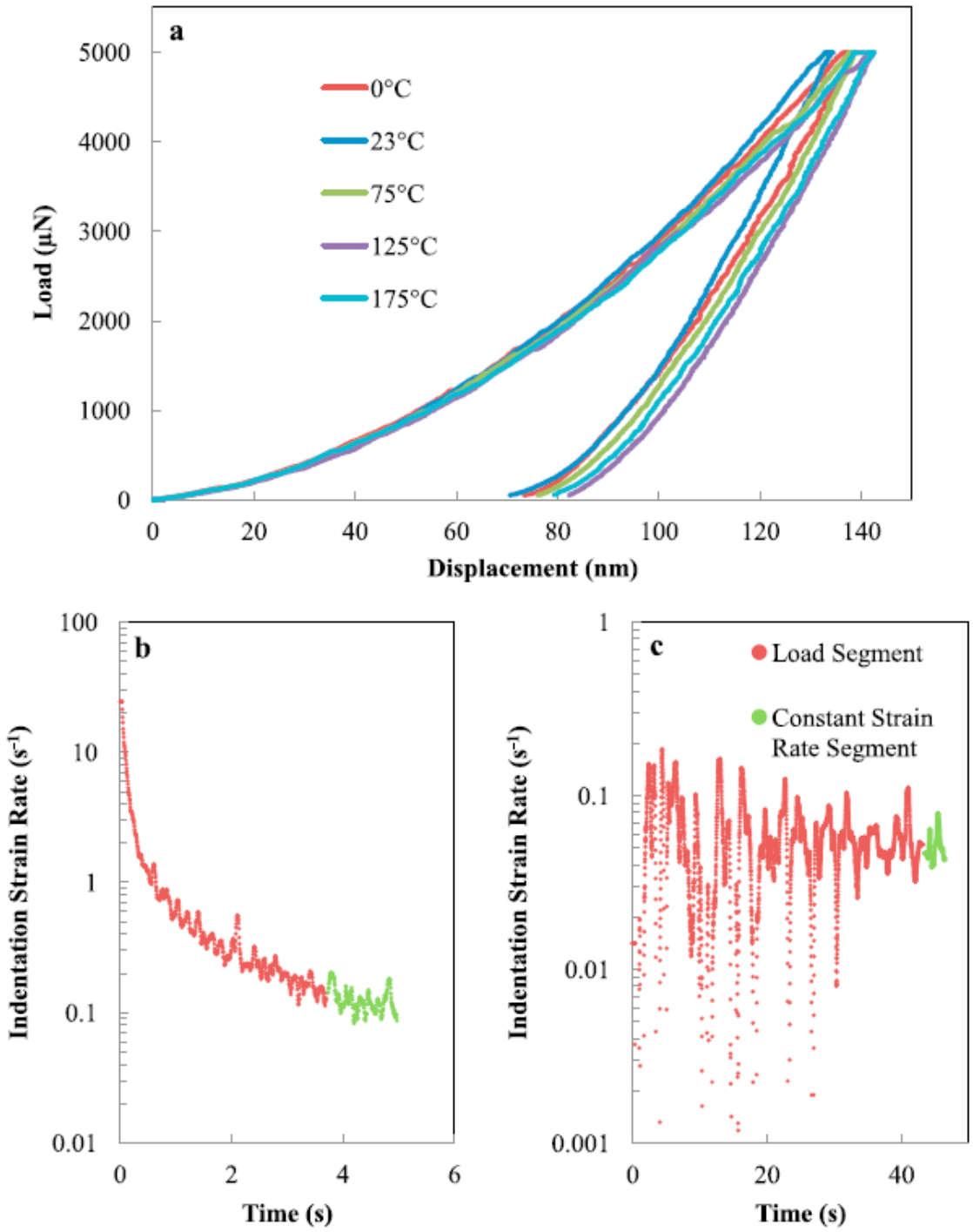

Figure 5.2. (a) Example of load-displacement curves from the different temperature tests. Indentation strain rate-time curves obtained at (b) 75°C for quasi-static and (c) 23°C for constant strain rate. For (b) and (c), the average strain rate over the final 20 nm of loading (constant strain rate segment; green) was used in the analysis. Each of these plots used an averaging window of 1.5% of the duration of the test. The scatter is due to fluctuations in displacement during the load-controlled testing.

Figure 5.3 shows the data obtained in this study fitted to flow laws of the form given in Equation 5.4 with (p, q) combinations of (1/2, 1), (1, 2), (2/3, 2), (3/4, 4/3), and (1, 1). The first four combinations were chosen for their use by Mei et al. [19], Raterron et al. [31], Evans and Goetze [21], and Frost and Ashby [2], respectively. The (1, 1) combination was also evaluated because it defined a lower bound for the Peierls stress (cf. ref. [18]). Also plotted in Figure 3 are the flow laws of Evans and Goetze [21], Raterron et al. [31], and Mei et al. [19] adjusted to a strain rate of 0.04 s^{-1}. The fitting procedure produced ~1 GPa spread in the Peierls stress, ranging from 5.32 GPa (p=1, q=1) to 6.45 GPa (p=2/3, q=2). The average room temperature yield strength measured from the polycrystalline olivine was 5.65 GPa with a standard deviation of 0.39 GPa from the orientation effects.

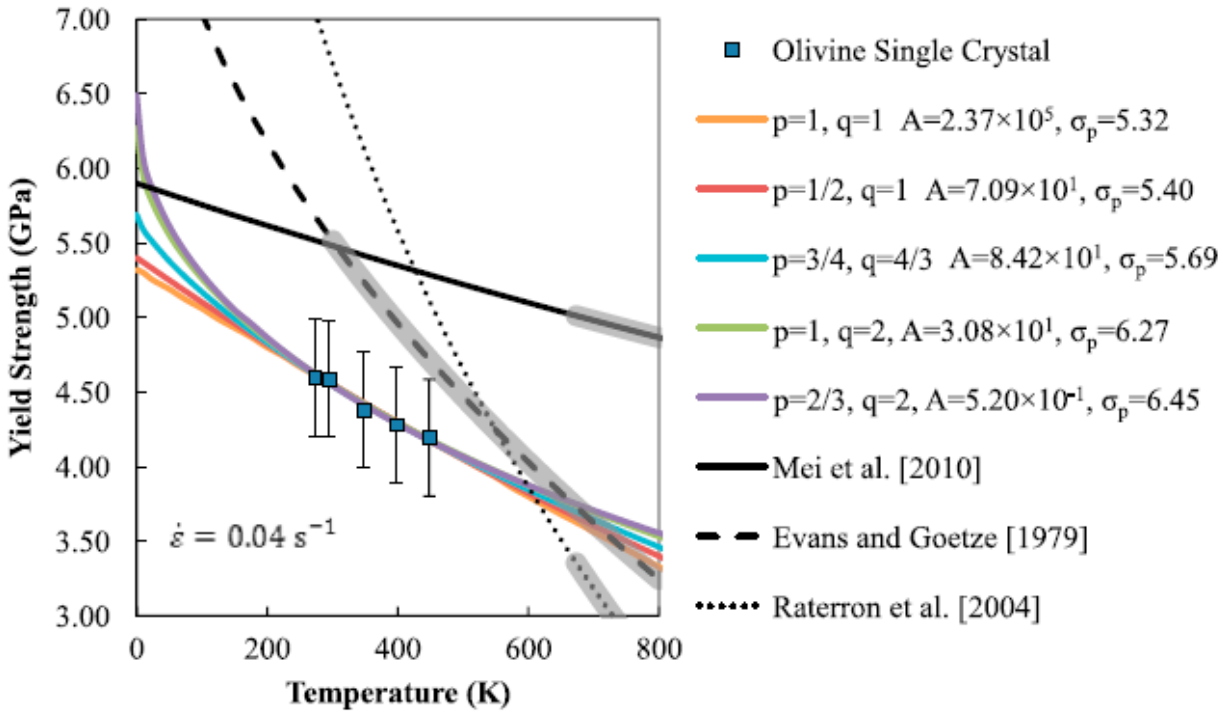

Figure 5.3. Yield strength plotted against temperature for the single crystal olivine tests (blue squares; $\dot{\boldsymbol{\varepsilon}}$ = 0.04 s^{-1}). Each curve was plotted using $\boldsymbol{H_0^*}$ = 320 kJ/mol. A and σ_p given for each curve have units of s-1GPa-2 and GPa, respectively. The error bars on the single crystal data points reflect the potential orientation effect, which is estimated as one sigma uncertaintly from the distribution of measurements on the polycrystalline sample. The single crystal olivine data were fit to Equation (5.4 using several combinations of p and q values. For comparison, the flow

laws of Evans and Goetze [21], Raterron et al. [31], and Mei et al. [19] at $\dot{\varepsilon} = 0.04\ s^{-1}$ are also included. The shaded gray regions on these flow laws indicate the range where experimental data were collected for each respective study.

5.5. Discussion

Figure 5.3 shows that the Peierls stresses determined by this study, 5.32 – 6.45 GPa, are among the lowest for any comparable study on dry olivine. These values are well below those determined by Evans and Goetze [21] and Raterron et al. [31], however they are in good agreement with the results of Mei et al. [19] who obtained a Peierls stress of 5.9 GPa.

Because indentation tests require the activation of many independent slip systems, it is likely that the orientation of the single crystal sample had some systematic effect on the measured properties in our study. While the orientations of the samples used in this study were not determined, the indentation arrays performed in the untextured polycrystalline olivine showed that the variation in yield strength between the grains was only ~7%. Similarly, Evans and Goetze [21] reported less than 10% variation in properties measured by indentation due to orientation effects. Because the testing volume of nanoindentation is well below the size of the individual olivine grains, this technique can only provide measurements of the individual grains (as if they were individual single crystals) not of the aggregate polycrystalline sample. Thus, performing the nanoindentation on a polycrystalline sample does not provide comprehensive properties for the sample as a whole. Conversely, the experiments by Mei et al. [19] and Raterron et al. [31] determined the average properties of an entire polycrystalline sample, which has the benefit of averaging any effects of crystallographic orientation. There is, however, a possibility that grain boundaries influenced the mechanical properties through the activation of additional deformation mechanisms.

In comparison to the high temperature and pressure methods typically used to measure rheological properties of geologic materials, nanoindentation provides a relatively simple and precise method to quantify rheology in low temperature deformation regimes. However, two particular aspects of nanoindentation testing that pertain to this study should be reviewed: thermal effects and conversion between indentation and uniaxial properties.

Thermal drift, the expansion or contraction between the sample and the indenter tip, is a concern at room temperature, and even more so with the use of a heating or cooling stage. This drift can adversely affect the accurate measurement of the probe displacement into the sample, resulting in incorrect property measurements. While this study attempted to mitigate the effects of drift by waiting a sufficient amount of time for the sample and probe to reach thermal equilibrium, large drift rates on the order of 0.8 nm/s were observed for the 175°C testing. However, the instrument software corrects the displacement measurements to account for the measured thermal drift. Additionally, a study on thermal drift in nanoindentation reports that its effects are negligible on the computed nanoindentation modulus if the time from the beginning of the test to the start of unloading is less than $(S \cdot h_c)/\dot{P}$, where h_c is the contact depth and $\dot{P}$ is the unloading rate [43]. At all of the temperatures tested in the current study, the test time was less than this quantity. The short test duration and automatic correction routine suggest that the effects from thermal drift on the data collected here are minimal.

The conversion of indentation measurements to uniaxial properties is not a trivial procedure. There is a very small body of literature, primarily tailored toward metals, that explores the relationship between indentation and uniaxial properties, and there is no universally applicable method to convert between the two. The uniaxial strain rate was calculated here as one third of the indentation strain rate, similar to a study by Cordova and Shen on Sn and a

SnAgCu alloy, while other studies have found the conversion factor to be on the order of 0.1 [36].

The method of calculating yield strength [42] also comes with some uncertainties. This method was designed for metals with any combination of yield strength in the range of 50 – 1000 MPa, Young's modulus in the range of 70 – 200 GPa, and strain hardening exponent between 0 – 0.4. While the properties of olivine should fall within the acceptable ranges for strain hardening exponent and Young's modulus, the yield strength falls above the intended range. The analysis depends on defining the contact under the indenter as either fully plastic or in an elasto-plastic transition. The conditions for fully plastic deformation are met when the plastic zone under the indenter is unconstrained and spreads outward from the material's free surface. This tends to be satisfied when the ratio E/σ_r is greater than 100. Applying our data to this analysis method shows that E/σ_r is around 30, meaning that the olivine indentation lies well within the elasto-plastic transition regime. The model covers E/σ_r ratios between 20 and 3000 and is applicable regardless of the deformation regime, but the calculations within the elasto-plastic regime are much more sensitive to the pile-up factor $\alpha^{0.5}$. Slight variations in this factor can greatly affect the calculated strain hardening coefficient, and, by consequence, the yield strength. However, the calculation of the pile-up factor obtained from Equation 5.9 was verified for randomly selected indents by measuring the deformation from their SPM profiles, with less than 1% difference between the values calculated through Equation 5.9 and measured from the SPM profile. This lends confidence to the applicability of the Mata and Alcala method to the data collected here.

5.6. Conclusions

Experimental determinations of mineral rheology are central to our understanding of the dynamics of Earth's interior. Here, we provide data obtained using instrumented nanoindentation

that constrains the rheology of olivine under conditions that favor low-temperature plasticity. These data provide increased confidence in the extrapolation of previous laboratory data to low temperatures and contribute to our basic understanding of olivine rheology at conditions relevant to the shallow lithosphere. We have demonstrated that the nanoindentation technique provides valuable data that complement traditional high pressure and high temperature rock mechanics experiments but also presents a number of advantages and opportunities for future research. In particular, the high precision of the stress measurements and the ability to generate large datasets means that uncertainties in flow law parameters can be reduced significantly. Nanoindentation offers tremendous potential for micromechanical testing in parameter space previously unexplored for geologic materials.

5.7. References

[1] S.I. Karato, P. Wu, Rheology of the Upper Mantle: A Synthesis, Science (80-.). 260 (1993) 771–778. doi:10.1126/science.260.5109.771.

[2] H.J. Frost, M.F. Ashby, Deformation Mechanism Maps, Pergamon Press, New York, 1982.

[3] J.P. Poirier, Creep of Crystals, Cambridge University Press, New York, 1985.

[4] S.I. Karato, Deformation of Earth Materials, Cambridge University Press, New York, 2008.

[5] G. Hirth, D.L. Kohlstedt, Rheology of the Upper Mantle and the Mantle Wedge: A View from the Experimentalists, in: J. Eiler (Ed.), Insid. Subduction Fact., Geophysica, American Geophysical Union, Washington, DC, 2003: pp. 83–105.

[6] L.N. Hansen, M.E. Zimmerman, D.L. Kohlstedt, Grain boundary sliding in San Carlos olivine: Flow law parameters and crystallographic-preferred orientation, J. Geophys. Res. 116 (2011). doi:10.1029/2011JB008220.

[7] M. Panning, B. Romanowicz, A Three-dimensional Radially Anisotropic Model of Shear Velocity in the Whole Mantle, Geophys. J. Int. 167 (2006) 361–379. doi:10.1111/j.1365-246X.2006.03100.x.

[8] M.C. Tsenn, N.L. Carter, Upper Limits of Power Law Creep of Rocks, Tectonophysics. 136 (1987) 1–26. doi:10.1016/0040-1951(87)90332-5.

[9] U.F.F. Kocks, A.S.S. Argon, M.F.F. Ashby, Thermodynamics and Kinetics of Slip, Pergamon Press, Oxford, 1975. doi:10.1016/0079-6425(75)90005-5.

[10] V.S. Solomatov, L.N. Moresi, Scaling of Time-dependent Stagnant Lid Convection: Application to Small-scale Convection on Earth and Other Terrestrial Planets, J. Geophys. Res. 105 (2000) 21795–21817.

[11] V.S. Solomatov, R. El-Khozondar, V. Tikare, Grain Size in the Lower Mantle: Constraints from Numerical Modeling of Grain Growth in Two-phase Systems, Phys. Earth Planet. Inter. 129 (2002) 265–282. doi:10.1016/S0031-9201(01)00295-3.

[12] T. Wong, V.S. Solomatov, Towards scaling laws for subduction initiation on terrestrial planets: constraints from two-dimensional steady-state convection simulations, Prog. Earth Planet. Sci. 2 (2015) 18. doi:10.1186/s40645-015-0041-x.

[13] D.L. Kohlstedt, B. Evans, S.J. Mackwell, Strength of the Lithosphere: Constraints Imposed by Laboratory Experiments, J. Geophys. Res. 100 (1995) 17587–17602. doi:10.1016/S0016-0032(16)90156-X.

[14] W.M. Behr, G. Hirth, Rheological Properties of the Mantle Lid beneath the Mojave Region in Southern California, Earth Planet. Sci. Lett. 393 (2014) 60–72. doi:10.1016/j.epsl.2014.02.039.

[15] P. Skemer, S.I. Karato, Sheared Lherzolite Xenoliths Revisited, J. Geophys. Res. 113 (2008). doi:10.1029/2007JB005286.

[16] A.S. Argon, Brittle to Ductile Transition in Cleavage Fracture, Acta Metall. 35 (1987) 185–196. doi:10.1016/0001-6160(87)90228-8.

[17] J.R. Rice, R. Thomson, Ductile versus brittle behaviour of crystals, Philos. Mag. 29 (1974) 73–97. doi:10.1080/14786437408213555.

[18] I. Katayama, S.I. Karato, Low-temperature, high-stress deformation of olivine under water-saturated conditions, Phys. Earth Planet. Inter. 168 (2008) 125–133. doi:10.1016/j.pepi.2008.05.019.

[19] S. Mei, A.M. Suzuki, D.L. Kohlstedt, N.A. Dixon, W.B. Durham, Experimental Constraints on the Strength of the Lithospheric Mantle, J. Geophys. Res. 115 (2010). doi:10.1029/2009JB006873.

[20] W.C. Oliver, G.M. Pharr, Nanoindentation in materials research: Past, present, and future, MRS Bull. 35 (2010) 897–907. doi:10.1557/mrs2010.717.

[21] B. Evans, C. Goetze, The temperature variation of hardness of olivine and its implication for polycrystalline yield stress, J. Geophys. Res. 84 (1979) 5505–5524. doi:10.1029/JB084iB10p05505.

[22] M.E. Broz, R.F. Cook, D.L. Whitney, Microhardness, toughness, and modulus of Mohs scale minerals, Am. Mineral. 91 (2006) 135–142. doi:10.2138/am.2006.1844.

[23] D.L. Whitney, M. Broz, R.F. Cook, Hardness, toughness, and modulus of some common metamorphic minerals, Am. Mineral. 92 (2007) 281–288. doi:10.2138/am.2007.2212.

[24] W. Zhu, J.J. Hughes, N. Bicanic, C.J. Pearce, Nanoindentation Mapping of Mechanical Properties of Cement Paste and Natural Rocks, Mater. Charact. 58 (2007) 1189–1198. doi:10.1016/j.matchar.2007.05.018.

[25] D.L. Goldsby, A. Rar, G.M. Pharr, T.E. Tullis, Nanoindentation creep of quartz, with implications for rate- and state-variable friction laws relevant to earthquake mechanics, J. Mater. Res. 19 (2004) 357–365. doi:10.1557/jmr.2004.19.1.357.

[26] A. Bandini, P. Berry, E. Bemporad, M. Sebastiani, Effects of intra-crystalline microcracks on the mechanical behavior of a marble under indentation, Int. J. Rock Mech. Min. Sci. 54 (2012) 47–55. doi:10.1016/j.ijrmms.2012.05.024.

[27] P. Barnes, D. Tabor, J.C.F. Walker, The Friction and Creep of Polycrystalline Ice, Proc. R. Soc. London A Math. Phys. Eng. Sci. 324 (1971) 127–155. doi:10.1098/rspa.1971.0132.

[28] A.C. Fischer-Cripps, Nanoindentation, Third Ed, Springer Science+Business Media, LLC, New York, 2011.

[29] D. Tabor, The Hardness of Solids, Rev. Phys. Technol. 1 (1970) 145–179. doi:10.1088/0034-6683/1/3/I01.

[30] E. Orowan, Problems of Plastic Gliding, Proc. Phys. Soc. 52 (1940) 8–22. doi:10.1088/0959-5309/52/1/303.

[31] P. Raterron, Y. Wu, D.J. Weidner, J. Chen, Low-temperature Olivine Rheology at High Pressure, Phys. Earth Planet. Inter. 145 (2004) 149–159. doi:10.1016/j.pepi.2004.03.007.

[32] P.C. Burnley, D. Zhang, Interpreting in situ X-Ray Diffraction Data From High Pressure Deformation Experiments Using Elastic–Plastic Self-Consistent Models: An Example Using Quartz, J. Phys. Condens. Matter. 20 (2008) 285201. doi:10.1088/0953-8984/20/28/285201.

[33] M. Sundberg, R.F. Cooper, A Composite Viscoelastic Model for Incorporating Grain Boundary Sliding and Transient Diffusion Creep; Correlating Creep and Attenuation Responses for Materials with a Fine Grain Size, Philos. Mag. 90 (2010) 2817–2840. doi:10.1080/14786431003746656.

[34] Z.X.A. Li, C.T.A. Lee, A.H. Peslier, A. Lenardic, S.J. Mackwell, Water Contents in Mantle Xenoliths from the Colorado Plateau and Vicinity: Implications for the Mantle Rheology and Hydration-induced Thinning of Continental Lithosphere, J. Geophys. Res. 113 (2008) B09210. doi:10.1029/2007JB005540.

[35] M.E. Cordova, Y.L. Shen, Indentation Versus Uniaxial Power-law Creep: A Numerical Assessment, J. Mater. Sci. 50 (2014) 1394–1400. doi:10.1007/s10853-014-8699-9.

[36] C.L. Wang, Y.H. Lai, J.C. Huang, T.G. Nieh, Creep of nanocrystalline nickel: A direct

comparison between uniaxial and nanoindentation creep, Scr. Mater. 62 (2010) 175–178. doi:10.1016/j.scriptamat.2009.10.021.

[37] B.N. Lucas, W.C. Oliver, Indentation Power-Law Creep of High-Purity Indium, Metall. Mater. Trans. A. 30A (1999) 601–610.

[38] M.J. Mayo, W.D. Nix, A Micro-indentation Study of Superplasticity in Pb, Sn, and Sn-38 wt% Pb, Acta Metall. 36 (1988) 2183–2192. doi:10.1016/0001-6160(88)90319-7.

[39] W.H. Poisl, W.C. Oliver, B.D. Fabes, The relationship between indentation and uniaxial creep in amorphous selenium, J. Mater. Res. 10 (1995) 2024–2032. doi:10.1557/JMR.1995.2024.

[40] N.I. Christensen, Poisson's Ratio and Crustal Seismology, J. Geophys. Res. 101 (1996) 3139–3156. doi:10.1029/95JB03446.

[41] M. Mata, M. Anglada, J. Alcalá, Contact Deformation Regimes Around Sharp Indentations and the Concept of the Characteristic Strain, J. Mater. Res. 17 (2002) 964–976. doi:10.1557/JMR.2002.0144.

[42] M. Mata, J. Alcalá, Mechanical property evaluation through sharp indentations in elastoplastic and fully plastic contact regimes, J. Mater. Res. 18 (2003) 1705–1709. doi:10.1557/JMR.2003.0234.

[43] G. Feng, A.H.W. Ngan, Effects of Creep and Thermal Drift on Modulus Measurement Using Depth-sensing Indentation, J. Mater. Res. 17 (2002) 660–668. doi:10.1557/JMR.2002.0094.

Chapter 6: Low Temperature Plastic Rheology of Olivine Determined by Micropillar Compression

6.1. Introduction

This chapter presents experimental results of micrometer-scale compression testing of olivine. As stated in Chapter 5, achieving plastic flow in olivine in the laboratory becomes more difficult with lower temperatures due to the propensity of the material to fail in a brittle manner when the differential stress exceeds the confining pressure [1,2]. Typically in geological studies, a confining pressure from a solid or gaseous medium is often used to suppress cracking during mechanical testing. However, as the testing temperature decreases, higher confining pressures must be used to attain plasticity. In silicon, for example, confining pressures as high as 5 GPa are required to obtain plasticity at room temperature [3]. In olivine, a confining pressure of 9.45 GPa is needed for obtaining plasticity at 400°C [4]. These kinds of pressures are achievable only with highly specialized equipment [5].

Micromechanical testing is a much more suitable technique to enable the study of low temperature plasticity. Because this technique utilizes small volumes of material and can be conducted at temperatures well below the solidus of the material, the influence on deformation from mechanisms other than low temperature plasticity, e.g. grain boundary sliding and thermally-activated deformation mechanisms, can be suppressed. This will in turn allow for a more accurate determination of the low temperature plasticity flow law.

Micromechanical testing is typically conducted either through indentation studies or micropillar compression. While indentation studies are useful because a large number of tests can be completed quickly with very little material, it is difficult to obtain uniaxial properties due to the complicated stress state under the indenter [6]. Conversely, micropillar compression

provides uniaxial properties, but is a much more time-consuming technique. Conversion between the two properties is not straightforward, and can be material-dependent [7,8]. Using micropillar compression to establish a conversion to indentation properties in olivine would provide confidence in indentation measurements and allow for this more efficient technique to be used in future studies. The use of nanoindentation to induce low temperature plasticity was investigated in the last chapter, and this chapter focuses on the second method, micropillar compression.

6.2. Experimental Procedure

6.2.1. Sample Preparation and Testing

A sample of natural olivine was polished to a 0.5 μm diamond slurry finish. Nondestructive 3D X-ray microscopy using a Zeiss Xradia Versa 520 instrument was performed on a secondary olivine sample to determine if any irregularities were present in the sample that could be included in the pillars and cause early failure during mechanical testing. The technique found fluid pockets on the order of 20 μm in diameter, sometimes with dense inclusions. The fluid inclusions were spaced hundreds of micrometers apart and it was determined to be unlikely that they would affect any pillar fabrication or subsequent testing.

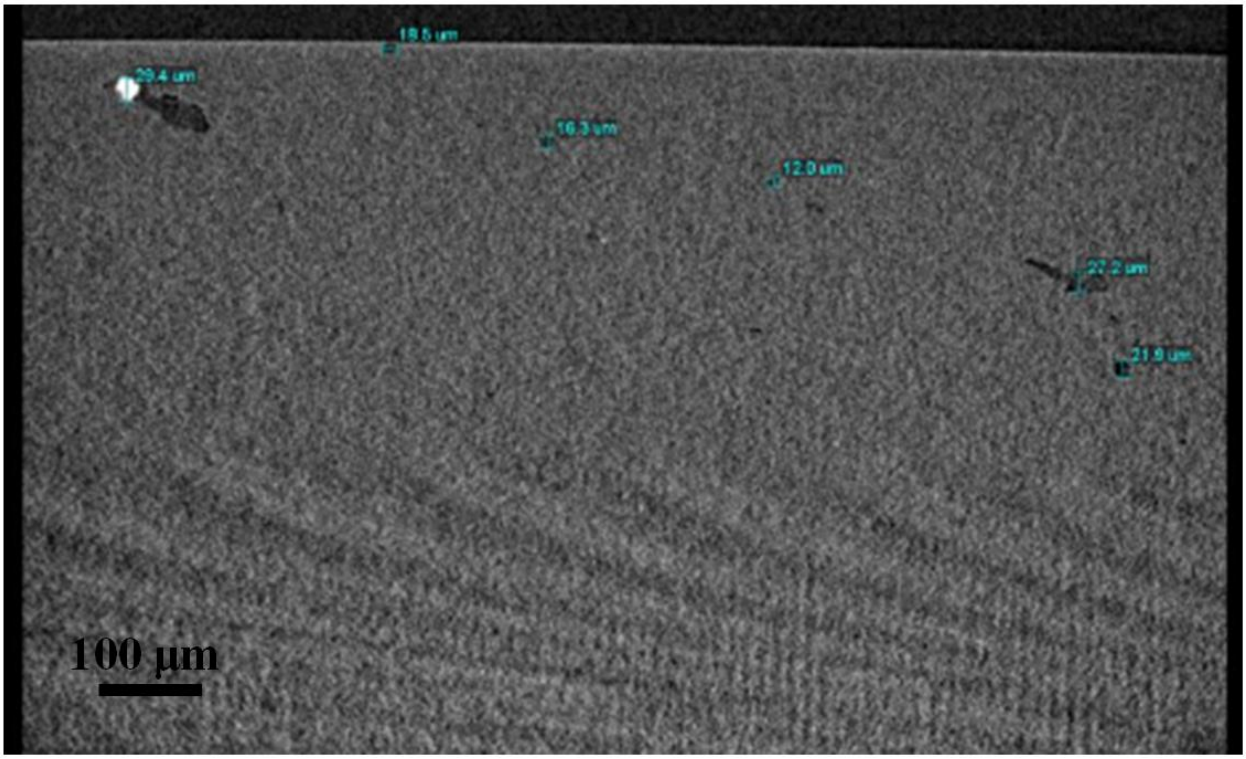

Figure 6.1. X-ray microscopy image of the interior of the olivine sample showing some areas of fluid inclusions, typically measuring 20 µm in diameter.

Micropillars measuring 1.25 µm in diameter with an aspect ratio of 1.75 were fabricated using a Zeiss Crossbeam 540 FIB-SEM. An annular milling technique commonly used for micropillar fabrication was employed here [9]. The exact milling parameters were given in Section 2.5.

The micropillar compression testing was performed using a Hysitron TI 950 instrument equipped with a flat punch probe at room temperature. Initial monotonic tests were performed to determine a pillar failure load. Subsequently, constant load testing was performed at loads slightly less than the pillar failure load for durations of 4 hours. During the hold segment of these tests, a 200 Hz sinusoidal load was superimposed over the set load using the nanoDMA III module on the instrument in order to continuously monitor the pillar stiffness. The amplitude of this sinusoidal load was selected so as to result in approximately 1 nm of dynamic displacement.

Transmission electron microscopy was performed on selected pillars. TEM samples were fabricated from the pillars using an FEI Quanta FIB with a gallium ion beam. The TEM analysis was performed using a JEOL JEM-2100F instrument at 200 kV.

6.2.2. Data Analysis

Pillar dimensions were determined before and after compression testing from high resolution SEM images using *ImageJ* software. The taper of the pillars was found to be 2° - 3°.

When converting the load-displacement curve into a stress-strain relationship, engineering stresses and strains are calculated because the pillar dimensions are unable to be monitored during testing. The stresses are calculated based on the cross-sectional area of the top of the pillar before testing, because this is where the diameter is smallest and thus the stress is highest. Strain calculations are based on the height of the pillar as measured in the SEM before testing.

Because of thermal drift occurring over the duration of the test, the displacement measurement from the instrument is not accurate over the creep segment of the test. The load oscillation was applied during this segment to continuously monitor the storage stiffness (k') of the pillar:

$$k' = \frac{F_D \cos\varphi}{d_D} + m_T\omega^2 - k_T \tag{6.1}$$

where F_D is the dynamic actuation force, φ is the phase shift between the dynamic force and dynamic displacement (d_D), m_T is the transducer mass, k_T is the transducer stiffness, and ω is the oscillation frequency. Once the storage stiffness was determined at discrete intervals throughout the creep segment, the displacement could be calculated from combining Equations 6.2a and 6.2b to get the pillar displacement in Equation 6.2c:

$$k' \approx \frac{F_D}{d_D} = \frac{\sigma A}{d_D} \tag{6.2a}$$

$$d_D = l\varepsilon = \frac{lF}{AE} \tag{6.2b}$$

$$d = h_0 - l = h_0 - \sqrt{\frac{VE}{k'}} \tag{6.2c}$$

where d is the displacement, h_0 is the initial height of the pillar, V is the pillar volume, and E is the elastic modulus. The pillar volume, which was assumed to remain constant throughout the test, was calculated as a conical frustum:

$$V = \pi \left[\frac{(h_0 \tan\beta + r_0)^3 - r_0^3}{3 \tan\beta} \right] \tag{6.3}$$

where β is the taper angle and r_0 is the radius of the top of the pillar.

When calculating the elastic modulus of pillar, both the fact that the pillar is affixed to a base material and that there is taper in the pillar must be accounted for with corrections. In regards to the former, when the pillar is being compressed, it causes some elastic deformation in the bulk material beneath the pillar, which results in an erroneously low modulus measurement. The Sneddon Correction for elastic modulus, which was originally developed for nanoindentation, accounts for this [10] and the formula to calculate the corrected modulus (E_S) is given in Equation 6.4.

$$E_s = \frac{h_0}{\left(C_{Tot} - \frac{\sqrt{\pi(1-\nu^2)}}{E\sqrt{A_{base}}} \right) A_{top}} \tag{6.4}$$

where E is the elastic modulus of the bulk polycrystalline mineral (200 GPa after ref. [11]), ν is the Poisson's ratio of olivine (0.25 after ref. [12]), and A_{top} and A_{base} are the area of the top and base of the pillar, respectively. C_{Tot} is the total compliance due to sample displacement as well as

displacement caused by the pillar indenting into the base material ($C_{Tot} = \frac{\partial d_{Tot}}{\partial P}$), where d_{Tot} is the measured displacement and P is the applied load. Because of misalignment between the pillar and the flat punch, the loading portion of the stress-strain curve tended to have a slight nonlinearity. Thus, C_{Tot} was obtained from the unloading portion of the curve when no catastrophic deformation occurred and was simply calculated as the inverse of the slope of the unloading curve at the beginning of unloading.

The modulus must further be corrected for taper, because a larger degree of taper will artificially increase the calculated modulus (i.e. a tapered pillar will be stiffer than an ideal pillar) [13]. Increasing the aspect ratio of the pillar (h_0/r_0) exacerbates this effect. Thus, taking into account the pillar aspect ratio and taper, as well as the apparent modulus from the tapered specimen, a taper-corrected modulus can be calculated as:

$$E = \frac{E_{apparent}}{1 + \frac{h_0}{r_0}\tan\beta} \tag{6.5}$$

Calculating the modulus using both Equations 6.4 and 6.5 produces a result corrected for both base compliance as well as taper.

6.3. Results

The results of a monotonic test to determine a yielding stress are shown in Figure 6.2. The SEM images show that the pillar underwent a complete failure with evidence of longitudinal fractures through the pillar as well as plastic deformation in the remaining fragments. The failure strength from the stress-strain plot in Figure 6.2(c) was approximately 6 GPa, and the measured modulus was 69.4 GPa, which increased to 81.4 GPa after the Sneddon and taper corrections were applied.

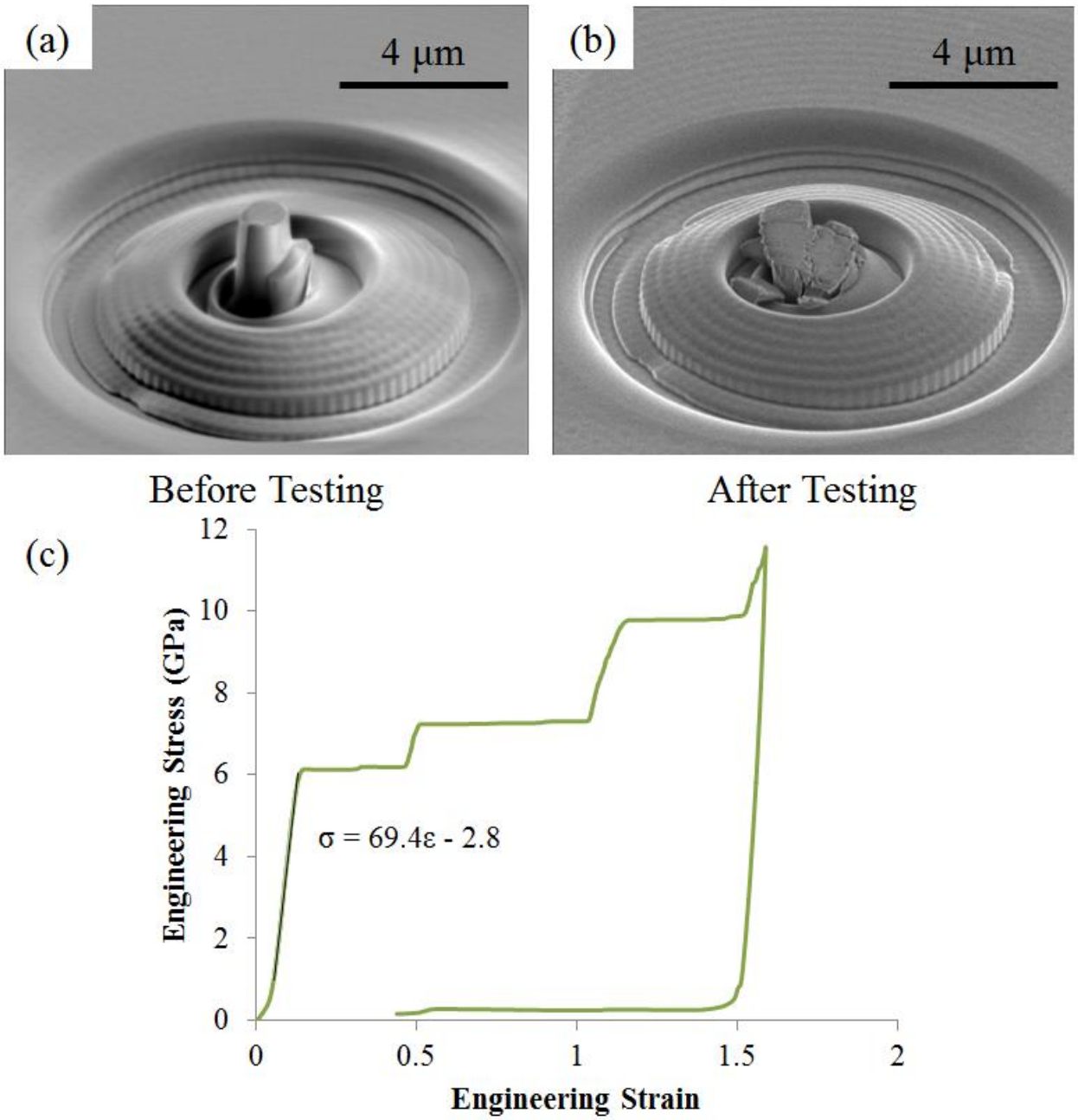

Figure 6.2. SEM images of a pillar tested in monotonic compression **(a)** before testing and **(b)** after testing. **(c)** The resulting stress-strain curve shows that the pillar failed at a uniaxial stress of 6 GPa and had an apparent modulus of 69 GPa, which changed to 87.5 GPa after applying the Sneddon and taper corrections.

The 6 GPa failure stress provided an upper stress limit for creep testing on subsequent pillars. Creep testing commenced on the pillars at a load of 5000 μN, equivalent to a stress of 4.1 GPa for a 1.25μm diameter pillar. Many of the pillars failed during the creep testing, as shown in

Figure 6.3. If the pillar survived the 5000 μN testing with no obvious evidence of damage in subsequent SEM imaging, then the pillars were tested again at 5500 μN, corresponding to a stress of 4.5 GPa for a 1.25μm diameter pillar. The pillars in Figure 6.3 exhibit a variety of deformation behaviors, such as axial splitting (Pillar 1), mushrooming (Pillars 2 and 3), and shearing (Pillars 4 – 6). They also failed at a wide range of times during testing, from as little as 22 seconds after creep was initiated (Pillar 2), to as much as 3567 seconds after being tested for 4 hours at 5000 μN (Pillar 6).

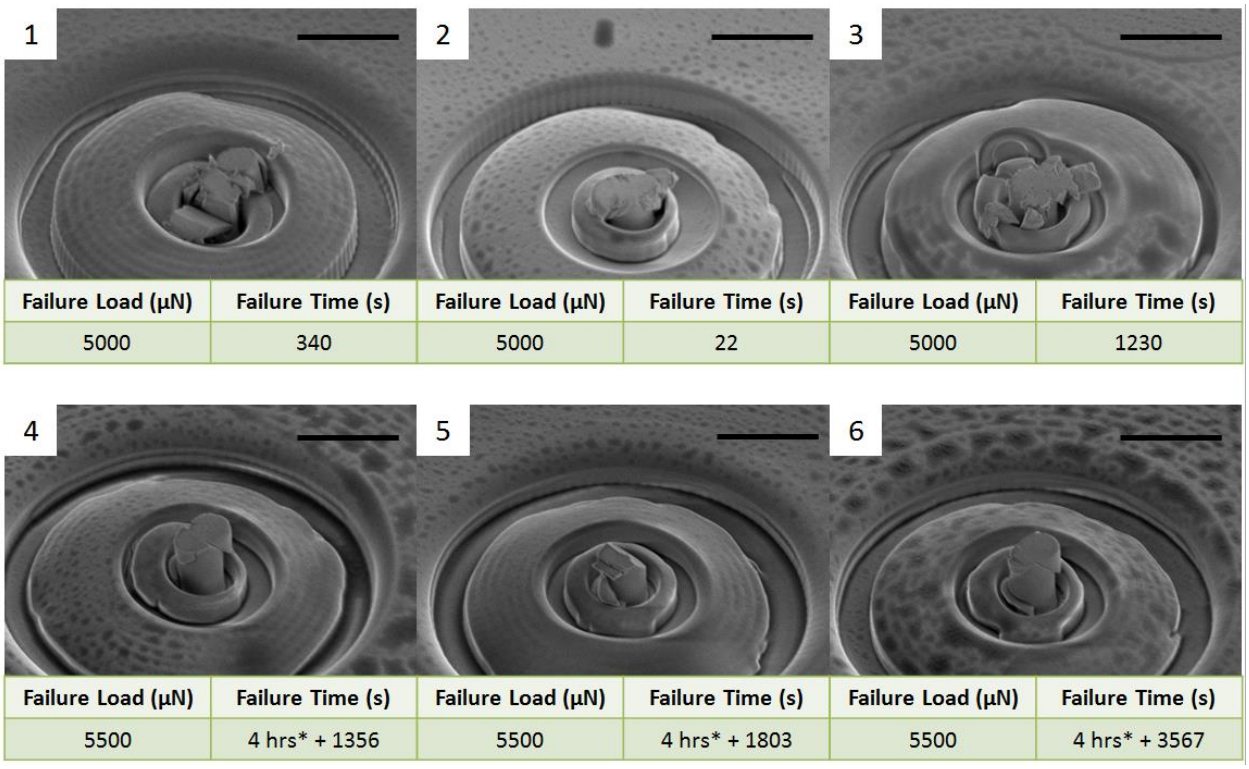

Failure Load (μN)	Failure Time (s)	Failure Load (μN)	Failure Time (s)	Failure Load (μN)	Failure Time (s)
5000	340	5000	22	5000	1230

Failure Load (μN)	Failure Time (s)	Failure Load (μN)	Failure Time (s)	Failure Load (μN)	Failure Time (s)
5500	4 hrs* + 1356	5500	4 hrs* + 1803	5500	4 hrs* + 3567

Figure 6.3. SEM images of pillars that failed catastrophically during creep testing. Below each pillar is the load and the time into the test at which it failed. Pillars 4-6 had already undergone creep testing at 5000 μN for 4 hours and then failed during a second creep test at 5500 μN at the time indicated under each image. Scale bar = 3 μm.

Other pillars, however, exhibited signs of deformation after 4 hours of creep testing, as shown in Figure 6.4. Shear steps were found on the surface of the pillars, indicating dislocation slip had occurred during the creep testing. The properties of these pillars are summarized in Table 6.1.

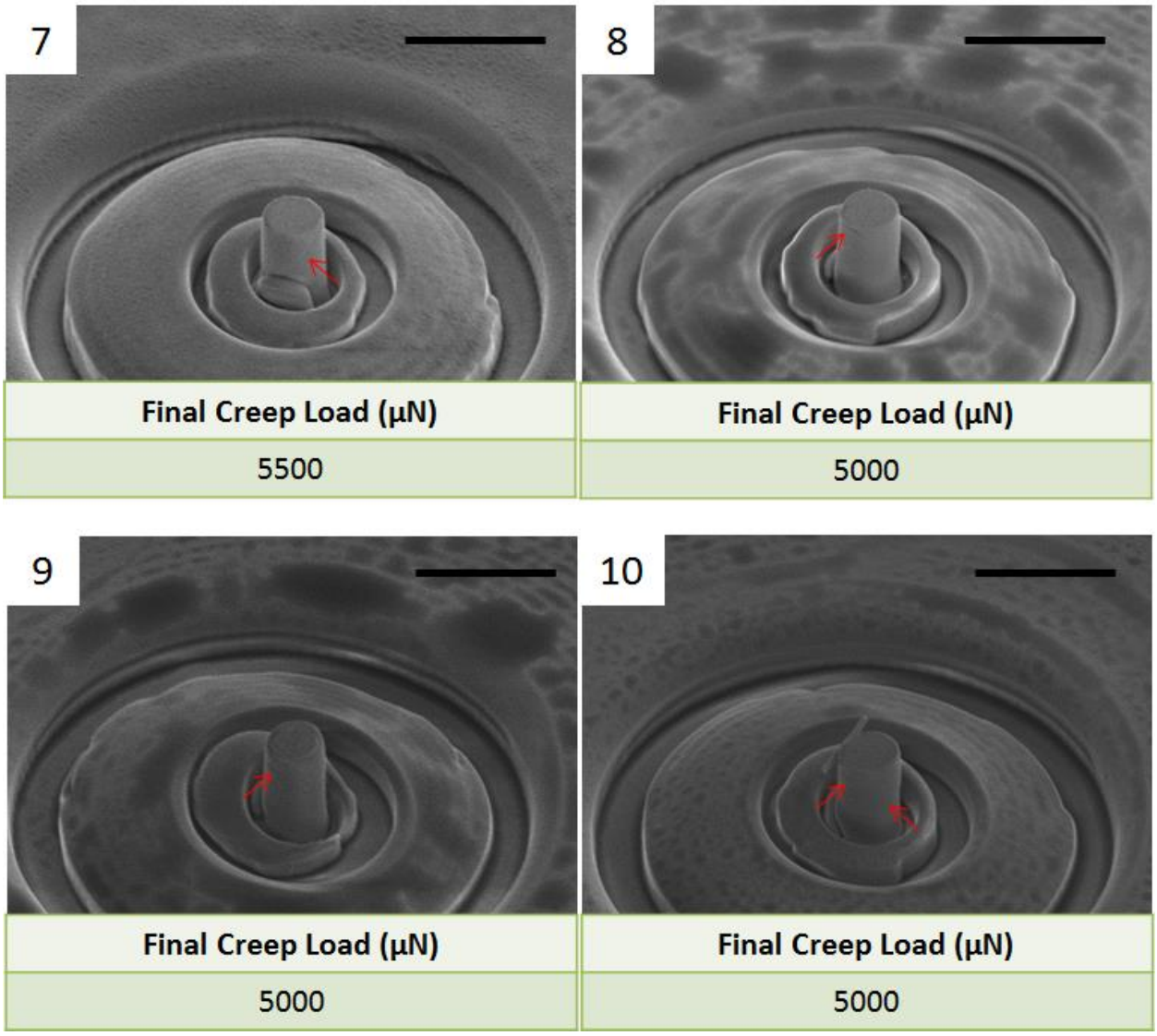

Figure 6.4. SEM images of pillars with evidence of deformation in the form of shear steps, as indicated by the arrows. Pillar 7 was tested at 5000 µN for 4 hours and then tested for 4 hours more at 5500 µN. Pillars 8 – 10 were all tested for 4 hours at 5000 µN. The sliver of material attached to Pillar 10 is dust and not a result of the testing. Scale bar = 3 µm.

Table 6.1. Measured properties of the pillars shown in Figure 6.4, including the stress calculated from the initial pillar diameter, the stress calculated from the final pillar diameter, and the elastic modulus calculated using the base and taper corrections.

Pillar #	σ_i (GPa)	σ_f (GPa)	E_{corr} (GPa)
7	4.1	3.8	179.4
8	4.6	4.1	167.7
9	4.3	3.9	216.0
10	4.1	3.5	185.12

The displacement, and consequently engineering strain, for the pillars in Figure 6.4 was calculated from Equation 6.2c and their plots are shown in Figure 6.5. The plot for Pillar 9 is not included here due to instrument difficulties with the nanoDMA during this test. Pillar 7 exhibited the highest strain rate of $4x10^{-6}$ s^{-1}, and was also the only pillar tested at 5500 μN creep load. Pillars 8 and 10 were tested at 5000 μN and their strain rates were calculated to be $1x10^{-6}$ s^{-1} and $5x10^{-7}$ s^{-1}, respectively.

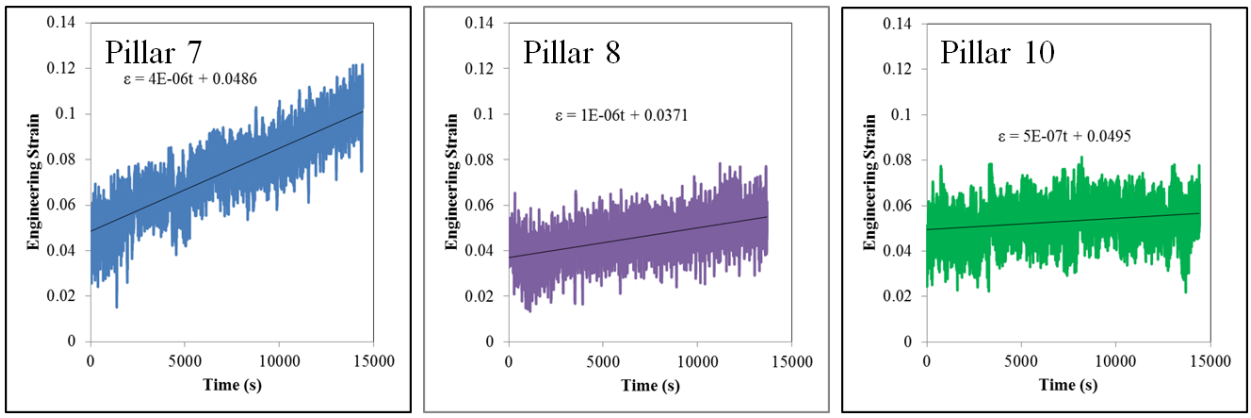

Figure 6.5. Plots of engineering strain over time acquired through using the nanoDMA load oscillations during the creep segment. The pillars exhibited engineering strain rates as high as $4x10^{-6}$ s^{-1} for the pillar tested at 5500 μN to $1x10^{-6}$ s^{-1} and $5x10^{-7}$ s^{-1} for the pillars tested at 5000 μN.

The calculated strain rates and maximum stress from Table 6.1 were then compared to stresses given by the low temperature plasticity flow law described in Chapter 5. The measured strain rate and testing temperature (ambient) were inserted into Equation 5.4, with the same

constants as shown in Figure 5.3 for the five different flow laws obtained through our nanoindentation testing. The difference between the flow laws and the pillar measurements varied from as high as 26% to as low as 0%. The flow law that consistently gave the smallest error was that with $p = 1$ and $q = 1$.

Table 6.2. Properties of the pillars shown in Figure 6.4, including their measured strain rate, maximum engineering stress from Table 6.1, and then the stress given by five different low temperature plasticity flow laws at that strain rate for comparison. The difference between the maximum engineering stress and the stress from the flow law are also provided.

			p =1/2 q = 1	p =3/4 q = 4/3	p = 1 q =2	p =2/3 q = 2	p =1 q = 1
Pillar #	**Measured Strain Rate (s^{-1})**	**Maximum Engineering Stress (GPa)**	**Stress (GPa)**	**Stress (GPa)**	**Stress (GPa)**	**Stress (GPa)**	**Stress (GPa)**
7	4.00E-06	4.1	3.91	3.93	3.9	3.53	4.19
		Percent Difference:	4.63%	4.15%	4.88%	13.90%	2.20%
8	1.00E-06	4.6	3.82	3.85	3.82	3.41	4.14
		Percent Difference:	16.96%	16.30%	16.96%	25.87%	10.00%
10	5.00E-07	4.1	3.76	3.81	3.78	3.76	4.10
		Percent Difference:	8.29%	7.07%	7.80%	8.29%	0.00%

In order to determine if dislocations were being formed upon loading or during the creep segment of the test, cyclic testing was performed on a pillar. The pillar was loaded to 5000 μN and unloaded to 100 μN for 10 cycles at a rate of 1000 μN/s. The load-displacement curves are shown in Figure 6.6. Extensive hysteresis was observed in the first cycle, indicating that plastic deformation occurred during loading. This hysteresis is essentially gone by the second cycle, meaning that deformation was elastic for the remainder of the cycles. The corrected modulus measurements from the unloading curve are consistent for all ten cycles. However, when the modulus is calculated from the loading portion of the first cycle, the value is 163.7 GPa, a 26% decrease from what is calculated from the unloading cycle.

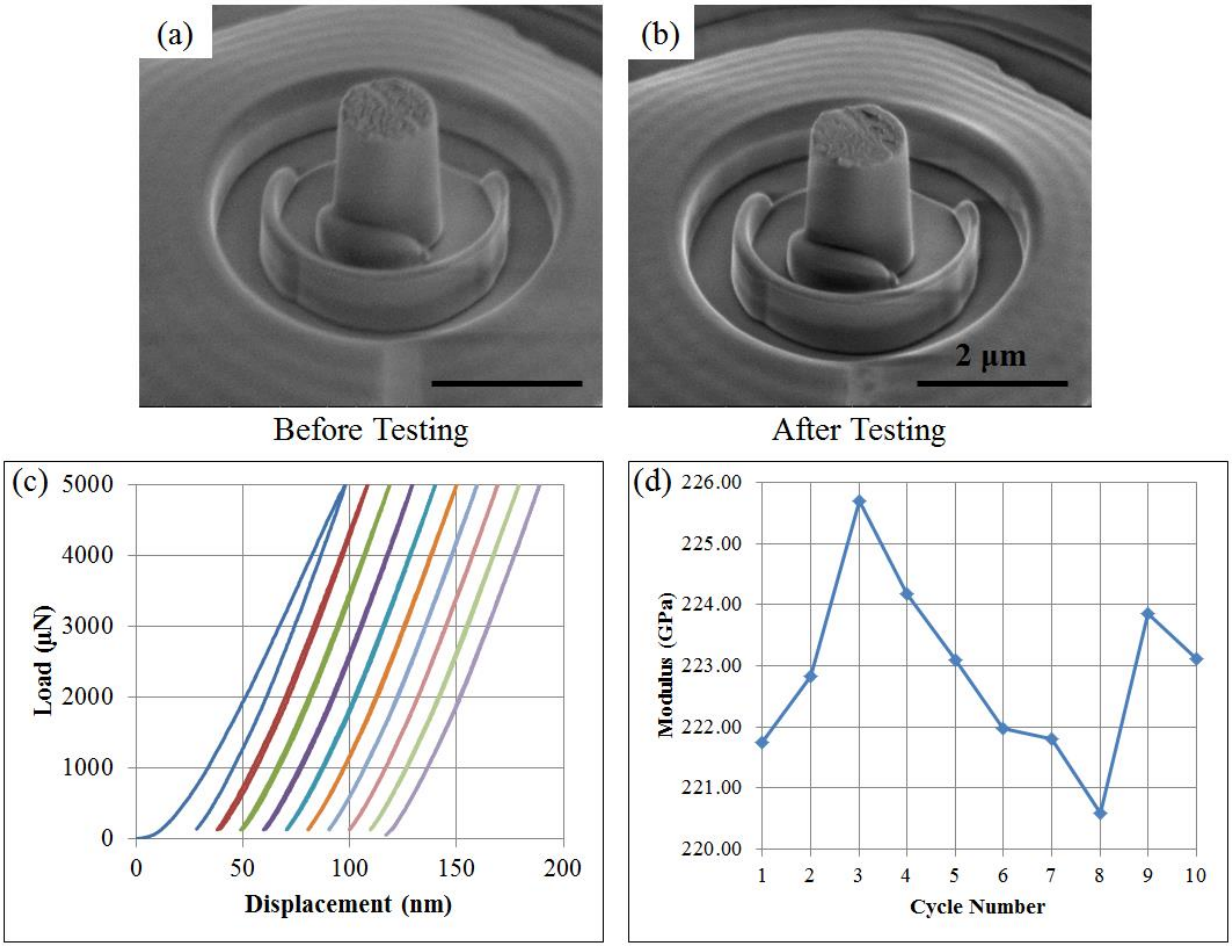

Figure 6.6. SEM images of the pillar **(a)** before and **(b)** after cyclic testing. **(c)** The load-displacement curves are separated along the x-axis for visual clarity. The load-displacement curve corresponding to the first cycle exhibits noticeable hysteresis, which is essentially gone by the second cycle. **(d)** The modulus calculated from the unloading curve are consistent among all ten cycles.

Finally, TEM foils were collected from the deformed pillars to analyze the dislocation activity creating the shear steps that were visible in the SEM. Figure 6.7 shows the SEM image of Pillar 7 along with a bright field TEM image and diffraction pattern clearly showing slip of (100) planes. TEM analysis of Pillar 10 in Figure 6.8 showed slip on both (100) and (010) planes. The TEM foils were cut at different angles, which is why the images in Figure 6.7 and Figure 6.8 are in opposite directions. The primary difference in testing between the two pillars is

that Pillar 7 was tested at 5000 μN for 4 hours and then again at 5500 μN for 4 hours, while Pillar 10 was only tested at 5000 μN for 4 hours.

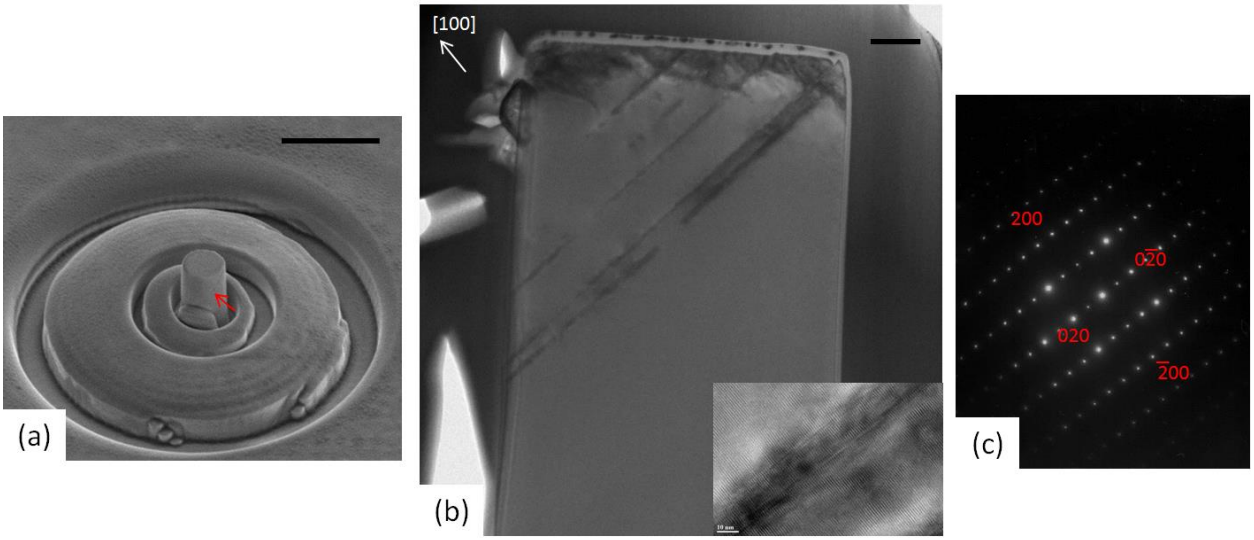

Figure 6.7. (a) SEM image of Pillar 7, scale bar = 3 μm. **(b)** Bright field TEM image of the pillar showing clear slip along the (100) planes. Scale bar = 200 nm. The inset is a high resolution image of the slip planes. **(c)** The corresponding [001] diffraction pattern of the TEM image.

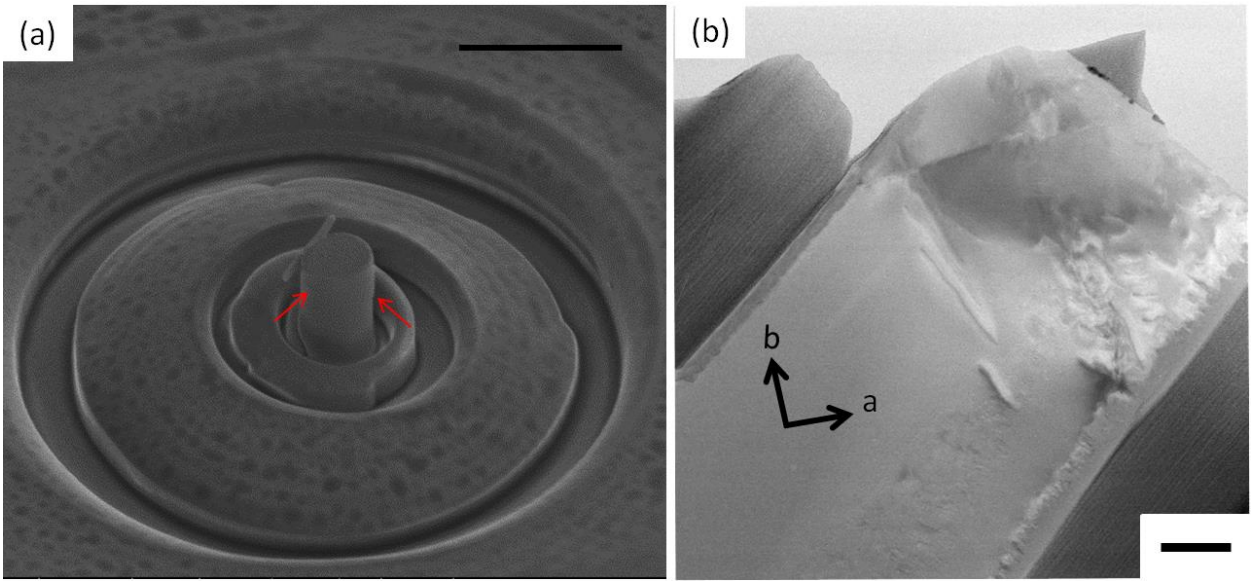

Figure 6.8. (a) SEM image of Pillar 10, scale bar = 3 μm. **(b)** Bright field TEM image of the pillar showing slip along two separate slip planes. Scale bar = 200 nm.

6.4. Discussion

At ambient conditions and laboratory time scales, olivine will fail via brittle fracture, inhibiting the study of low temperature plasticity in this material [4]. The goal of this work was to induce plastic deformation in olivine at room temperature without fracture of the material. As demonstrated from the relevant microscopy, some of the olivine micropillar compression creep tests resulted in dislocation slip along distinct crystallographic planes in the pillars without failure. When testing micropillars, there is a size below which cracking is suppressed. This size-dependent change in deformation behavior has been observed in a variety of materials, including silicon [14], $MgAl_2O_4$ spinel [15], and metallic glass [16,17]. The exact mechanism behind this phenomenon is still unclear, however several explanations have been proposed, including fewer flaws in smaller samples [18], increase in fracture energy [19], or decrease in crack driving force [20]. The fact that room temperature plasticity was observed at all in olivine is in itself remarkable, as this has notoriously been difficult using traditional testing methods at bulk scale.

The moduli measured here ranged from as low as 81.4 GPa to as high as 216 GPa. However, it was shown from the cyclic loading experiment that the elastic modulus calculated from loading is on the order of 25% less than that of unloading, most likely due to misalignment effects [21]. When only the moduli from unloading are considered, they range from 167.7 to 225.7 GPa, near the given aggregate Young's modulus of 200 GPa [11].

For the tests where the pillar did not fail, slip was observed through TEM analysis on (100) and (010) planes, which are the primary slip planes in olivine in the [110] orientation [22]. Furthermore, an engineering stress and strain rate were calculated for the surviving pillars. The strain rates measured indirectly through force oscillation during creep testing were on the order of 10^{-6} - 10^{-7} s^{-1}. It was not possible to verify the displacement changes associated with those

strain rates and predicted from Equation 6.2c, because those displacement changes were on the order of the error of the height measurements obtained through the SEM image analysis. The engineering stresses were measured to be 3.5 – 4.6 GPa for the creep tests, or as high as 6 GPa for the monotonic tests. These measurements produced striking agreement with the low temperature plasticity flow law fits determined from the earlier nanoindentation study. It is important to note here that size can affect the compressive yield strength of crystalline materials, with nanoscale specimens exhibiting yield strengths over an order of magnitude greater than their bulk counterparts [23]. This behavior is attributed to fewer dislocation sources [24] and 'dislocation starvation', where dislocations are annihilated at the sample surfaces instead of interacting within the sample volume [23]. However, this yield strength effect is much more pronounced in metallic materials than in ceramics, where the yield strength is closer to the theoretical strength and the dislocation activation volume is smaller [14,25]. This size effect on strength is most likely not a concern here, due to the fact that the material is a ceramic and that there is good agreement between the predicted flow law and the measured values. Overall the fact that there is agreement from the data obtained using two different methods, micropillar compression and nanoindentation, is encouraging.

In other pillars, complete shearing along the crystallographic planes resulted after a dwell time during the creep testing. The hysteresis observed in the first cycle of the cyclic testing clearly shows that plastic deformation in the pillar is initiated upon loading. However, the distribution of dwell times observed before catastrophic failure also indicate that dislocation activity continues throughout the creep test until a criticality is reached that causes complete or nearly complete shear along a primary slip plane. This behavior is reminiscent of creep fracture in ceramics, caused by the nucleation, growth, and coalescence of cavities that form a

microcrack and leads to subsequent failure [26]. It is conceivable in this case that dislocation slip occurs along a favorable crystallographic plane, but is then obstructed by an obstacle with a large energy barrier, causing a buildup of other dislocations in the wake of the slip and increasing the stress, resulting in cleavage failure along the slip plane [27].

6.5. Conclusions

The goal of this work, achieving plastic deformation in olivine at room temperature was indeed achieved. Here we provided experimental conditions, including uniaxial stresses and strain rates, that result in dislocation slip without failure in olivine at room temperature. Furthermore, the results obtained from the micropillar compression support the findings from the nanoindentation study, providing increased confidence in our fitting parameters to the established low temperature plasticity flow law. This increased understanding of low temperature plasticity is essential to predicting olivine rheology at conditions relevant to the shallow lithosphere. Micropillar compression, as well as nanoindentation, are reliable methods of studying low temperature plasticity of geologic materials and can further increase our understanding of the Earth's upper mantle dynamics.

6.6. References

[1] D.L. Kohlstedt, B. Evans, S.J. Mackwell, Strength of the Lithosphere: Constraints Imposed by Laboratory Experiments, J. Geophys. Res. 100 (1995) 17587–17602. doi:10.1016/S0016-0032(16)90156-X.

[2] M.E. Broz, R.F. Cook, D.L. Whitney, Microhardness, toughness, and modulus of Mohs scale minerals, Am. Mineral. 91 (2006) 135–142. doi:10.2138/am.2006.1844.

[3] J. Rabier, P.O. Renault, D. Eyidi, J.L. Demenet, J. Chen, H. Couvy, L. Wang, Plastic deformation of silicon between 20 °C and 425 °C, Phys. Status Solidi. 4 (2007) 3110–3114. doi:10.1002/pssc.200675480.

[4] S. Mei, A.M. Suzuki, D.L. Kohlstedt, N.A. Dixon, W.B. Durham, Experimental Constraints on the Strength of the Lithospheric Mantle, J. Geophys. Res. 115 (2010).

doi:10.1029/2009JB006873.

[5] Y.B. Wang, W.B. Durham, I.C. Getting, D.J. Weidner, The deformation-DIA: A new apparatus for high temperature triaxial deformation to pressures up to 15 GPa, Rev. Sci. Instrum. 74 (2003) 3002–3011. doi:10.1063/1.1570948.

[6] A.C. Fischer-Cripps, Nanoindentation, Third Ed, Springer Science+Business Media, LLC, New York, 2011.

[7] C.L. Wang, Y.H. Lai, J.C. Huang, T.G. Nieh, Creep of nanocrystalline nickel: A direct comparison between uniaxial and nanoindentation creep, Scr. Mater. 62 (2010) 175–178. doi:10.1016/j.scriptamat.2009.10.021.

[8] W.H. Poisl, W.C. Oliver, B.D. Fabes, The relationship between indentation and uniaxial creep in amorphous selenium, J. Mater. Res. 10 (1995) 2024–2032. doi:10.1557/JMR.1995.2024.

[9] J. Hütsch, E.T. Lilleodden, The influence of focused-ion beam preparation technique on microcompression investigations: Lathe vs. annular milling, Scr. Mater. 77 (2014) 49–51. doi:10.1016/j.scriptamat.2014.01.016.

[10] I. Sneddon, The relation between load and penetration in the axisymmetric Boussinesq problem for a punch of arbitrary profile, Int. J. Eng. Sci. 3 (1965) 47–57. http://www.sciencedirect.com/science/article/pii/0020722565900194 (accessed May 8, 2012).

[11] B. Evans, C. Goetze, The temperature variation of hardness of olivine and its implication for polycrystalline yield stress, J. Geophys. Res. 84 (1979) 5505–5524. doi:10.1029/JB084iB10p05505.

[12] N.I. Christensen, Poisson's Ratio and Crustal Seismology, J. Geophys. Res. 101 (1996) 3139–3156. doi:10.1029/95JB03446.

[13] A. Bharathula, S.W. Lee, W.J. Wright, K.M. Flores, Compression testing of metallic glass at small length scales: Effects on deformation mode and stability, Acta Mater. 58 (2010) 5789–5796. doi:10.1016/j.actamat.2010.06.054.

[14] S. Korte, J.S. Barnard, R.J. Stearn, W.J. Clegg, Deformation of Silicon - Insights from Microcompression Testing at 25-500 C, Int. J. Plast. 27 (2011) 1853–1866. doi:10.1016/j.ijplas.2011.05.009.

[15] S. Korte, W.J. Clegg, Micropillar compression of ceramics at elevated temperatures, Scr. Mater. 60 (2009) 807–810. doi:10.1016/j.scriptamat.2009.01.029.

[16] D. Jang, J.R. Greer, Transition from a strong-yet-brittle to a stronger-and-ductile state by size reduction of metallic glasses, Nat. Mater. 9 (2010) 215–219. doi:10.1038/nmat2622.

[17] C.A. Volkert, A. Donohue, F. Spaepen, Effect of sample size on deformation in amorphous metals, J. Appl. Phys. 103 (2008) 83539. doi:10.1063/1.2884584.

[18] H. Gao, B. Ji, I.L. Jager, E. Arzt, P. Fratzl, Materials become insensitive to flaws at nanoscale: lessons from nature, Proc. Natl. Acad. Sci. 100 (2003) 5597–5600. doi:10.1073/pnas.0631609100.

[19] F. Östlund, K. Rzepiejewska-Malyska, K. Leifer, L.M. Hale, Y. Tang, R. Ballarini, W.W. Gerberich, J. Michler, Brittle-to-ductile transition in uniaxial compression of silicon pillars at room temperature, Adv. Funct. Mater. 19 (2009) 2439–2444. doi:10.1002/adfm.200900418.

[20] F. Östlund, P.R. Howie, R. Ghisleni, S. Korte, K. Leifer, W.J. Clegg, J. Michler, Ductile–brittle transition in micropillar compression of GaAs at room temperature, Philos. Mag. 91 (2011) 1190–1199. doi:10.1080/14786435.2010.509286.

[21] A.A. Konstantinidis, K. Michos, E.C. Aifantis, On the correct interpretation of compression experiments of micropillars produced by a focused ion beam, J. Mech. Behav. Mater. 25 (2016) 83–87. doi:10.1515/jmbm-2016-0009.

[22] W.B. Durham, C. Goetze, Plastic Flow of Oriented Single Crystals of Olivine, J. Geophys. Res. 82 (1977) 5737–5753.

[23] J.R. Greer, W.D. Nix, Nanoscale Gold Pillars Strengthened through Dislocation Starvation, Phys. Rev. B - Condens. Matter Mater. Phys. 73 (2006) 1–6. doi:10.1103/PhysRevB.73.245410.

[24] S.H. Oh, M. Legros, D. Kiener, G. Dehm, In situ observation of dislocation nucleation and escape in a submicrometre aluminium single crystal, Nat. Mater. 8 (2009) 95–100. doi:10.1038/nmat2370.

[25] S. Korte, W.J. Clegg, Discussion of the dependence of the effect of size on the yield stress in hard materials studied by microcompression of MgO, Philos. Mag. 91 (2011) 1150–1162. doi:10.1080/14786435.2010.505179.

[26] C.H. Hsueh, A.G. Evans, Creep fracture in ceramic polycrystals-II. effects of inhomogeneity on creep rupture, Acta Metall. 29 (1981) 1907–1917. doi:10.1016/0001-6160(81)90028-6.

[27] M.F. Ashby, R.A. Verrall, Micromechanisms of flow and fracture, and their relevance to the rheology of the upper mantle, Philos. Trans. R. Soc. London A. 288 (1977) 59–95.

Chapter 7: Conclusions

This dissertation explored fundamental questions about the structure, properties, and behavior of two material systems. Significant insight into the structure and properties of metallic glasses and their composites as well as into the properties and mechanical behavior of olivine were achieved through the use of micromechanical testing techniques. The work here provides a unique perspective into better understanding these two materials, providing valuable information fitting into the framework of their respective bodies of knowledge.

The first material that was explored was monolithic metallic glass. Here, mechanical heterogeneity was quantified using both nanoindentation and dynamic modulus mapping and was discovered over two length scales. The nanoindentation testing showed spatially random heterogeneity at the micron-scale. The linear relationship between hardness and modulus was indicative of compositional fluctuations in the material causing the mechanical variations. Dynamic modulus mapping showed the presence of sub-micron heterogeneities forming an elastic microstructure featuring an interconnected network of stiff regions encompassing softer areas. Because these sub-micron heterogeneities were superimposed on the micron-scale heterogeneities found through the nanoindentation, this led to the concept of a hierarchy of heterogeneity being present in metallic glasses. Different domains of features with common aspect ratio and orientation were also observed in the maps, reminiscent of the impingement of microstructural colonies. Dynamic modulus mapping was also employed in the vicinity of a shear band, and general alignment of regions of higher aspect ratio and orientation were observed biased in the direction of the shear band. This work demonstrated the existence of heterogeneities in a Zr-based metallic glass at multiple length scales, including the presence of an elastic microstructure, and provides a new experimental approach for studying the microstructure of

BMGs with a view towards improving the ductility and structural reliability of these materials. Future work in this area should focus on further quantification of these microstructural features. Furthermore, since the only glass investigated here was Zr-based, potential variations in the heterogeneities in a different metallic glass system with differing mechanical behavior (e.g. Fe-based glasses) should also be explored.

Complementary to the study on monolithic metallic glass, the same techniques were also used to investigate properties of a series of Ti-based bulk metallic glass composites. This composite series exhibited a wide array of macro-scale tensile behavior, resulting from very slight compositional changes in the β-stabilizing element, vanadium. The modulus and hardness of the glass and crystalline phases for each of the composites was determined via nanoindentation. This showed that some aspects of the tensile behavior, such as the brittle failure of the composite without any vanadium, could be attributed to differences in the modulus between the two phases, although it could not completely describe the tensile behavior of the entire series. Modulus mapping on three of the composites showed the largest distribution of heterogeneities in the glass phase of the composite with the greatest strength, ductility, and strain hardening of the three composites. This indicates that heterogeneities within the glass phase of the composite play an important role in the deformation of the composite. Future design of BMGCs should seek to optimize both the interphase heterogeneity between the glass and the crystal as well as the intraphase heterogeneity within the glass. As with the monolithic glass, future work in this area should focus more on quantification of the elastic microstructure and comparing elastic microstructures between different composite systems.

The second material to be explored was the mineral olivine. The rheology of olivine plays an important role in the dynamics of Earth's upper mantle. At conditions of low temperature and high stress, such as in semi-brittle regions of the lithosphere, the deformation

mechanism transitions into low temperature plasticity. Low temperature plasticity is difficult to study in typical laboratory conditions, requiring high confining pressures to suppress cracking in favor of dislocation glide. Two micromechanical testing techniques, nanoindentation and micropillar compression, were used to provide insight into this mode of deformation.

Nanoindentation of olivine at temperatures ranging from 0°C – 175°C resulted in indents exhibiting plastic flow, with no evidence of cracking. The indentation properties were measured for the temperature range and translated into uniaxial stresses and strain rates using available models. An established low temperature plasticity flow law could then be determined. Peierls stresses of olivine determined through the flow law ranged from 5.32 – 6.45 GPa. This work showed the utility and potential of using nanoindentation to complement traditional high temperature, high pressure rock mechanics experiments and better understand geologic materials at low temperature conditions. Future work here should focus on expanding the technique to characterize other minerals with significance for mantle rheology and refining the models for converting indentation properties into uniaxial properties, making them more applicable to geologic materials.

Complementary to the nanoindentation study, micropillar compression tests were also performed on olivine. This type of testing results in uniaxial properties, which are much easier to analyze than nanoindentation. It has been found in other materials that a brittle to ductile transition can occur with decreasing specimen size. That characteristic was exploited here, and indeed dislocation slip was induced in olivine without brittle failure. Slip occurred along primary slip planes and for some of the pillars, catastrophic shearing occurred along these planes as well after a dwell time during creep testing. When compared to the flow laws generated from the nanoindentation study, good agreement was found between results from the two independent

testing techniques, lending confidence to the viability of the determined flow law. This increased understanding of low temperature plasticity is essential to predicting olivine rheology at conditions relevant to the shallow lithosphere. Micropillar compression, as well as nanoindentation, were shown to be reliable methods of studying low temperature plasticity of geologic materials and can further increase our understanding of the Earth's upper mantle dynamics. Further work in this area should also expand the technique to different minerals. Moreover, more investigation into the dwell time before catastrophic shearing should be performed to more precisely determine its origin.